DETECTION AND CHARACTERISATION OF NANOPARTICLES USING INDUCTIVELY COUPLED PLASMA MASS SPECTROMETRY

Dissertation

zur Erlangung des akademischen Grades

Doctor rerum naturalium

(Dr. rer. nat.)

im Fach Chemie

Spezialisierung: Angewandte Analytik und Umweltchemie

eingereicht an der

Mathematisch-Naturwissenschaftlichen Fakultät

der Humboldt-Universität zu Berlin

von

M.Sc. Benita Schmidt (geb. Ramkorun)

Präsidentin der Humboldt-Universität zu Berlin

Prof. Dr.-Ing. Sabine Kunst

Dekan der Mathematisch-Naturwissenschaftlichen Fakultät

Prof. Dr. Elmar Kulke

Gutachter/-innen: Prof. Dr Detlef Günther

Prof. Dr Janina Kneipp

Prof. Dr Ulrich Panne

Tag der mündlichen Prüfung: 26.04.2019

Acknowledgements

The journey towards my thesis has been very exciting. I had the great opportunity to work alongside bright people and felt fortunate to come across the different people who helped me reach my goal of finishing a PhD. I found out that doing a PhD is harder than becoming a parent. Some of whom came into my life to guide me, to share their knowledge or to be great support in a foreign environment.

I am extremely grateful to Dr. Norbert Jakubowski and Prof. Detlef Günther; you have been the best supervisors I could ever ask for. In your own different ways, you have always encouraged, inspired and supported me. Thank you for giving me the opportunity to learn from you and to work in your groups. On a different note; Norbert, you made life in BAM and Berlin much easier! Detlef, thank you for giving me the chance to be part of ETH even if only for a few months.

I would not have been doing a PhD at the HU Berlin without you SALSA! Thank you Prof. Ulrich Panne, Prof. Janina Kneipp and Katharina Schultens for the first interview and your support throughout my time as a SALSA student! I am thankful to the SALSA administration for the taking care of my paper works and organising enjoyable lectures and summer schools.

I am extremely thankful to Spiros Pergantis who patiently introduced me to all the essentials I needed to work on this project and for learning about life in Germany/Berlin together! Thank you Diego Esteban-Fernández for teaching me about the instruments and software, for all the work and food discussions we had!

I would like to thank my group members from FB 1.1 at BAM. Thank you Petra Schubert for organising and for the pleasant German chats! Thank you Heike, Silke, Larissa, Herr Vogel, Antja, Carina and Andreas for all the tips and scientific discussions. I am grateful to Frank and Fabian for the intellectual and Berlin-style discussions and good friendships! Matthias,

Jana, Uwe, Ana, Janine, Pranee, Konrad and Antje; thank for your support and good company in the lab.

I had the great opportunity to work along some wonderful people at the ETH Zürich. Alex, you are an inspiration! Thank you for your support, positivity, encouragement and making labwork a lot of fun! Thank you Bodo and Joachim for all the technical discussions and encouraging critical thinking. Thank you Sabrina for being my MDG support via long distance. Thank you Nicole for all the organisation. Thank you Lyndsey for working together and the scientific discussions. Thank you to the rest of the team; Beni, Thomas, Marcel, Ceren, Deborah, Kevin, Lorenzo, Kathrin, Natalia for your support, and (work hard, play hard motto!) help and making my time in Zürich a pleasant one despite all the stress in trying to finish my lab work on time.

To my dream team; my office mates and friends : Nahla, Cinthya, Dorota and Sabine thank you so much for being there through thick and thin. For sharing the stress and multiplying the fun!

To Traudel and Heinrich; thank you for leaving behind your home so readily to come help me whenever I needed extra support. Thank you Heinrich for your support in the final stages. Thank you Johannes for spending half of our life together reading about ICP-MS and listening to my multiple practice presentations without you having a clue about chemistry. Thank you Karan for your support, thank you Vijeta for your words of encouragement.

Finally but definitely not the least, I am extremely thankful to my parents who have always supported me in my crazy journey of getting an education all over the world. They have never said no to my requests of going far away and made sure I had everything I needed to achieve this milestone today. I hope I can be at least half as patient and supportive as you as a parent.

Abstract

In this doctoral thesis an analytical method for characterising metal nanoparticles (NPs) was developed and its application for investigating natural samples verified. An analytical system consisting of a microdroplet generator (MDG) used in combination with a pneumatic nebuliser (PN) and an inductively coupled plasma mass spectrometer (ICP-MS) proved capable of quantitatively and qualitatively identifying NPs.

The MDG was used to establish the calibration function for mass quantification of the metal present in the sample NPs introduced via the PN. The major advantage of this configuration is that the MDG generated droplets of tailored size for any given metal while offering a 100 % transport efficiency. The introduced mass correlated with signal intensities of NPs and thus the microdroplet generated droplets could be used for calibration purposes without the need for any reference material. Thus, the tedious and error-prone nebuliser efficiency determination step that is required when determining the NP metal content using the single particle mode ICP-MS (spICP-MS) approach, could be avoided.

With this dual sample introduction method, the sizes and concentrations of a range of standard silver (Ag) NPs and gold (Au) reference NPs were determined with high accuracy. This new technique was successfully used to characterise metal oxides NPs such as aluminium oxide (Al_2O_3) NPs with some washing steps involved before analysis.

Additionally, together with a new commercially available ICP-time of flight-MS (ICP-TOF-MS) the characterisation of Ag- and Au-NPs was carried out in various matrices: In hydrochloric (HCl) and nitric acid (HNO_3) at a range of concentration and in different elemental environments. In the presence of matrices, it was found that the size characterisation of the NPs is correct within the standard deviation.

Finally, taking advantage of a simultaneous mass analysis, the application of this system was demonstrated in the analysis of macroparticles and NPs in environmental samples. The ICP-TOF-MS was used at a high time resolution where it was possible to distinguish between NPs, macroparticles, and a wide variety of particles consisting of different metals and compositions.

The new configuration not only made it possible to characterise a range of particles in natural samples simultaneously, but it was also able to distinguish between naturally occurring and engineered particles and gave an insight to trace back the source of an unknown sample of water depending on its particle content.

Zusammenfassung

In dieser Doktorarbeit wurde eine analytische Methode zur Charakterisierung metallischer Nanopartikel (NPs) entwickelt und die Methode bei der Untersuchung natürlicher Proben angewendet. Mit einem analytisches System bestehend aus einem Mikrotropfengenerator (microdroplet generator, MDG) zusammen mit einem pneumatischen Zerstäuber und einem induktiv gekoppeltem Plasma-Massenspektrometer (ICP-MS) konnte eine quantitative und qualitative Charakterisierung von NPs durchgeführt werden.

Der MDG wurde verwendet um die Kalibrierungsfunktion für die massenspektrometrische Quantifizierung der Metalle in den Nanopartikelproben, die über den pneumatischen Zerstäuber eingeführt wurden, einzurichten. Der Hauptvorteil dieser Anordnung besteht darin, dass mit dem MDG für jedes Metall Tropfen einer gewünschten Größe hergestellt werden können und eine 100 %-ige Transporteffizienz gegeben ist. Die eingeführte Masse korrelierte mit der Signalintensität von Nanopartikeln, so dass die mit dem MDG generierten Tropfen für die Kalibrierung verwendet werden konnten ohne dass Referenzmaterial erforderlich war. Die aufwändige und fehleranfällige Bestimmung der Effizienz eines Zerstäubers, die für die Bestimmung des Metallgehaltes von NPs mittels eines Einzelpartikel-ICP-MS (spICP-MS) erforderlich ist, konnte dadurch vermieden werden.

Unter Anwendung dieser dualen Einführungsmethode wurden Größen und Konzentrationen einer Reihe von Standard Silber (Ag) NPs und Referenz Gold (Au) NPs mit hoher Genauigkeit bestimmt. Nach der Durchführung von Reinigungsschritten vor der Analyse konnten auch Metalloxid NPs wie Aluminiumoxid (Al_20_3) NPs charakterisiert werden.

Zusätzlich wurde mit einem neuen kommerziell verfügbaren ICP-Flugzeitmassenspektrometer (ICP-TOF-MS) Ag und Au NPs in unterschiedlichen Matrices

charakterisiert: in verschiedenen Salzsäure (HCl)- und Salpetersäure (HNO_3)-Konzentrationen und in Gegenwart verschiedener Elemente. Bei den unterschiedlichen Matrices war die Größenbestimmung innerhalb der gegebenen Standardabweichungen korrekt.

Abschließend wurde unter Realisierung des Vorteils der gemeinsamen Analyse die Anwendbarkeit dieses Systems bei der Untersuchung von Makropartikeln und Nanopartikeln in Umweltproben gezeigt. Bei hoher Zeit-Auflösung des ICP-TOF-MS war es möglich, Nanopartikel, Makropartikel und sehr verschiedenartige Partikel aus unterschiedlichen Metallen und mit unterschiedlicher Zusammensetzung zu unterscheiden.

Diese neue Anordnung ermöglicht nicht nur eine gemeinsame Bestimmung einer Reihe von in natürlichen Proben vorkommenden Partikeln, sondern ermöglicht auch zwischen natürlich vorkommenden und künstlich hergestellten Partikeln zu unterschreiben. Zudem kann sie aufgrund des Partikelgehaltes Hinweise auf die Herkunft einer unbekannten Wasserprobe geben.

Table of Contents

Abstract II

Zusammenfassung IV

Table of Contents VI

1 Introduction 1

1.1 Nanoparticles 1

1.2 Inductively coupled plasma mass spectrometry 6

1.3 Mass analysers 8

1.3.1 Quadrupole mass analyser 9

1.3.2 Sector field mass analyser 10

1.3.3 Time of flight mass analyser 11

1.4 Sample introduction technique 14

1.4.1 Liquid introduction 14

1.4.2 Nebulisers 15

1.4.3 Spray chambers 16

1.4.4 Matrix effects 17

1.4.4.1 Acidic matrix effects 17

1.4.4.2 Elemental matrix effect 18

1.5 Single particle inductively coupled plasma mass spectrometry 20

1.5.1 Background 20

1.5.2 Particle characterisation 21

1.5.3 Transport efficiency 23

1.5.4 Nanoparticle data collection 25

1.5.5 Nanoparticle measurement by single particle inductively coupled plasma mass spectrometry 26

1.5.6 Limitations of single particle inductively coupled plasma mass spectrometry 28

1.6 Monodispersed droplet introduction 29

1.6.1 Background 29

1.6.2 Microdroplet generator 31

1.6.3 Microdroplet generator inductively coupled plasma optical emission spectrometry 32

1.6.4 Microdroplet inductively coupled plasma mass spectrometry 34

2 Aim and objectives 37

3 Experimental 40

3.1 Chemicals 40

3.1.1 Experiments on spICP-MS and dual sample introduction system nebuliser 40

3.1.2 Analysis of metal oxides nanoparticles 41

3.1.3 Matrix effect studies 41

3.1.3.1 Acid effects 41

3.1.3.2 Elemental matrix effect studies 42

3.1.4 Experiments on application of microdroplet generator pneumatic nebuliser inductively coupled time of flight mass spectrometry in environmental water samples 42

3.2 Microdroplet generator 43

3.3 Inductively coupled plasma mass spectrometry 44

3.3.1 Inductively coupled plasma quadrupole mass spectrometry 44

3.3.2 Sector field inductively coupled plasma mass spectrometry 45

3.3.3 Inductively coupled plasma time of flight mass spectrometry 47

3.4 Transmission electron microscopy 50

3.5 Data evaluation 50

4 Results and Discussion 51

4.1 Single particle mode inductively coupled plasma mass spectrometer on gold nanoparticles 51

4.2 Coupling of microdroplet generator to an inductively coupled mass spectrometer 55

4.3 Investigation of a combined microdroplet generator and pneumatic nebulisation system for rapid quantitative determination of metal-containing nanoparticles using inductively coupled plasma mass spectrometry[134] 60

4.3.1 Investigation of possible interference of the two sample introduction systems 60

4.3.2 Optimisation of inductively coupled plasma mass spectrometry parameters for the dual microdroplet pneumatic nebuliser inlet system 61

4.3.3 Dual inlet signal calibration 65

4.3.4 Particle size determination 67

4.3.5 Transport efficiency determination 70

4.3.6 Validation of the new approach 72

4.4 Metal oxides nanoparticle studies using dual configuration 76

4.4.1 Analysis of ZnO nanoparticles 76

4.4.1.1 Ion exchange chromatography 77

4.4.1.2 Centrifugation 78

4.4.2 Analysis of Al_2O_3 nanoparticles 81

4.4.2.1 Size distribution of Al_2O_3 81

4.4.2.2 TEM imaging of Al_2O_3 nanoparticles 82

4.4.3 Overview 84

4.5 Evaluation of acidic matrix effects on size calibration of gold nanoparticles by a dual sample introduction 85

4.5.1 HNO_3 vs HCl 85

4.5.2 Au droplets vs Au nanoparticles 88

4.5.3 Nebulisation and plasma effect 89

4.6 Evaluation of elemental matrix effects on size calibration of silver nanoparticles by a dual sample introduction 91

4.6.1 Absence of matrix elements 92

4.6.2 Effect of sample gas flow rate on analyte signal at high and low concentrations of matrix elements 94

4.6.3 Effects of low to high matrix concentrations on Ag analytes 98

4.6.4 Correlation of matrix effect with physical parameters of matrices 102

4.7 Application of the microdroplet generator with an inductively coupled plasma time of flight mass spectrometer in the characterisation of particles in environmental water samples 106

4.7.1 A multi-elemental droplet for size calibration of SiO_2-Au NPs 107

4.7.2 Environmental water samples 109

4.7.2.1 Effluent from HCI Building in ETH Zürich 109

4.7.2.2 Water sample from Lake Zürich 111

4.7.2.3 Water sample from Limmat River (Zürich) 113

4.7.2.4 Water sample from Rhine River (Basel, Switzerland) 115

5 Conclusion and Outlook 119

6 Appendix 123

6.1 Abbreviations 123

7 References 125

1 Introduction

1.1 Nanoparticles

The term nanoparticle (NP) defines a substance within the range of 1 - 100 nm in dimension as specified by the European Commission (2011/696/EU): *"A natural, incidental or manufactured material containing particles, in an unbound state or as an aggregate or as an agglomerate and where, for 50 % or more of the particles in the number size distribution, one or more external dimensions is in the size range 1 nm - 100 nm"*.[1] Manufacturers of food products and food packaging material for the EU market need to notify the European Commission of any presence of nanomaterials in the goods which then undergo a safety evaluation prior to approval (Regulation (EU) 10/2011). A similar safety assessment is required for any cosmetic product containing insoluble nanomaterials (Regulation (EC) No 1223/2009). Therefore, quantitative and qualitative analytical methodologies for the determination of NPs. in those complex materials have to be available.

Due to the fact that they are so small in size, their large surface area to volume ratio sets the NPs apart from their corresponding micro- and macroparticles with regard to both their chemical and physical properties. The unique properties of NPs are what make them so attractive in different applications.

Carbon nanotubes and fullerenes, by-products of fossilization, are examples for naturally occurring organic NPs.[2] Inorganic NPs are also formed in biological, thermal and mechanical processes. They occur naturally in the geochemical environment, for example as oxides of cerium (Ce), manganese (Mn), lead (Pb), iron (Fe) and lanthanides. These NPs go through various transformation processes and can be found in soil and water sources as stable sulphates, oxides and colloids.[3]

Ag and Au NP formation in surface waters has been simulated under natural conditions.[3] The presence of a wide variety of organic (e.g. humic and fulvic acids) as well as inorganic material in water plays a role in the photo-reduction of Ag^+ and Au^+ [4] as well as the stabilisation of the respective NPs with other elements, e.g. sulphur (S) as Ag_2S NPs.[5]

Engineered NPs (ENPs) are stabilised to tolerate extreme temperature and high salt content of the environment. Higher 'shelf life' is achieved mainly through capping with polymers such as polyvinylpyrrolidone (PVP) and surfactants (citrates).[6] These features have enabled the commercial applications of NPs to increase considerably in the last few years. At the moment, over 1,800 consumer and consumer related products from more than 30 countries[7] involve the presence and use of ENPs mainly with Ag, Au, carbon and metal oxides.[8, 9] The main industries contributing to the rise in the use of ENPs include health care and consumer products, electronics, textile and the food industry. Oxide NPs are often employed for food preservation.[10, 11] The antibacterial properties of Ag NPs explain the widespread use of these NPs in clothing, health care products and washing machines.[12] The stability of Au NPs makes them promising in the medical field, e.g. use of Au NPs in drug delivery to targeted cells.[13, 14] Metal oxide NPs, in particular ZnO, Al_2O_3, TiO_2 and SiO_2, are extensively used in a wide range of personal care products including cosmetics and household products.[10, 15, 16]

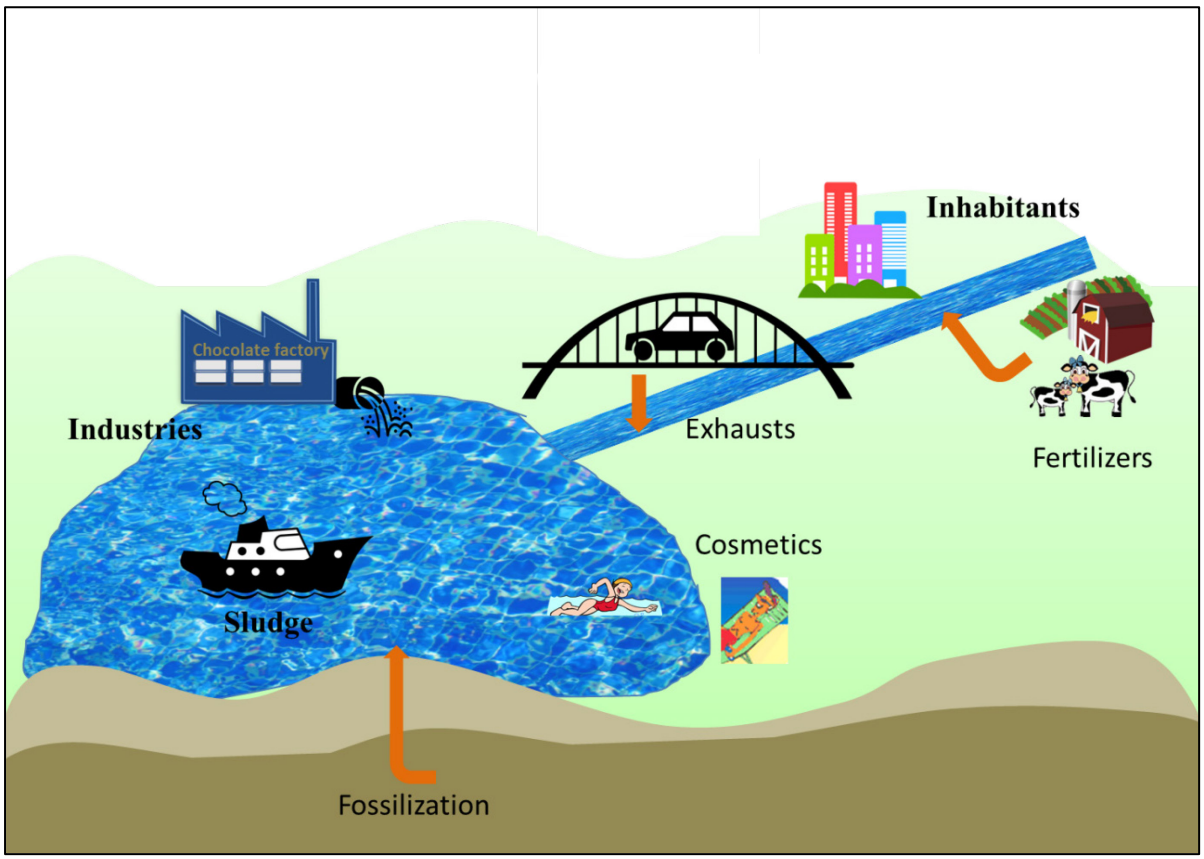

Figure 1: Illustration showing the possible sources of macro- and nanoparticles in the environment, including from industries, motor vehicles, urbanisation and naturally occurring particles.

Stable ENPs may undergo various reactions and transformations upon release in the environment and this makes it challenging to discriminate between naturally occurring NPs and ENPs and their impact on the environment. An illustration showing the leaching of ENPs and naturally occurring NPs into a water body is shown in Figure 1. Several studies investigated the fate of the ENPs and any adverse effect they might impose in the long run.[12, 17] Some cases of toxicity have already been reported with regard to aquatic life,[18] bacterial growth, and even the atmospheric environment.[19] However, the fate of the ENPs is currently not entirely understood, especially in environmentally relevant concentrations and in complex matrices.

The toxicity of NPs can be attributed to 3 different types of mechanisms: 1) release of their metal ions, 2) surface interactions with the surroundings and the subsequent formation of

secondary toxic compounds and 3) any reaction of the NPs itself with other species, e.g. DNA or cell membranes.[20]

Both ZnO and Ag NPs are known to offer antibacterial properties, however it is this same property which can be harmful to naturally present bacteria responsible for decomposition of organic matters in soil and which can lead to their bioaccumulation.[8, 21] NPs present in nature can thus accumulate higher up through food chains.[16]

Several studies have shown that the size of oxide NPs determines their degree of toxicity towards certain species of microorganisms in terms of inhibition of growth and development as well as alterations in enzyme activities.[22-24] Other studies have pointed out that the toxicity of oxide NPs arises from their ionic fraction whose release is regulated by natural organic matter such as tannic, fulvic and humic acids.[25-27] It was found for ZnO that the smaller the size of the NPs the higher the solubility due to the bigger surface area of the particle size.[28] However, a comparison of toxicity arising from Zn^{2+} from ZnO NPs and the Zn^{2+} equivalent from an ionic solution found that ions from NPs were more detrimental to the arthropod studied,[29] indicating that the toxicity is not only caused by ions. The readiness for ZnO NPs to release Zn^{2+} compared to other metal oxide NPs (TiO_2, SiO_2, CuO, etc.) is what most likely makes it more toxic.[20] Natural organic matter (NOM) present in environmental water can dictate the aggregation or dissolution of NPs, a similar role to the one that polymers play as coatings in engineered NP sample. Tuoriniemi *et al.*[30] have addressed the different properties of NPs particularly size, composition, shape and concentration and have shown that these can explain their desired features as well as toxic effects attributable to them.

In the environment, the characteristic of the NPs present is unknown and therefore in the analysis of an environmental sample, an instrument which would satisfy a qualitative as well as a quantitative analysis is required. With the growing commercial use of NPs, it has become increasingly important to be able to evaluate the fate and stability of engineered metal oxide

NPs to address and prevent any toxicity issues. Many natural NPs and ENPs have different compositions, which require a multi-element and multi-isotope characterisation of the NPs in order to utilise this distinction to improve NP detection and characterisation.

Several analytical methods are available for characterisation of NPs in terms of their morphology, size and aggregation state. Microscopic techniques such as scanning electron microscopy (SEM)[31] and transmission electron microscopy (TEM)[32] are the most commonly used methods on samples with a concentration starting at 10^9 particles L^{-1}. Electron microscopy techniques can provide high spatial resolution, size distribution and shape of each single particle. However, these methods do not provide any information about the elemental composition of the NPs. Additionally, sample preparation can be time consuming and interfere with the original state of the particles. In terms of obtaining the chemical composition of NPs, X-ray diffraction (XRD)[33] and atomic force microscopy (AFM)[34] are useful tools for surface analysis. Another rather straightforward and simple analytical technique is dynamic light scattering (DLS),[35] which is most often used as complementary technique or as a quick way to get an idea of the content of the sample. DLS provides the particles' hydrodynamic size information but at a poor sensitivity without differentiating between aggregates and larger particles.[35]

Detectors are combined with different separation and fractionation techniques for characterisation of size, shape and mass of NPs. Some of these separation methods include filtration,[36] using pores of different sizes, usually < 0.4 μm, or ultracentrifugation.[37] Hydrodynamic size chromatography (HDC)[38] is another physical separation technique, where the NP sample is eluted from a column consisting of inert silica particles so that particles of higher hydrodynamic size experience a higher velocity and elute earlier. A recently used chromatographic method in the separation of NPs is the reversed phase chromatography (RP-HPLC) which has been shown to work well for particles < 60 nm.[39, 40] Asymmetric field flow fractionation (AF4) is a technique which is quickly gaining recognition for analysis of NPs

due to its higher resolution in size separation.[41, 42] This technique is based on the particles being injected into a laminar flow in a narrow channel while at the same time experiencing a perpendicular force field by a second liquid flow. Thus, within the thin channel, a parabolic flow profile is created. The bigger particles with lower diffusion rate closer to the edge of the channel travel at a slower speed and smaller particles at a higher position in the channel travel faster. More recently, AF4 has been hyphenated to an inductively coupled plasma mass spectrometer (ICP-MS) to detect NPs in different fractions of eluents. However, the low recovery rate and limited selectivity are still a problem.[43-46]

Currently there is not a single method that can satisfy all needs to characterise NPs and more importantly be applied to more complex NP systems, such as environmental samples which involve different elemental compositions, polydispersity and low concentration. However, one of the most promising methods most often applied for NP characterisation is inductively coupled plasma mass spectrometry.

1.2 Inductively coupled plasma mass spectrometry

ICP-MS was first described by Houk *et al*.[47] and became commercially available in 1983. Since then, ICP systems have been sold worldwide with the main fields of application in industry,[48] geology[49] and environment.[11, 50] What makes it such an attractive tool is its ability to carry out multi-elemental and quantitative analyses at a large dynamic range of concentration from parts per million (ppm) to parts per trillion (ppt) levels.[51] The high resolving power of the instrument offers the possibility to differentiate isotopes and quantify most elements in a very short time. Nowadays, with the growing demand in NP production and characterisation, there has been a revival in its usage and advances in more sensitive and selective instrumentations. In comparison to other analytical methods matrix effects are not pronounced and the instrument can easily be calibrated by liquid standards, so that quantitative results with good accuracies are achieved.

The different types of ICP-MS available today have the most important hardware in common: sample introduction system, plasma torch, interface and mass analyser as illustrated in Figure 2. The sample introduction system can handle both: liquid samples are introduced through a nebuliser and a spray chamber and solid samples can be introduced via a laser ablation system (LA). Eventually, no matter what the nature of the sample was, they are introduced as aerosols into the plasma torch.

However, one major drawback of the ICP-MS instruments is found in the sample introduction system: only 2 - 10 % [52-54] of the sample can be transferred into the plasma with a typically used sample introduction method. This percentage is dependent on several factors: the nature of the sample, the temperature at which it enters the plasma as well as the flow rate and the nebuliser design. It has been shown that the transport efficiency can be as high as 60 % with the use of low sample uptake rates of < 10 uL min^{-1} and up to 90 % with a heated spray chamber.[55] The design of sample introduction systems is constantly being improved. However, the low transport efficiency is still the Achilles' heel of ICP-MS.

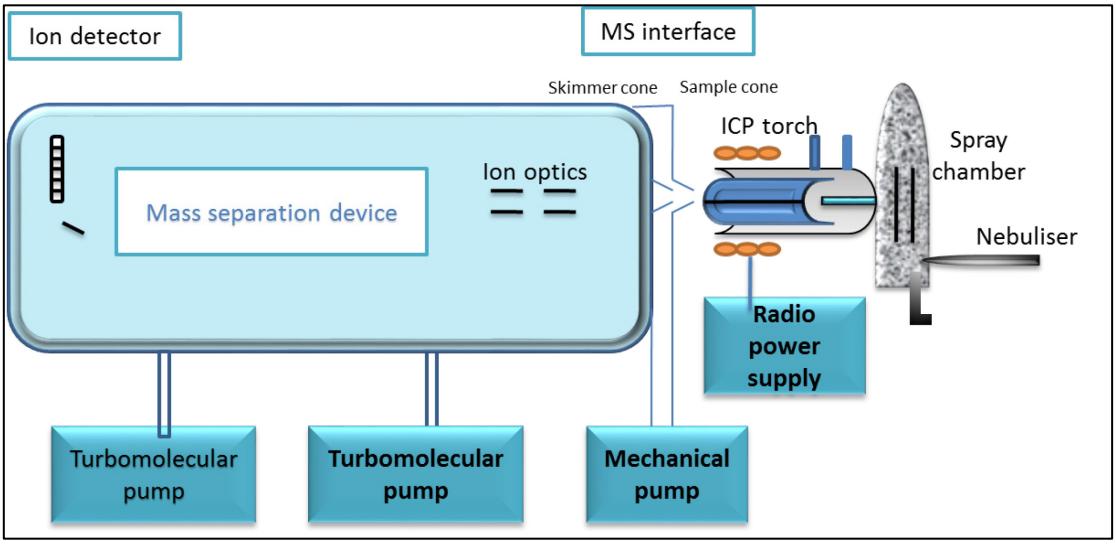

Figure 2: Schematic diagram of an ICP-MS showing the basic components adapted from Thomas.[53] The sample travels through the nebuliser to the spray chamber. The nebulised droplets are then vaporised, atomised and ionised in the ICP torch before travelling through the ion optics. The ions are then sorted in the mass analyser part depending on their mass to charge ratio before reaching the detector.

The mass separation device can be in the form of a quadrupole, sector field or time of flight instrument. The final destination of the ions is the detector. In a conventional mode, the sample is introduced into the ICP-MS instrument through a nebuliser forming an aerosol. Large droplets are removed in a spray chamber. The resulting fine aerosol then enters the plasma. The droplets then enter the plasma torch, the ionisation region of the instrument. The plasma is formed when an argon (Ar) flow is passing through the torch and an electromagnetic field is created by a radiofrequency (RF) generator. A high voltage spark produces free electrons which are accelerated, causing ionisation of the Ar gas. A plasma is created at the end of the torch with a temperature of 6000-10000 K. The plasma is maintained by a constant RF electrical energy, and feeding of Ar through an inlet in the torch. As the sample droplets travel through the plasma, the solvent evaporates and a solid particle is formed which vaporises as it travels deeper into the plasma. The element in the particle atomises and eventually ionises in a region known as the normal analytical zone (NAZ).[51, 53]

The ions then make their way to the interface region which consists of two cones at a vacuum of 1 - 2 Torr. The first one, known as the sampler cone, is followed by the skimmer cone, each with a small outlet to allow the ions to be extracted efficiently into the ion optics behind. The sample ions then make their way through the ion optics, electrostatically controlled lens components. These focus the ions into the mass analyser while at the same time eliminating any neutral species and photons which may be formed during the ionisation process in the plasma. This is essential as these species cause high background noise and signal instability.

1.3 Mass analysers

The mass analyser filters the ions depending on their mass-to-charge-ratio (m/z). Two detection modes are possible: in the scanning mode ions are detected one at the time and in the simultaneous mode, more than one ion signal arrives at the same time at the detector. The mode of ion separation and detection depends on the type of instrument being used. The

quadrupole, magnetic sector field and time-of-flight instruments are the most common types of mass spectrometers available and have all been applied in the course of this project and thus will be discussed in more detail in the following chapters.

The performance of a good mass analyser is dependent on how well it can separate two adjacent peaks, one being the analyte isotope of interest and the other any matrix interference that has a similar m/z value. The resolving power, R, is the term used to determine its ability to separate different masses.[56] R is given by:

$$R = \frac{m}{\Delta m} \qquad (1.1)$$

where m is the nominal mass of the analyte and Δ m is the mass difference between the resolved adjacent peaks.

1.3.1 Quadrupole mass analyser

The most commonly used mass analyser is a quadrupole. Mainly because of its comparatively low price and because it offers a mature technology since it was the first commercialised MS, it is suitable for routine analysis as well as a bench-top instrument. The quadrupole, as its name suggests, consists of opposite pairs of four rods, where each opposing pairs are linked electronically. When the ions enter the set of rods, a particular radio frequency (RF) potential applied determines the analyte ions that will have a stable trajectory down to the end of the rods. The analyte ions of different m/z values will travel in an unstable manner and will be ejected from the quadrupole. For multi-element analysis, the scanning process is repeated with different AC/DC voltages as shown in Figure 3. At the exit of the quadrupoles, the ions are detected in a multichannel detector as electrical pulses in the so called pulse counting mode or as voltages in the analogue mode.[53, 54] Both modes are often combined to extend the linear dynamic range. Signal intensities are measured therefore in both modes as counts per second (cps), but a cross calibration of detectors is required to guarantee linearity.

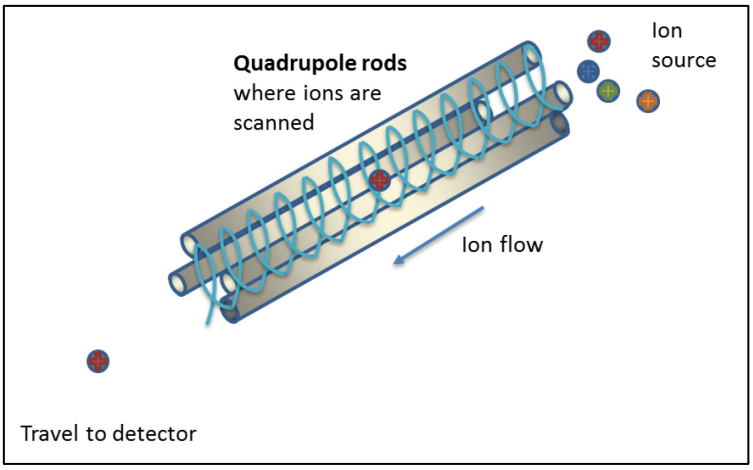

Figure 3: Schematic of a quadrupole mass analyser showing the entrance of ions of different masses but based on the AC/DC potential applied on the opposite set of rods, ions of a particular mass will travel further to the detector. Diagram adapted from Thomas.[53]

1.3.2 Sector field mass analyser

Although the quadrupole instrument is very attractive for routine analysis, one of its drawbacks lies in the maximum resolution it can offer especially when the analyte element is likely to be associated to spectral interferences. The sector field mass analyser (SF) has been developed to address the shortcomings in mass resolution of the quadrupole instrument. It allows the analysis of otherwise problematic elements (iron, potassium, arsenic) and allows an isotopic analysis, while at the same time covering a wider dynamic range. SF instruments applied in ICP-MS commercially, are mainly based on the 2 different double focussing approaches, the Mattauch-Herzog[57] and the Nier-Johnson geometry,[58] and consist of two analysers, an electromagnet for mass separation and an electrostatic analyser (ESA) for energy correction.[59] The geometry of the Mattauch-Herzog analyser allows the ions to be focussed simultaneously onto a focal plane such that detection of all ions at the same time (simultaneous detection) is achieved (Figure 4a). In the standard Nier-Johnson analyser, the ESA is located before the electromagnet and in the reverse geometry, the ESA is found after the electromagnet as shown in Figure 4b.

By varying the width of the entrance and exit slits, the resolution of the instrument can be increased, but the sensitivity is compromised. However, in terms of resolving power and sensitivity, the SF is the better choice compared to a quadrupole instrument. In this work a sector field ICP-MS with a reverse Nier-Johnson geometry (Element XR) has been used which offers three predefined resolution settings (low resolution LR = 400; medium resolution MR = 4,000; and high resolution HR = 10,000).

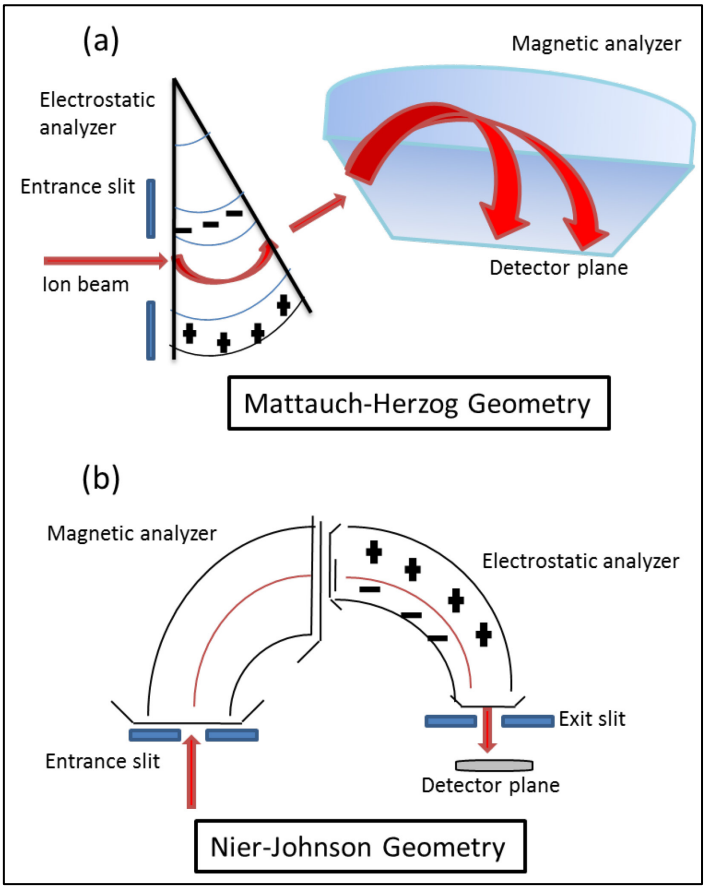

Figure 4: Adapted schematic diagram showing the configuration of 2 double focussing sector field analyser: in Mattauch-Herzog Geometry[60] the ions enter the ESA followed by the magnetic sector (a). In the reverse Nier-Johnson configuration the location of the analyser is the other way round and the ions travel from the magnetic sector to the ESA (b).[59]

1.3.3 Time of flight mass analyser

The time of flight (TOF) instrument displays a distinct advantage over the more conventional scanning mode of quadrupoles and most SF instruments by offering a simultaneous mode of

measurement. An orthogonal ICP-TOF-MS was first described in the multi-elemental characterisation by Hieftje *et al.*[61] In an ICP-TOF-MS, the ions coming from the ICP are accelerated by an electric field applied at the acceleration region. Then they enter a field free region, the drift/flight tube, as packets.[62] The kinetic energy (KE) of the ions is identical. Below is the relationship between KE and the mass (m) and velocity (v) of the ions. The velocities

depend on the mass such that ions of higher m/z value will travel slower than lighter ions as follows:

$$KE = \frac{1}{2}mv^2 \qquad (1.2)$$

The time t to travel in the tube over a distance L, will differ and the ions are separated according to the following equation:

$$m/z = \frac{2vt^2}{L^2} \qquad (1.3)$$

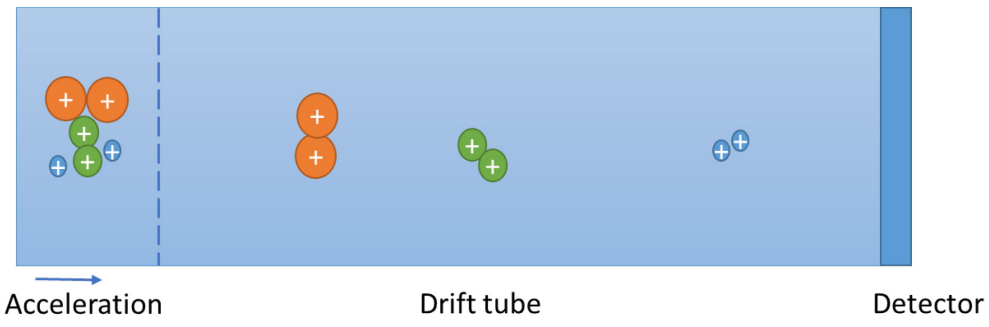

Figure 5: Schematic of a TOF mass analyser showing the separation and detection of ions with 3 different m/z ratios. The ions are accelerated in the acceleration region and obtain the same KE. They travel and separate through the drift tube according to their m/z ratio before reaching the detector, the lightest ions reaching the detector first.

The TOF mass analyser separates the ions according to their m/z, collects them as ion packets to be detected after a given time, as shown in Figure 5. This allows isotope separation and detection of the ions in a quasi-simultaneous way. Any interference such as neutral species

and photons are removed by different deflection plates in the analyser to ensure maximum sensitivity and minimum background signal.

In reality, ions of the same m/z have a slight difference in KE; that leads to a poor resolution. However, this energy spread can be compensated by using a reflectron, a type of ion mirror that reflects ions back.[63] The ions with more energy will travel deeper into the reflectron and those with lower energy will travel a shorter distance such that the spread of drift time is compensated and the ions of the same m/z reach the detector at the same time. Figure 6 is a schematic diagram of a TOF analyser which has been used in this investigation, showing the main components of the analyser.

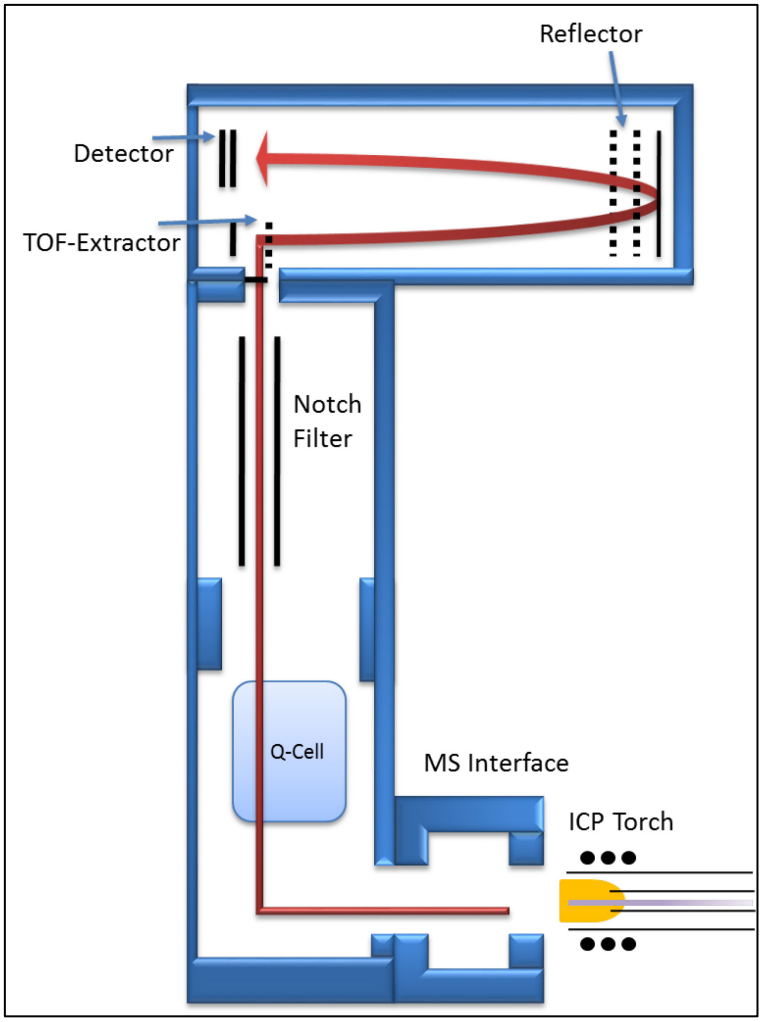

Figure 6: Schematic of an orthogonal ICP-TOF-MS instrument adapted from www.tofwerk.com. The ions are extracted from the ICP interface and travel through the notch filter, where selective ions are attenuated. The reflectron corrects for the energy spread of the ions of identical m/z ratios.[64, 65]

With the TOF system, the ions are analysed at the same time. This capability makes the TOF analyser attractive when analysing samples of different elemental mixtures. In this respect, unlike with the quadrupole and SF instrument, there is no loss of information and time via the scanning and settling time process. The analysis of isotopes with a TOF also offers better precision and a fast transient peak analysis where the entire mass spectrum data can be collected in 30 µs and results in low background noise for both qualitative and quantitative analysis.[64, 66]

1.4 Sample introduction technique

1.4.1 Liquid introduction

Several factors can affect the analyte intensity in an ICP-MS. Already at the sample introduction system the efficiency of the analysis is affected. Apart from the obvious issue of transport efficiency (TE) in an ICP, the type of instrumental parts of the sample introduction system and the choice of gas flows influence the analyte intensity. For a liquid sample, a nebuliser together with a spray chamber is used with argon gas acting as the carrier gas. In conventional methods, a sample flow rate of about 1 mL min^{-1} is common. The transport through the nebuliser can be based on self-aspiration (the sample is being sucked through the nebuliser with a perpendicular Ar flow - 'Venturi effect') or on the use of a peristaltic pump. The nebuliser produces an aerosol which is then transported into the instrument through a spray chamber which in turn attaches to the ICP. Although the nebuliser produces a fine spray of analyte aerosol, the latter is still polydispersed consisting of droplet diameter 1 - 60 µm[67] depending on the inner diameter of the nebuliser and sample gas flow rate. Such a large range of droplet sizes can critically affect the stability of the plasma, i.e. plasma temperature, vaporisation and atomisation of the analyte, as well as the ionisation processes in plasma. The spray chamber helps to reduce the range of the analyte droplet sizes by sieving through the aerosol to eventually be introduced into the plasma. The peristaltic pump is used to remove the waste liquid from the spray chamber.

1.4.2 Nebulisers

The most common types of pneumatic nebulisers (PN) used nowadays in ICP-MS are of the cross-flow design, used mainly for high matrix samples and the concentric design for cleaner samples.[53] PN can be made from glass, quartz or corrosion resistant polymer. The difference in the two designs of nebuliser lies in the way the aerosols are produced.

In the more rugged cross-flow nebuliser,[53] the carrier gas is located at a right angle to the tip of the liquid sample outlet, thus creating an aerosol when gas and sample liquid meet. For routine analysis, this type of nebuliser is preferred as it tolerates high matrix samples and presence of some solid particles. It is more suitable for high throughput analysis since it consists of a larger sample transport capillary. Nevertheless, the larger capillary also means production of droplets of a larger diameter and a drop in the efficiency and sensitivity of the sample introduction.

The concentric design as shown in Figure 7, is the most common nebuliser used in the analysis of clean, low matrix liquids. The sample is aspirated through a narrow capillary, where it comes into contact with a high gas flow at the nozzle. The low sample flow rate (0.1 – 3 ml min^{-1}) and high gas flow rate and pressure give rise to the Venturi effect, such that the sample is self-aspirated and nebulised into a fine aerosol. The sample flow can be regulated by changing the gas flow rate. Microflow concentric nebulisers are designed to create a sample flow rate as low as <100 µl min^{-1} at high gas pressure such that the aerosol consists of droplets of small diameters.[53] These nebulisers exhibit a higher TE than conventional nebulisers and are preferably applied to analysis of samples of low quantity. However, the narrow tubing for the sample uptake causes the set-up to be unsuitable for samples with high matrix loading or presence of solid particles, because the capillary clogs easily. The microflow nebuliser is a preferable system when it comes to coupling a chromatographic system (low flow, low dead volume) to an ICP-MS. The main aim in nebuliser development

is to have a highly efficient tool with as low sample consumption as possible. The benefits of low consumption nebulisers include additionally improved transport efficiency and higher sensitivity. However, the low sample inlet does not work well for a range of matrices.[52] Achieving even higher nebulisation efficiency and being able to introduce concentrated samples to the ICP, the direct injection nebulisers[68] seem to get as close as possible to the desired characteristics of a nebuliser. However, loss in spatial focussing and high background noise is an accompanying issue.

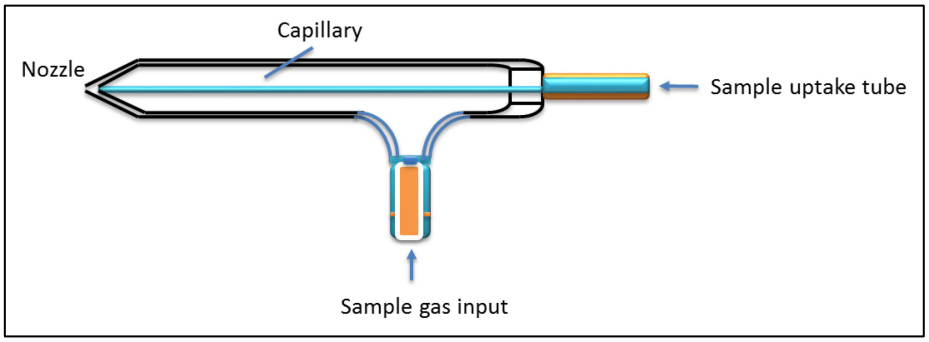

Figure 7: Schematic of a concentric nebuliser as used in this study adapted from Meinhard.[69] The sample is aspirated via a tube and nebulised upon contact with the gas flow.

1.4.3 Spray chambers

The aerosol formed by the nebuliser is known as the primary aerosol, the secondary aerosol is the modified primary aerosol formed on impact with solid surfaces in the spray chamber and the aerosol entering the ICP is known as the tertiary aerosol. As mentioned earlier, the primary aerosol consists of droplets of a wide range of sizes and the use of a spray chamber prevents large droplets from entering the plasma. Tertiary aerosols consist of small and easy-to-desolvate droplets. ICP spray chambers come in different designs: impact bead, Scott double-pass and cyclonic design.

In the impact bead spray chamber (***Figure 8***a), the primary aerosol collides with a glass bead located in the middle lower part of the spray chamber and both big and small droplets are formed. The smaller droplets are the ones which make it to the ICP with the gas flow while the bigger droplets are eliminated by gravitational force down the waste tube. The Scott spray

chamber consists of a long central tube through which the aerosol is directed in a way that the smaller droplets go to the injector and the larger droplets exit via a drain tube.

The cyclonic spray chamber (Figure 8b) works by eliminating the bigger droplets by the use of centrifugal force. The aerosol is transported through a vortex produced by a gas flow; the smaller droplets are transported with the gas flow into the plasma and the bigger droplets, after collision with the chamber wall, go to the waste tube. The cyclonic spray chamber offers high sensitivity and therefore low limits of detection (LOD).[70] Similar to nebulisers, a wide choice of material is available to suit different purposes, such as low flow, resistance to corrosion, and fast wash out.

The spray chamber can be cooled through a cooling system with a temperature below the condensation point of water, just to remove water vapours from the aerosol. This leads to a more stable ionisation process in the plasma due to a more constant temperature level. Moreover, by delivering less water to the plasma, the plasma energy can be used mainly for excitation and ionisation of the sample instead of evaporation.

1.4.4 Matrix effects

1.4.4.1 Acidic matrix effects

Matrix effects occurring during sample introduction are influenced by the concentration and volume of analyte introduced through the nebuliser and the physical properties of the solvent. Changes in aerosol due to increasing acid concentration has a big impact on ICP signals. The size of the droplets making it through the spray chamber depends on the gas dynamics in the spray chamber and the primary and secondary droplet sizes and aerosol density.[71] Analytes of lower densities will be more likely to exit the spray chamber into the plasma. It was found that the overall transport efficiency decreases with increasing acid concentration of the sample.[72] With higher concentration of acid in the solvent, evaporation in the spray chamber is reduced, and the total volume of droplets of < 3 μm in size increases quite dramatically

with an acid concentration of up to 2 %.[73] According to Canals *et al.*,[72] this also includes a decrease in transport efficiency, but how NPs are affected by presence of acidic solvent is still unknown.

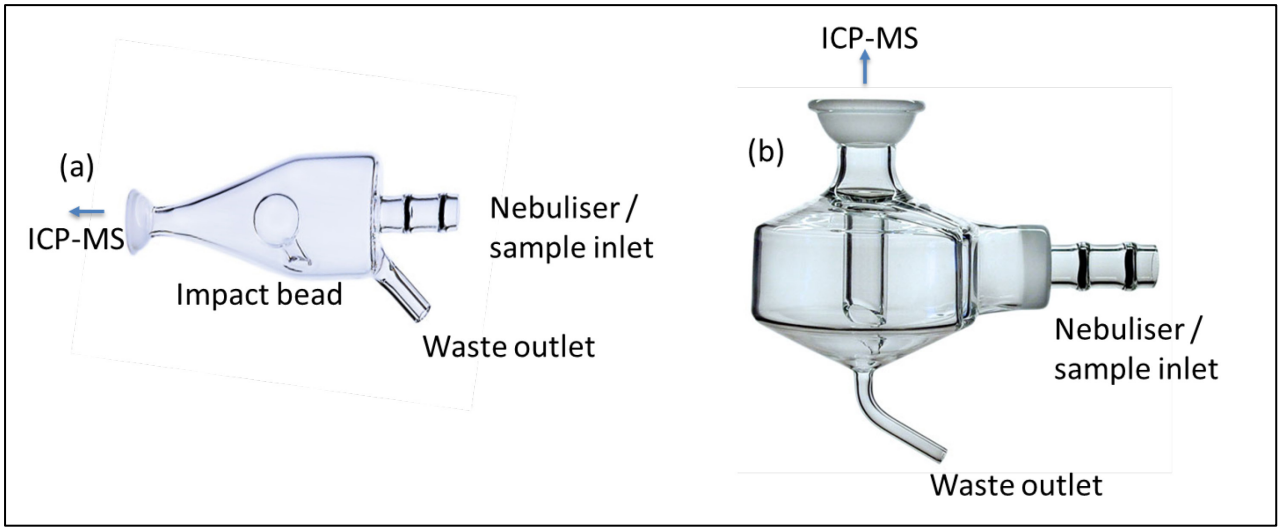

Figure 8: (a) Impact bead spray chamber and (b) Cyclonic spray chamber, both used in this project. The aerosol from the nebulisers enter the spray chambers as primary aerosols. Upon impact with the walls of the spray chamber the sizes of the droplets are altered and most eliminated as waste. The resulting droplets enter the ICP-MS as tertiary aerosols. Pictures are adapted from Meinhard.[69]

The matrix effect from the acid will decrease if water evaporation or drainage in the spray chamber is prevented and a low nebuliser gas flow and high power is used.[71, 73] However, this also reduces the intensity of the analyte of interest by a third. The fact that the instrument is always tuned to obtain a more optimum condition for higher analyte intensity determination does not help in reducing the matrix effect due to acids. Measurement done at low plasma temperature also increases the formation of oxides.[74] The sampling depth can be adjusted instead of decreasing the sample flow rate but this involves working at less optimal conditions. A low sample uptake of 30 µL min^{-1} together with a heated aerosol did not reduce the impact from HCl and HNO_3.[73]

1.4.4.2 Elemental matrix effect

Matrix effects, which can lead to incorrect analysis, take place in the stages of sample introduction, ionisation and ion transfer to the detector. In the presence of matrix, the energy

needed to vaporise and ionise analyte species can be consumed by matrix species, which results in a cooler plasma[75] and in a shift in the normal analytical zone, where the maximum density of singly charged ions are found due to a lateral diffusion of the analyte ions. This type of matrix effect will be referred as a "plasma effect". In addition to changes in ionisation position due to plasma temperature effects, high matrix concentrations can also change relative positions of ions in the plasma due to charge repulsion. This type of matrix effect is generically termed a space-charge effect, and causes analyte signals to be enhanced or attenuated based on each analyte's ion position in the plasma relative to the ionisation position of the matrix species.[76-79]

Horlick *et al.*[80] extensively studied matrix effects caused by low-to-high ionisation potential elements of varying concentration at varying carrier gas flows using a traditional sample introduction ICP-MS. The matrix elements used were of low-to-high mass and the impact of these matrix elements was also assessed on low-to-high-mass analytes with a range of ionisation potentials. The gas flow rates were found to be of high importance. At low nebuliser flows, matrix effects were considerably reduced. The absolute concentration of the matrix affected the analyte, and one way to overcome the matrix effect was by diluting the sample, hence reducing the number of matrix ions being introduced into the plasma.[81] In the case of sampling depth, changes in the gas flow compensate for changes in ionisation point caused by the matrix. However, when it comes to plasma power, the influence on the analyte is rather severe: if plasma power is not at an optimum value, there will be incomplete ionisation of the analyte[82] and, in this non-robust plasma, matrix effects are pronounced.[83] A robust plasma consists of high plasma power and is supported by low nebulisation flow rate and large inner diameter of the central tube in the ICP torch.[81]

Highly ionisable elements cause suppression of analyte ions and this effect is bigger with matrix elements of higher mass.[80] Olesik *et al.*[84] found that the presence of a higher mass element, in this case Pb^+, causes the Li^+ signal to be temporally broadened. They attribute this

observation to a broadening in size of the ion cloud due to a space-charge effect. Li^+ transport from the ICP to the mass analyser is attenuated because higher mass Pb^+ ions repel surrounding lighter Li^+ ions to a greater extent than other ionic species and therefore the Pb^+ : Li^+ number ratio in the region of the plasma decreases.

1.5 Single particle inductively coupled plasma mass spectrometry

1.5.1 Background

Measurement of single particles was performed already in the 1980s when monodispersed aerosol and airborne particles were introduced directly into an ICP atomic emission spectrometer (AES).[85-87] The transient signal produced with a size limit of detection (LOD) of around 0.3 μm for Copper (given diameter 0.2 μm) and the smallest LOD was for calcium oxide at 0.1 μm.[85] In 2003, Degueldre and Favarger[88] introduced a nebulised colloidal solution while expecting the signal in the form of a peak over a defined time to correspond to the amount of ions in a particle. They chose an ICP-MS to improve the LOD of the samples. The authors initially performed a feasibility study on model samples, where no sample preparation of the suspension was required and a small measurement window was used. Each particle was expected to produce an ion cloud in a short time interval leading to single peaks. The intensity of the ion signal would determine the size of the particles being measured and the number of single peaks would relate to the particle number concentration in the colloidal suspension introduced. The colloid suspensions were diluted into water and later nebulised such that one colloid was present in every 10^6 of the microdrops formed and that no double particle event would be detected in the selected time interval. The data was recorded every 10 ms with a dead time of 9 μs. Under these conditions, the detection limit in terms of diameter was as low as 30 nm for Al.[27] They pointed out problems that may arise due to interferences at certain m/z values upon interaction with the matrix elements or Ar gas and therefore underlined that the choice of isotopes is crucial in a spICP-MS analysis. The group went on

to apply the spICP-MS to analyse colloids such as zirconia,[89] thorium,[90] gold (80 - 250 nm)[91] and uranium.[92]

1.5.2 Particle characterisation

In conventional ICP-MS, the introduction of a solution containing dissolved ions will give a steady signal. If that same amount of ions is present in the form of small particles and introduced in the same way, the sample will show signals in terms of spikes over a short duration of time, the time taken for the analyte to be ionised in the plasma and for the ion plume to be transported and detected. Aerosol droplets with the particles will give a spike signal and any droplet without particle will appear as a steady background signal. Therefore, the measurement of the particles demands a fast acquisition rate in a short dwell time of ≤ 10 ms (Figure 9). The short measurement window assures that the particle has undergone total ionisation and is detected, and with a rapid acquisition rate all the particles ionised in the plasma can be recorded as single peaks and no double events are recorded as a single peak.

The intensity of the pulse corresponds to the elemental mass in one particle and eventually to the size of that particle if the density and geometry are known. By summing up the number of pulses produced in a given time and by knowing the transport efficiency of the system, the particle number concentration can be calculated. A size distribution of the particles in that particular sample can therefore be plotted and particle number and mass concentration can be deducted. Systematic approaches have been proposed to characterise NPs[93-95] and have demonstrated the possibility to distinguish and identify dissolved Ag ions and Ag NPs of different sizes.

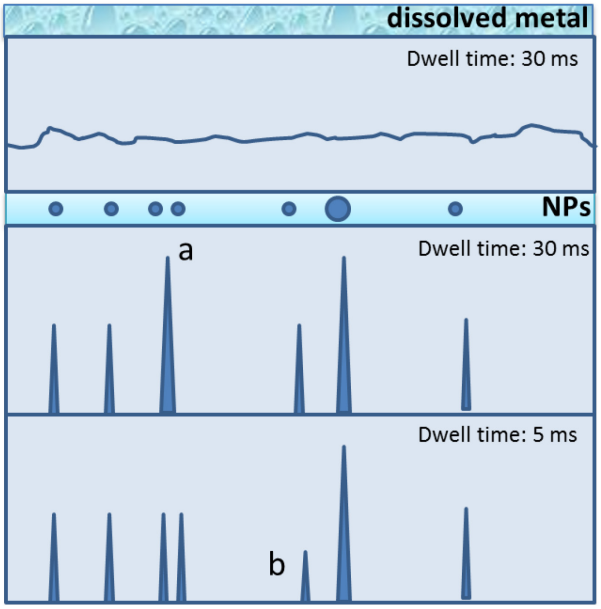

Figure 9: Diagram comparing signal obtained in analysis of a dissolved metal sample as compared to a sample of metal NPs (adapted from Laborda et al.[96]). The chosen time resolution is critical for the measurement of the NPs. At 30 ms, the measurement time is too long such that the signal of 2 NPs arriving close in time will be shown as a high intensity signal making it hard to differentiate against a NP of bigger size as pointed out in (a). When using a low dwell time, there is also risk of split events shown in (b) and the signal could be mistaken for a smaller NP.

Additionally, the use of faster electronics in order to decrease the dwell time and enhance resolution was proposed.[93-95] Mitrano *et al.*[94] also outlined the theory of spICP-MS while screening for Ag NPs in environmental water and pointed out the difficulty in differentiating between aggregates and colloidal NPs.

The basic assumptions in spICP-MS are that 1) each NP pulse recorded corresponds to one NP, therefore the NP samples should be diluted to give 10^3 - 10^5 particles mL^{-1} , 2) every single NP that enters the plasma is detected, 3) the sensitivity of the instrument is the same for the element in its dissolved form as it is in its particle form and 4) the density of the analyte in its elemental form should be the same as in its solid/particle form. Based on this, the following set of equations will hold.[97]

The first equation relates the pulse frequency to the particle number concentration:

$$\frac{q_p}{c_p} = q_s \times \varepsilon_n \qquad (1.4)$$

where q_p = flux (or number) of particles detected in plasma (s^{-1}), c_p = number of particles in the sample (mL^{-1}), q_s = sample uptake rate (mL s^{-1}) and ε_n = transport efficiency (dimensionless). In conventional ICP-MS, the transport efficiency (TE) is defined as the ratio of the amount of analyte that that enters the plasma to the nebulised amount. When it comes to analysing particulates, the suspension should be evenly distributed in the liquid solution so as to ensure that the NPs counted would correspond to the NP number concentration. The parameter abbreviations are taken from Heithmar and Pergantis.[97] Different groups working with spICP-MS use abbreviations of their own.[30, 88, 94, 98, 99] The mass of the analyte element in a single NP ($m_{a,p}$), can be calculated from the following equation:

$$m_{a,p} = \left[\frac{q_s \varepsilon_n c_a}{q_{i,a}}\right] n_{i,p} \; = k \, n_{i,p} \qquad (1.5)$$

where $n_{i,p}$ = number of ions of analyte elements detected in a single NP pulse, c_a = the analyte concentration in a dissolved standard (g mL^{-1}), and $q_{i,a}$ = ion flux measured for the dissolved standard (s^{-1}). To calculate k (response factor), an ICP-MS standard of the dissolved element is used and the same sensitivity for the NP form is assumed. Once q_s, ε_n, have been determined, the calibration for any unknown nanoparticle suspension can be obtained by rearranging equation 1.4:

$$c_p = q_p \, / \, q_s \, \varepsilon_n \qquad (1.6)$$

For a suspension of homogenous and spherical NPs, the diameter of the NPs d_p can be obtained by relating the mass of the analyte to the diameter of a sphere as follows:

$$d_p = \left(6 \frac{m_{a,p}}{\pi \rho_p}\right)^{1/3} \qquad (1.7)$$

where ρ_p is the density of the metal analyte at room temperature (g nm^{-3}).

1.5.3 Transport efficiency

There are different approaches in calculating the transport efficiency ε_n such that the above equations can be used for particle size determinations. The most common method for

characterisation of particles is via the analysis of a reference material of known particle composition, size and concentration, ideally of the same chemical composition and of monodisperse nature.[89] The pulse intensity from the reference material can be related to the mass content or size of the particles and the number of pulses from the sample can give a particle number count. However, the current problem with this method is that reference material is not available for most types of NPs and ideally alternative methods have to be developed in those cases.

The waste collection method is used to obtain the ε_n.[95, 100] In this method, a vial containing the sample and an empty vial for the waste collection are both weighed before the analysis. The sample is introduced into the nebuliser and at the same time the waste is collected into the waste vial. After a defined period of time, both vials are weighed again. From the weight differences of the vials before and after the analysis the amount of the sample that entered the plasma can be calculated by substracting the mass of waste collected from the amount delivered to the nebuliser. The ratio of the mass which entered the plasma to the amount delivered to the nebuliser gives the transport efficiency ε_n. The waste collection method however yielded a high value for the TE, and therefore an underestimation of NP size and number concentration.[95]

Pace *et al.*[95] have proposed a couple of alternative procedures in calculating ε_n. One of which they named the particle size method, where two calibration curves are created: one correlating a known NP mass to the respective intensity and another one relating the analyte mass of different concentrations to its intensity. The slopes of the two curves are assumed to be equivalent and from there the ε_n is determined, as shown in Figure 10. This method holds true assuming that the density of the element in dissolved and particle form both are of the same density. The sensitivity of the instrument to the bulk material should be equal to the sensitivity to the particle. In case of any differences in the conditions applied for the particles

and bulk material, the use of a correctional factor (CF) should be taken into account in calculating the final ε_n.[101]

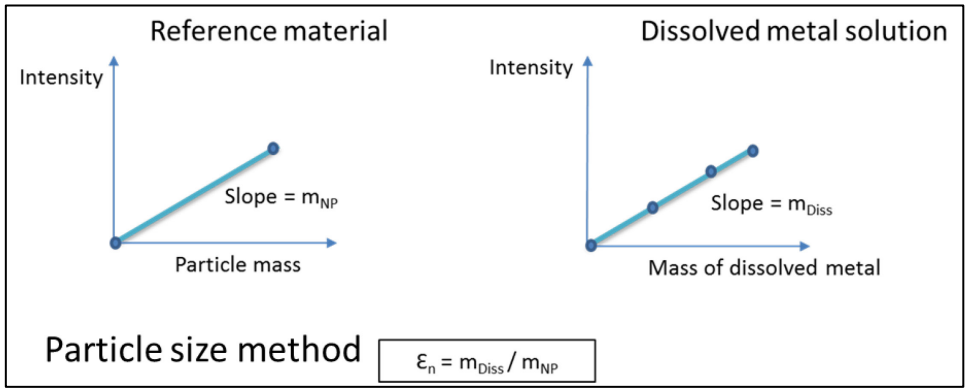

Figure 10: A schematic for showing how the TE value is obtained using the particle size method as described by Pace et al.[95] The ratio of the solution response to the NP response gives the TE; slope of dissolved metal/slope of particle.

Another method proposed, known as the particle number concentration method, is the most commonly used nowadays.[95] A reference material of known particle number concentration is used, such that the ratio of the measured number of pulses in a defined time to pulse frequency of the suspension introduced will give the ε_n. The pulse frequency of the suspension introduced is calculated using the known concentration and the sample flow rate. In this approach, an assumption is that the particle number concentration introduced is the same as what is reported by the manufacturer. Over time, particles may aggregate, dissolve or stick to the walls of the containers they are kept in therefore leading to a wrong estimation in the TE value. In all the methods outlined, a common point lies in the use of a reference material, whether it is to find the size or particle number concentration.

1.5.4 Nanoparticle data collection

The most common data processing for NPs in the spICP-MS is using a threshold to distinguish the particle signal from the noise and dissolved analyte signal. This method, described by Pace et al.,[102] collects data that are above the mean value of the entire data set + 3σ, where σ is the standard deviation of the background in counts, to represent the NPs event, assuming that the background signal follows a normal distribution. The data set below the

threshold are re-averaged and the process is repeated until no data point is obtained above the final mean value. The number of data points collected represents the number of particle events measured and the intensity gives the particle size.

1.5.5 Nanoparticle measurement by single particle inductively coupled plasma mass spectrometry

The analysis of NPs using spICP-MS is very attractive for various reasons, one of which is the requirement of very little or no sample preparation, in most cases the sample only needs to be diluted in water. Therefore the application of spICP-MS, using mainly standard Ag and Au NPs as reference, has found itself a niche in the analysis of NPs in water and waste water treatment samples.[30, 94, 97, 102]

As pointed out previously, this method can not only differentiate between NPs and their dissolved analyte form[93] but can also give a quantitative analysis of the sample content as shown by Laborda *et al.*[93] and Mitrano *et al.*[94] in the analysis of Ag NPs. Offering a wide linear dynamic range and sensitivity, particles can be classified as aggregates/agglomerates or particles in the micrometer range. Reed *et al.*[103] have shown that spICP-MS can be used too in the study of dissolution of commonly used NPs including Ag (both spherical and rod shaped), titania (TiO_2), ceria (CeO_2) and zinc oxide (ZnO). Except for ZnO NPs, the application of spICP-MS was suitable for the analysis of the NPs in water due to the low background level. The dynamic range of the ICP-MS in the sp mode can be extended to analyse particles between 10 - 200 nm by reducing the sensitivity of the instrument via analysis in a high resolution mode, use of a collision cell or using a low extraction voltage.[103, 104]

The highly sensitive and multi-elemental detection capability of spICP-MS also means that samples of unknown composition can be analysed. Borovinskaya *et al.*[105] used an ICP-TOF-MS to simultaneously analyse core shell NPs of Ag and Au composition. With the use of fast electronics and short dwell time,[106] more than 1 isotope can be rapidly analysed.[107]

Hyphenation to several separation techniques makes spICP-MS a unique and innovative technique for the analysis of NPs. With the analysis of NPs in the environment, the importance to determine and characterise a range of NPs sizes in the same sample is more pronounced. Pergantis *et al.*[38] have used a front end hydrodynamic chromatography column (HDC) to separate NPs of 30, 60, 80 and 100 nm prior to analysis via spICP-MS, with the drawback of achieving low resolution separation. Asymmetric flow field flow fractionation (AF4)-spICP-MS has also been applied to separate NPs from enzymatically digested chicken meat with a recovery of 80 %.[108] Sedimentation FFF (SdFFF), a higher resolution separation technique, coupled to spICP-MS was used to obtain a size distribution of TiO_2 NPs. The broad size distribution of the TiO_2 colloidal samples was initially separated into narrower size groups then analysed by spICP-MS to obtain a size distribution of the fractions collected after SdFFF.[109] With a focus on environmental analysis, ion exchange chromatography (IEC) hyphenated to spICP-MS was applied to characterise and quantify ZnO NPs.[110, 111] With a high rate of dissolution, ZnO NPs samples are complex to analyse. With this method, a separation of NPs from the ionic solution can be achieved and a size distribution obtained. More recently, Sötebier *et al.,*[39] used a combination of isotope dilution analysis (IDA) and high performance liquid chromatography (HPLC)-spICP-MS for the separation of Ag NPs and their ionic content. This method was found to not be favourable for particles larger than 60 nm due to the latter's interaction with the stationary phase. However, these above mentioned hyphenation techniques show a great potential in the application of spICP-MS to more complex NPs samples in the environment or biological studies.

SpICP-MS has proved to be a superior technique compared to a range of other techniques for the analysis of NPs with its accurate measurement of size and concentration as well as being able to distinguish between aggregates, single particles and dissolved ions in one single measurement window.[93] It should be noted that most of the applications and research to improve the technique are done on well-defined and characterised Au and Ag NPs obtained

e.g. from U.S. National Institute of Standards and Technology (NIST) and Nanocomposix. Hence, they are applied mainly for academic purposes.

1.5.6 Limitations of single particle inductively coupled plasma mass spectrometry

However, there are some challenges in the analysis of NPs by spICP-MS. Currently spICP-MS involves the use of a certified reference material for obtaining the size and/or concentration of unknown NPs. The specifications of the reference material given by the manufacturer must be trusted or additional imaging techniques must be used prior to spICP-MS analysis in order to get the correct NP size and shape information. Currently, there are only a few reference materials from NIST (Au NPs (RM 8011, -8012, -8013), Ag (RM 8017), polystyrene sphere (SRM 1964, -1963a) and TiO_2 (SRM 1898)), from the Bundesanstalt für Materialforschung und -prüfung (BAM) (Ag (BAM N001)) and from the Institute for Reference Materials and Measurements (IRMM) (SiO_2 (ERM FD100 and -304)).

SpICP-MS can be used for a range of NPs with different elemental compositions, but the reference material used in their determination is still Au or Ag. If the elements of the sample and reference material differ the chemical properties and ionisation potential of the reference NPs and the sample are different[112] and therefore any subsequent calculations may not be accurate. Another issue lies in the sample introduction part of spICP-MS: NPs are known to stick to the walls of the glassware[113] and this can lead to an underestimation in the subsequent calculations of particle number concentration. Since the arrival of NPs in the instrument can be erratic, it is not possible to ensure a uniformly distributed NP sample; some NP signals may be lost in the settling time window of the instrument. Fast scanning modes have been proposed with the SF[114] and quadrupole[106] instruments, where the acquisition time can go down to 1 µs. However, the settling time needed between measurements is still the drawback in using these mass analyser to look at unknown NP samples. Although spICP-MS can give qualitative information about several elements present in an unknown NP sample, the

commonly used quadrupole and SF mass analyser are only able to detect one isotope at a time in the scanning mode.[115] Borovinskaya *et al.*[116] developed a prototype ICP-TOF-MS instrument where a quasi-simultaneous detection was performed on core shell NPs. More recently, a new commercial ICP-TOF-MS has been introduced offering high speed and simultaneous detection.[64]

One alternative introduction system which can overcome many of the limitations of conventional nebulisers including the need for reference material and which will be investigated in more detail for NP detection in this work is based on introduction of monodispersed droplets.

1.6 Monodispersed droplet introduction

1.6.1 Background

As described previously, one of the biggest sources of error in an ICP-MS analysis lies in the sample introduction technique. The use of a nebuliser and spray chamber not only results in only 2 - 10 % TE[53] but also in a disorderly arrival of the sample in the plasma. This may interfere with the normal sample vaporisation, atomisation and ionisation process due to fluctuation in the plasma temperature. These processes therefore take place at different points in the torch, possibly resulting in loss of ions or occurrence of matrix effects. A few improvements have been made over the years in order to develop the analytical capability of the technique and one of them was to improve the TE of the sample into the plasma.

The first concept of introducing samples as droplets was put forward by Hieftje *et al.*[117-120] with the production of a liquid jet. These then mechanically 'broke up' to form monodispersed droplets. The droplets were introduced into a flame for the purpose of studying the vaporisation, ionisation behaviour and the shape of ion cloud formed from single particles. Since the droplets entered the plasma with the same interval, a better insight into spatial and temporal resolution was obtained.

Coupled to an ICP device, an improved droplet dispenser known as the monodisperse dried microparticulate injector (MDMI) was designed by French *et al.* with the aim of reducing oxide formation and interference while eliminating nebuliser induced noise and allowing a 100 % sample consumption.[121] The droplet injector works on the principle of a piezo-element: with the application of a voltage monodisperse droplets are produced. By varying the pulse's width and height on the piezo, the size of droplets as well as their initial ejection speed can be altered. The frequency of the droplet formation can range from 1 to 6000 Hz. With a laminar flow of heated Ar droplets enter eventually the plasma as dried particles, maintaining a near zero turbulence as well as resulting in a small enough gravity, so that a horizontal trajectory into the plasma is possible. The 100 % sample introduction system also includes lower oxide interference and consequently gives a lower noise level. By optimising the gas and droplet velocity, the temporal jitter in the arrival of the droplets entering the plasma was minimized. The resulting relative standard deviation of 6 - 8 % in the peak height and area of the monodispersed droplets opened the door for further investigating droplet-plasma interactions.[122] The transport processes in an ICP-MS was investigated with the use of the time resolved droplet introduction via MDMI. For this purpose, different easily ionisable elements were introduced at the same time and the ion interactions were observed. A mass dependent space charge effect was found to occur after the ionisation process of the analyte ions in the plasma,[84] more precisely in the ion optics.[123] Using a twin quadrupole ICP-MS, simultaneous measurement of high concentrations of Li^+ and Pb^+ was performed in order to study the location of matrix interaction and the resulting signal shape from the analyte ions. By adjusting the voltage of the lenses, the region where matrix effects occur was found to be between the skimmer and extraction lenses and within the ion optics.[123] To improve reproducibility in droplet arrival, the MDMI was also connected in a vertical manner where the reproducibility of the droplet arrival was also better in the long term.[124]

1.6.2 Microdroplet generator

Research about using discreet droplet introduction to study desolvation in plasma took off again after a commercial microdroplet generator (MDG) became available. The commercial droplet generator is based on a similar design as the MDMI introduced by French *et al.*[121] The basic components of the MDG consist of a dispenser head, an electronic control box and a sample reservoir.

The MDG used in the experiments in this thesis was the MD-K-150 from Microdrop Technologies GmbH, Nordstedt, Germany. A schematic and photos of the instrument used are shown in Figure 11. The liquid reservoir (sample vial, Figure 11b), has a capacity of up to 5 mL and is connected to the dispenser head's nozzle via a tube which feeds in the sample (Figure 11a). Air pressure, applied through a syringe, pushes the liquid through the tube to the dispenser head via an air inlet with a filter at the top of the cover of the sample vial. The electrical part of the MDG (Figure 11c) is also connected at the top of the dispenser head.

Within the core of the dispenser head is a glass capillary connected at one end to the liquid reservoir and at the other end it forms a nozzle through which the droplet is generated. To a piezo actuator tube, surrounding the capillary, short electric pulses are applied which generate short pressure pulses in the liquid and produce the droplet at the nozzle tip. Droplets are therefore ejected at relatively high initial speed. Upon ejection, the velocity of the liquid decreases due to reduction of the pressure after liquid expansion at the nozzle tip, after which a capillary tubing sucks up fresh liquid from the reservoir after ejection of each droplet. The voltage applied to the piezo actuator is controlled by the electronic box. By adjusting the voltage and the duration of the electrical pulse the size of the droplets and their initial acceleration can be controlled. The pulses applied can be in the form of a single pulse or triple pulses. The single pulse mode produces droplet sizes proportional to the diameter of the dispenser nozzle, whereas in the triple pulse mode, smaller droplets can be produced even if

larger nozzle tip diameters are applied. The use of a larger nozzle tip decreases risk of clogging that may occur depending on the sample used. In the MD-K-150 model, the top dispenser head also consists of a gas inlet which can be used to carry the droplet in a gas sheath.

Complementary to this dispenser head, nozzles of 30, 50 and 70 µm in diameter can be used to produce droplets of a volume ranging from 20 to 380 pL. With a frequency of up to 2,000 Hz, the droplets can be formed with a high reproducibility in the volume of the droplets. The viscosity of the liquid is very critical to the size of the formed droplets and a realistic liquid would have viscosities between 0.4 and 20 mPas and have an ambient temperature of up to 80°C. Any unsuitable liquid would result in unstable droplet formation and ejection and the possibility of introducing air bubbles in the capillary. The physical characterisation of the liquid and the nozzle diameter chosen have a direct effect on the size of the droplets and the initial speed of droplet generation.

Since the droplets formed are too small to visualise, a strobe light in combination with a CCD camera is used to capture images on a screen. This will enable the user to judge the suitability of the voltage applied to have a satisfactory droplet formation. The size of the droplets and the velocity of the droplet formation can be thus measured.

1.6.3 Microdroplet generator inductively coupled plasma optical emission spectrometry

The commercial MDG was used together with an ICP-OES instrument to study droplet desolvation and vaporisation in the plasma in a simultaneous end-on observation by the use of three monochromators for the measurement of lines of hydrogen, the analyte and Ar.[125] It has been found that for small droplets (<50 µm) the plasma conditions are not as much affected during desolvation of water molecules as they are affected during the atomisation process. The authors also used a combination of side and end-on analysis to conclude that the plasma behaviour both in an ICP-MS and – OES strongly depends on the Ar carrier gas flow

rate, the size of the droplets and the size and position of the ion clouds formed. With the introduction of a high Ar flow rate and bigger droplet size, a plasma cooling results which in turn shifts the position of the atomisation point.[126] The MDG can also be used to investigate how to improve the detection efficiencies of the analyte in the plasma.[127]

With the advancement in NP characterisation techniques, a calibration strategy using the MDG and ICP-OES was introduced by Garcia *et al.*[129] The size calibration was done for Au (0.25 µm) and SiO_2 (0.53 - 2.06 µm) particles using dissolved Au and Si solutions as an external calibration to calculate the size of the corresponding particles. Calcium solution was used as a marker to follow the droplet introduction and frequency. The MDG was connected in a vertical position to the ICP so that no droplets were lost on the way to the plasma. Through these sets of experiments, the authors deduced the size limit of plasma ionisation for particles to be < 2 µm.

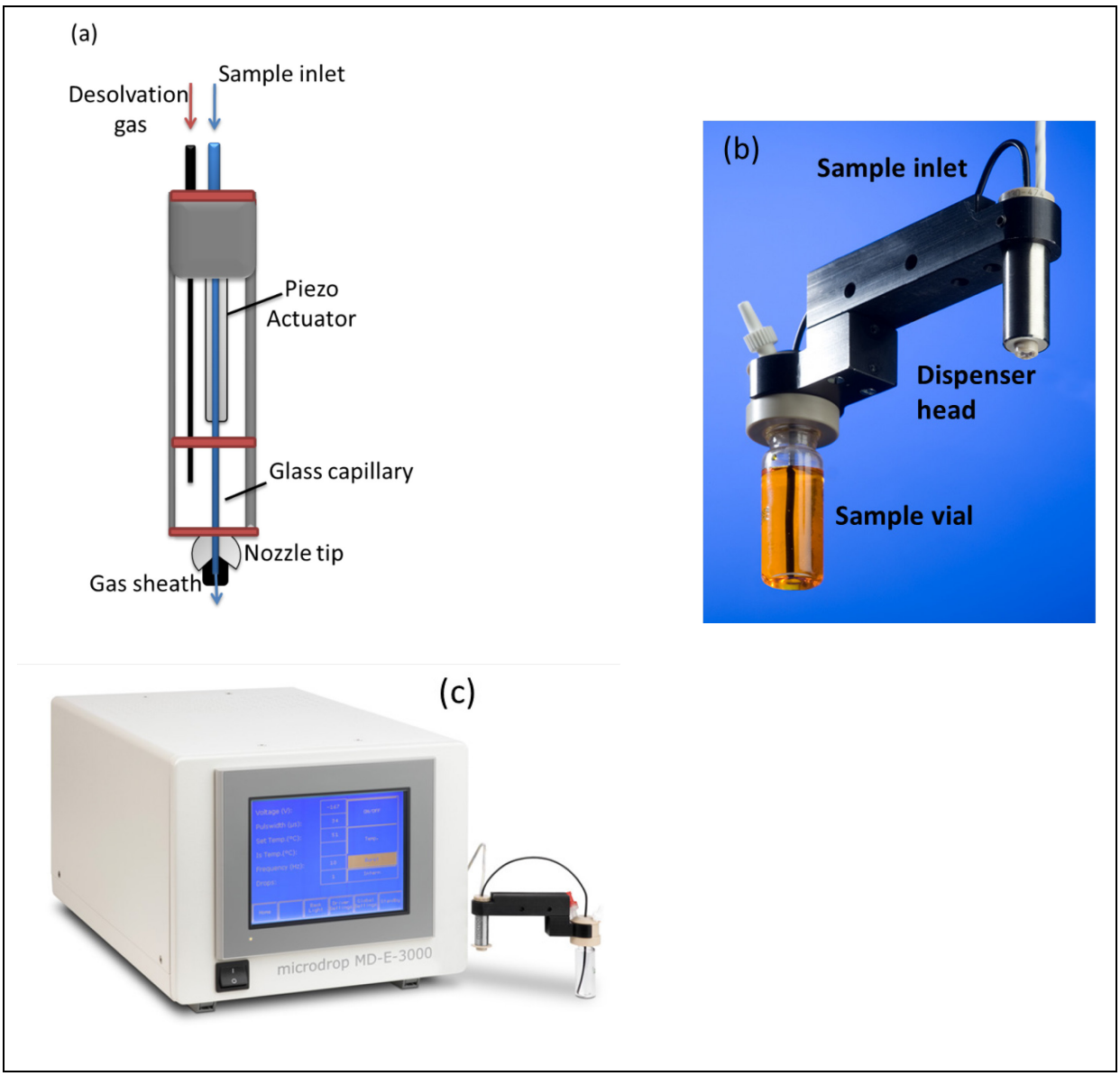

Figure 11: (a) Diagram showing the interior of a dispenser head. The sample is introduced into the MDG through an inlet and exits at the nozzle as droplets. (b) Connection between the sample vial and the dispenser head where the sample travel via a tube to the sample inlet of the MDG. (c) Control box, through which the generation of the droplets can be adjusted in terms of size, frequency and velocity. Picture (b) and (c) are adapted from microdrop Technologies GmbH.[128]

1.6.4 Microdroplet inductively coupled plasma mass spectrometry

This calibration technique was transferred to an ICP-MS that could satisfy a lower limit of detection for the analysis of NPs. To be able to introduce the droplets in a vertical manner so as to assure the drying of the particle, Gschwind *et al.*[129] developed an adapter to connect a vertical connecting tube to the ICP inlet in an airtight condition. To direct the droplets into the plasma without any losses, an investigation was undertaken to find the right carrier gas.

Using a computational modelling system to find the right gas, it was found that He induces a faster drying process on droplets than Ar.[130] A comparison was made between Ar and Ar-He gas mixtures regarding the transport of droplets down a vertical tube, where it was found that the mass transfer rate from the Ar-He mixture was higher.[129]

In a first characterisation experiment on Au and Ag NPs, the MDG was connected in a vertical position for the entrance of the droplets in the plasma.[129] Helium was chosen as the most suitable carrier gas down the tube as it not only is the best gas to be used to dry the droplets without the use of an oven as was previously needed,[121, 122] but also ensures that the droplets would not crash at the bottom of the T junction due to gravitational forces. The droplet diameter generated by the MDG was < 40 μm and by the time it reached the injector of the torch the diameter has decreased to ~ 1 μm by desolvation. Just like in spICP-MS, dwell time is an important value in this procedure. With a lower dwell time, the signal sensitivity would be higher. However, a dwell time too low will result in inadequate signal measurement. With a quadrupole analyser, the lowest dwell time used was 12 ms.[129] Dissolved solutions of Cu, Ag and Au were analysed in the form of droplets and the Ag and Au NP suspensions were also introduced as droplets after being diluted to ensure one NP per droplet. The MDG was used in the single pulse mode and TE were close to 100 %. The LODs in terms of particle diameter for Au and Ag particles were 21 and 33 nm, respectively, which was lower than any LOD in a conventional mode of analysis due to the low background noise. A similar vertical set up was used by Shigeta *et al.*[114] In this case, He was introduced only through the MDG at almost double the total flow as done by Gschwind *et al.*[129] The MDG, coupled to a SF analyser in this case was used in a triple pulse mode where the average size of the droplets formed was 23 μm, resulting in a TE of 100 %. In the single pulse mode, a TE of only 20 % was achieved with droplets of 70 μm.

In a different configuration, Gschwind *et al.*[131] introduced a new 3D printed adapter which was lighter, consisted of four symmetrical gas inlets and a glass window to view droplet

generation and would easily couple to the torch of commercial ICP-MS. For the droplet transportation, the falling tube was also made of lighter material. The adapter was used both in a horizontal and vertical position. The vertical setup was found most suitable for droplets of < 95 µm, whereas smaller droplets of < 43 µm were analysed after horizontal sample introduction. The TE in both cases were found to be > 95 %. The temporal jitter was decreased from 10 ms to 2 ms in the horizontal setup due to the lower transport time needed. A low dwell time of 0.1 ms was achievable since the experiments were done in a SF instrument. The MDG was also coupled with a prototype ICP-TOF-MS to detect composite NPs of Au and Ag simultaneously.[105] More recently, a new ICP-TOF-MS was made commercially available. The capabilities of the new instrument were assessed with both a MDG and PN for conventional sample introduction and show a significant improvement over the prototype ICP-TOF-MS in terms of resolution, limit of detections and high speed analysis.[64]

2 Aim and objectives

ICP-MS has become one of the most important analytical tools for characterisation of NPs and spICP-MS is already established to measure mass, size and number of metallic particles in suspension. But spICP-MS is not a primary method and thus needs calibration by standards for quantification. However, standard reference materials are rarely available for most novel NP systems and thus novel and traceable calibration methods are needed for spICP-MS.

Thus, it is the aim of this study to develop a new method based on traceable, liquid standards for quantification of metallic NPs. A combination of a MDG and a nebuliser was considered to be a system by which this aim could be achieved. To develop and characterise this new system different steps had to be performed resulting in 5 main objectives for this work.

Objective 1: Optimisation of a MDG for sample introduction of metallic NPs in suspension

The significant advantage of this sample introduction system is a 100 % transport efficiency, so that errors for calibration and determination of the transport efficiency will not affect the size determinations of NPs, as it is the case for conventional pneumatic nebuliser. Calibration by use of liquid standards will be investigated and validated.

Objective 2: Combination of a MDG with a pneumatic nebuliser

A main limitation of the MDG is its extremely low flow rate of pl min^{-1}, which is not suited to analyse, for example environmental water samples. Therefore, a MDG used for calibration will be combined with a conventional pneumatic nebuliser for the sample introduction of complex samples at high flow rates. This novel sample introduction configuration, which will be defined as dual system here, will be optimised in order to obtain high signal sensitivity as well as high reproducibility. The applicability of this arrangement and the figures of merit

will be demonstrated and reported for the analysis of Ag and Au NPs. Furthermore, the NP number concentrations, at different sizes, will be determined.

Objective 3: Application of the dual sample introduction system for analysis of oxidic metal NPs

The next objective of the project is related to the application of the dual sample introduction system in the analysis of the oxidic metallic NPs, following different separation methods to reduce the dissolved ion content in the NP sample. The presence of a high concentration of ions interferes with analysis of smaller NPs. This makes especially the analysis of complex NPs samples such as ZnO and alumina (Al_2O_3), extensively used in consumer products, challenging.

Objective 4: Investigation of matrix effects using the combined sample introduction system

The dual sample introduction opens a new possibility in the study of matrix effects in the plasma and in the analysis of their impact on the characterisation of NPs, because it allows to separate matrix effects caused by a nebuliser from those taking place in the plasma. For this purpose, droplets of ionic metal standards are generated and mixed with aerosols generated by a pneumatic nebuliser with changing matrix composition. The main objective here is to show that the new dual nebuliser technique used for the size calibration of the NPs is reliable even in the presence of other solvents than H_2O. The first part of the matrix effect study aims at investigating the effect of nitric (HNO_3) and hydrochloric acid (HCl) on the size characterisation of silica coated Au NPs (SiO_2-Au). The effect of the varying acid concentrations on the NPs entering via the pneumatic nebuliser was simultaneously compared to the acid effect on the droplets from the MDG going into the plasma. The second part of the matrix effect study aims at the investigation of elements of different physical property on NPs size characterisation. Elements were chosen based on their differing elemental mass,

ionisation energy and heat of vaporisation and melting point to look at their effect on the droplets from the MDG in the plasma and consequently to what extent the size characterisation of the corresponding NPs is affected.

Objective 5: Application of the dual sample introduction system for the analysis of environmental surface waters

Finally, the dual configuration will be applied to analyse engineered and/or naturally occurring NPs in different environmental surface water samples. Water from four different sources in Switzerland will be investigated time resolved for the presence of metallic NPs. For this purpose an ICP-TOF-MS will be combined with the dual sample introduction system for a quantitative and qualitative analysis of metals in a particulate form.

3 Experimental

3.1 Chemicals

3.1.1 Experiments on spICP-MS and dual sample introduction system nebuliser

Standard solutions of dissolved In, Ag, (Certipur, stock solution 1000 mg L^{-1}, Merck, Germany) and Au (Specpure, stock solution 1000 mg L^{-1}, Alfa Aesar, US) were prepared in 1 % HNO_3 (65 % weight by weight (*w/w*) ultrapure grade, Merck, Darmstadt,Germany) and Au in 1 % HCl (30 %, Merck, Darmstadt,Germany) respectively in Milli-Q water (MilliPore gradient, Merck MilliPore, Darmstadt, Germany) to make up to 100 µg L^{-1}.

Monodispersed NPs of Ag (20 ± 2.9 nm, 32.7 ± 4.8 nm, 40 ± 2.9 nm, 60.8 ± 6.6 nm, 79.8 ± 5.4 nm and 103 ± 11 nm) each with an average mass concentration of 0.02 mg mL^{-1} (nanoComposix, San Diego, CA, USA) and reference material of Au NPs (NIST, Gaithersburg, USA) at nominal value of 30 nm (RM 8012) and 60 nm (RM 8013) citrate stabilised were used. Suspensions of 100, 80 and 60 nm NPs were prepared at 100 µg L^{-1}, of 40 nm NPs at 20 µg L^{-1}, of 30 and 20 nm NPs at 10 µg L^{-1} when analysed using the MDG and diluted by a factor of 1000 when introduced through the pneumatic nebuliser (PN). The NPs samples were sonicated for 10 min and suspended in Milli-Q water to prepare the required concentrations. Fresh dilution of the stock material in Milli-Q water was performed daily after sonication of the sample for 10 min to ensure solution homogeneity and to reduce NPs´ aggregation.

Digestions of Ag and Au NPs were carried out following the procedure outlined by Fabricius *et al.*[132] Briefly, Ag NPs were digested in HNO_3 (1.4 mL of 65 % purity) and Au NPs in a mixture of HNO_3 (1.1 mL) and HCL (0.3 mL of 30 % purity). Internal standards used for total content determination of the dissolved metal were iridium and indium (both Certipur, stock solution 1000 mg L^{-1}, Merck, Germany) for Au and Ag, respectively.

3.1.2 Analysis of metal oxides nanoparticles

Standard solutions of Zn and Al (both from Merck, Germany) were prepared in 1% HNO_3 in Milli-Q water, used for calibration purposes through the MDG. Commercially available NPs of ZnO < 130 nm (in 40% ethanol; Sigma –Aldrich), 50 nm and 70 nm (50 % in H_2O, product no 45588 and 45006, respectively; Alfa Aesar) and Al_2O_3 powder (< 50 nm; Sigma-Aldrich) were used as stock material. The exact size distribution of the NPs is unknown.

For ZnO NPs two different methods were tested to prepare the sample. Amberlite MB-150 Mixed Bed, Exchanger (Sigma Aldrich) was used to perform cation exchange chromatography. A 10x diluted (in 40 % EtOH) ZnO NPs sample was eluted through the column. EtOH was used to dilute the sample since the ZnO NPs were stored in EtOH because the equilibrium of the NPs and the Zn^{2+} is less affected than when using a different solvent.

Another method to remove the dissolved ions was by centrifugation. The sample was first diluted followed by centrifugation at 9000 rpm and the NPs residue that settled at the bottom of the vial was collected for the same process of dilution and centrifugation to be repeated for 4 cycles where the residues were equally divided and resuspended in 2 different solvents: one part in 40 % EtOH and second part in H_2O. The final residue was resuspended in 40 % EtOH and diluted 10^3 - 10^6 times in 2 - 3 % EtOH and in H_2O. The same washing and centrifugation steps with only H_2O were done for Al_2O_3 NPs to reduce the number of Al^{3+} ions. The NPs were all introduced as aerosol through the PN in the instrument.

3.1.3 Matrix effect studies

3.1.3.1 Acid effects

A standard solution of Au (Certipure, 1000 mg/L stock solution, Merck, Germany) was prepared in 1 % HCl (from 30 % sub boiled; Sigma Aldrich Chemie, Switzerland) and 1 % HNO_3 (Merck AG, Darmstadt, Germany) in Milli-Q water (18 MΩ cm, Millipore, Billerica, USA) to make 250 Au μg L^{-1} each, introduced through the MDG. A standard suspension of

citrate-stabilised silica-coated SiO_2-Au NPs (5 ppm stock solution, nanoComposix, San Diego, CA), was diluted to 0.2 µg L^{-1} in 0, 1, 2, 5 and 10 % of each HCl and HNO3 (sub boiled, Trace select, Sigma Aldrich, Chemie, Switzerland). These SiO_2-AuNPs have a nominal diameter of 100 nm; the Au inner core has an average diameter of 72 ± 5 nm and a shell thickness of 17 ± 1 nm and were aspirated via a PN in the ICP-MS.

3.1.3.2 Elemental matrix effect studies

A standard solution of 200 ug L^{-1} Ag was prepared from 1000 mg L^{-1} stock and introduced as droplets in the ICP-TOF-MS. Isotopically enriched ^{109}Ag (9.53 mg L^{-1} Ag, 98.3 % ^{109}Ag) was purchased from Merck (Darmstadt, Germany) and will be further referred to as ^{109}Ag. Monodispersed NPs of 80 nm Ag (79.8 ± 5.4 nm) with an average mass concentration of 0.02 mg mL^{-1} (nanoComposix, San Diego, CA) were used. Matrix elemental solutions of lead (Pb), lanthanum (La), magnesium (Mg), lithium (Li), lutetium (Lu), caesium (Cs), rubidium (Rb), uranium (U), and cerium (Ce) (1000 mg L^{-1} , Merck AG, Darmstadt, Germany and Inorganic Ventures, Christiansburg, Virginia, USA), listed in the order they were used, were made with concentrations of 0, 0.001, 0.025, 0.1, 0.25, 0.5, 1, 10, and 100 (omitted for U) mg L^{-1}. Dilutions, carried out gravimetrically were done in 2 % HNO_3 (Merck AG, Darmstadt, Germany) solution. NPs were diluted in Milli-Q water (ultra-high purity (UHP) water (Millipore, Billerica, Massachusetts, USA) and sonicated for 5 min both prior to dilution to break up NP agglomerates and ensure uniform suspension. The Ag NPs, ^{109}Ag, and matrix elements (0-10/100 mg L^{-1}) were all introduced via the PN Figure 13).

3.1.4 Experiments on application of microdroplet generator pneumatic nebuliser inductively coupled time of flight mass spectrometry in environmental water samples

A stock solution of Au (Certipure, 1000 mg/L stock solution, Merck, Germany) and a multi-elemental stock solution consisting of 23 elements; Ag, Al, B, Ba, Bi, Ca, Cd, Co, Cr, Cu, Fe, Ga, In, K, Li, Mg, Mn, Na, Ni, Pb, Sr, Tl, Zn (Certipur, 1000 mg/L Merck AG Darmstadt,

Germany) were mixed in 1 % HCl/HNO_3 to make 250 µg L^{-1} of Au in each sample containing 0, 25, 125, 250 and 500 ug L^{-1} of the multi-elements. SiO_2-Au NPs samples of 72.4 ± 5.1 nm (NanoComposix) was diluted to 0.25 ug L^{-1} in Milli-Q water. The multielemental solution was introduced through the MDG for calibration purposes.

Samples which were aspirated into the ICP-TOF-MS via a PN, were collected in May 2016 from four different water bodies: the effluent from the chemistry building at the Eidgenössische Technische Hochschule (Swiss Federal Institute of Technology, ETH) Zürich, Lake Zürich, River Limmat and Rhine River in Basel. The samples were first filtered through 0.45 µm filter (Chromafil®, Macherel-Nagel, Germany) before being analysed. The chemistry building effluent water sample was diluted two times prior to analysis. The ICP-TOF-MS data were acquired for 5 min for the Rhine River sample, as compared to 3 mins for the Lake Zürich, River Limmat and effluent water from the chemistry building.

3.2 Microdroplet generator

A microdroplet generating system commercially available from Microdrop Technologies GmbH (MD-K-150, Norderstedt, Germany) was used on top of a vertical falling tube allowing for generated droplets to be transported efficiently into an ICP-MS. The operation of the MDG has been described in detail in Chapter 1 (1.6.4) and in previous publications.[114, 129, 131] In this study a dispenser head with a nozzle size of 50 µm was used either in single pulse mode to produce droplets of 68 - 74 µm or in the triple pulse mode to produce droplets of 33 - 36 µm at a frequency between 10 - 25 Hz. The droplet formation and size was monitored through a CCD camera. Through a gas flow inlet, Helium (He) was used as a carrier gas to dry and guide the droplets so that their size was small enough to travel to the plasma,[130] ensuring no loss of analyte through the falling tube and therefore enabling a reproducible analysis. At the bottom of the vertical falling tube an inverted T-piece adapter was connected to the outlet of a spray chamber and to the ICP torch. A Meinhard type pneumatic nebuliser

operated with Ar gas was used in conjunction to a conical spray chamber with impact bead. The Ar gas travels through the adapter and thus transported the falling MDG generated droplets into the plasma. The set up used in this project is illustrated in Figure 12.

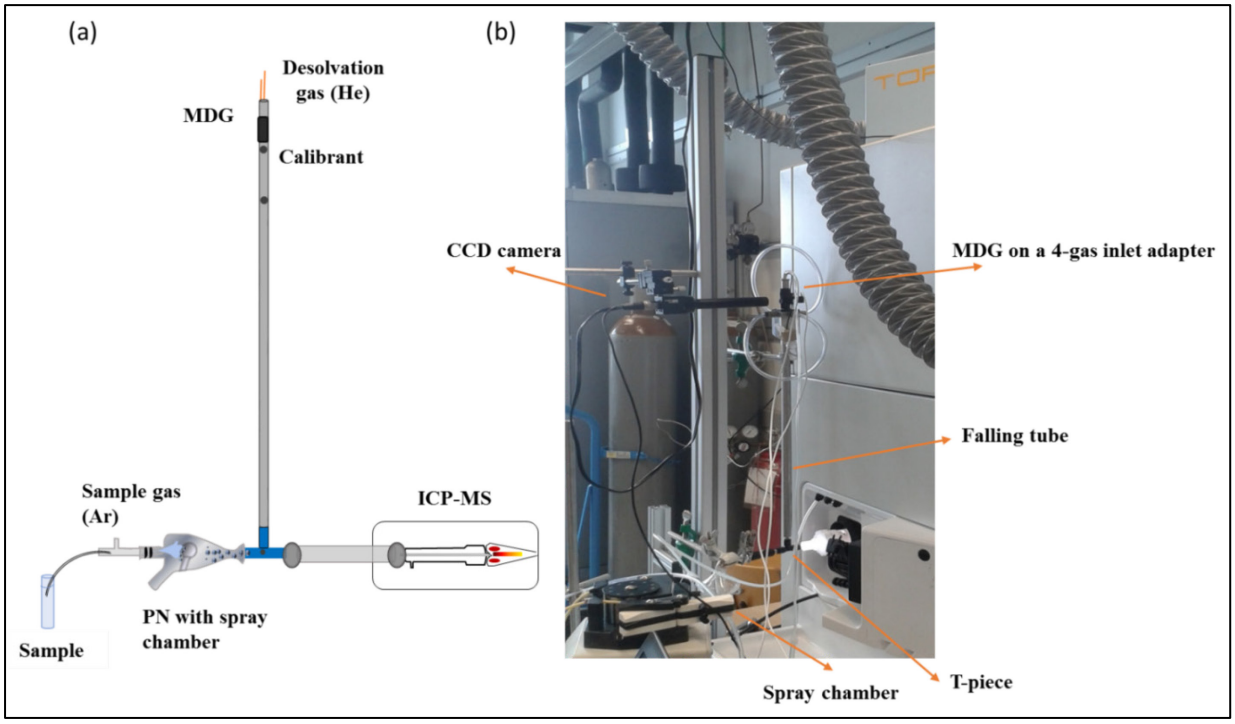

Figure 12: (a) Setup of MDG connected to an ICP-MS via a falling tube and a T-piece as used in this project. The MDG sits on a vertical tube where the droplets together with He travel down. The droplets merge with the sample entering horizontally through a spray chamber and together travel to the ICP-MS. (b) Picture showing the camera mounted on a parallel post to capture the droplets generated.

3.3 Inductively coupled plasma mass spectrometry

The experimental parameters for each of the ICP instrument used in this work are listed in the tables below. The instrumental parameters were tuned to obtain maximum sensitivity and stability when both the MDG and the PN were in use.

3.3.1 Inductively coupled plasma quadrupole mass spectrometry

When coupled to the quadrupole instrument, X-Series II (Thermo Fisher Scientific (Bremen, Germany) standard operating conditions were used on the ICP-MS for the droplet analysis (Table 1). The only notable difference was the lower Ar gas flow of 0.5 - 0.6 L min^{-1} which was mixed with a He flow of about 0.5 - 0.6 L min^{-1} coming from the MDG. Dwell times of 5

and 10 ms were used for individual droplet detection. In some cases for signal optimisation and stability monitoring, longer dwell time of 500 ms was also used. When the MDG was connected, while the latter was dispensing this solution deionised water was being aspirated via the PN at a flow rate of 0.42 mL min^{-1}. Sample was only analysed via the PN when the MDG was turned OFF.

Table 1: Operating conditions for XSeries II when used in sp-mode.

Instrumental parameter	Value
Instrument	Thermo Xseries II
RF power (W)	1400 - 1500
Ar flow $Lmin^{-1}$	0.5 - 0.7
He Flow $Lmin^{-1}$	0.5 - 0.6
Sample uptake	Self aspirating
Dwell time (ms)	5 or 10 or 500
Isotopes monitored	^{115}In, ^{197}Au

3.3.2 Sector field inductively coupled plasma mass spectrometry

The sector field instrument used in this work was an Element XR from Thermo Fisher Scientific (Bremen, Germany). The Element XR was used in the analysis of NPs through the development of the combination of MDG and spICP-MS and in the application of the combined method for the analysis of metal oxides NPs. Operating conditions for the instrument are listed in Table 2.

However, the instrument is not able to perform continuous signal detection, even when monitoring single isotopes. Therefore, a settling time of at least 3 - 4 ms after each single scan is required. During the settling time the instrument is not detecting and, therefore, the NPs arriving at the detector at this time are not measured. The importance of this blind time interval is noticeable due to the low dwell time (10 ms) and the high number of scans required for single particle mode analysis. Moreover, the settling time has a non-constant

contribution to the total scan duration and is therefore not predictable. This problem has been solved by applying a correction factor (f_{sett}), which is calculated by dividing the total analysis time (sum of dwell times and settling times) by the sampling time (sum of all dwell times). Either the number of detected NPs or the sum of signal intensities was statistically corrected for by applying the factor f_{sett}. The value of f_{sett} was in the range of 1.25 to 1.43 depending on the ICP-MS method used.

Table 2: Operating conditions of the SF ICP-MS.

Instrumental parameter	Value
Mass resolution (m/Δm)	400 (Low resolution)
Scanning mode	Fast scan mode (E-scan)
Mass window (%)	10
Samples per peak	1000 (100 for 10 % mass window)
Detector	SEM in pulse counting mode
Integration time (ms)	0.1 (per sample/peak)
Dwell time (ms)	10 (100 samples/peak)
Integration type	Average/ Integration
Integration window (%)	1 / 10
Isotopes monitored	^{107}Ag, ^{197}Au, Zn^{66}, Al^{27}
RF power (W)	1200 - 1300
Sample gas - Ar flow rate (L min^{-1})	0.78 - 0.82

Desolvation gas - He flow rate (L min^{-1})	0.30 - 0.40
Sampling depth (mm)	-3.5
Sample uptake rate (mL min^{-1})	0.20 - 0.22

3.3.3 Inductively coupled plasma time of flight mass spectrometry

A commercially available ICP-TOF-MS, *icp*TOF® (TOFWERK AG, Thun, Switzerland) was used in the characterisation of NPs in the presence of various matrices. In the standard operating mode, ions of 14 - 254 m/z values are simultaneously detected by the TOFMS to ensure maximum instrument resolution and sensitivity. The illustration of an experimental procedure is given in Figure 13 and the operating conditions used for the ICP-TOF-MS in the sp-mode are given in Table 3.

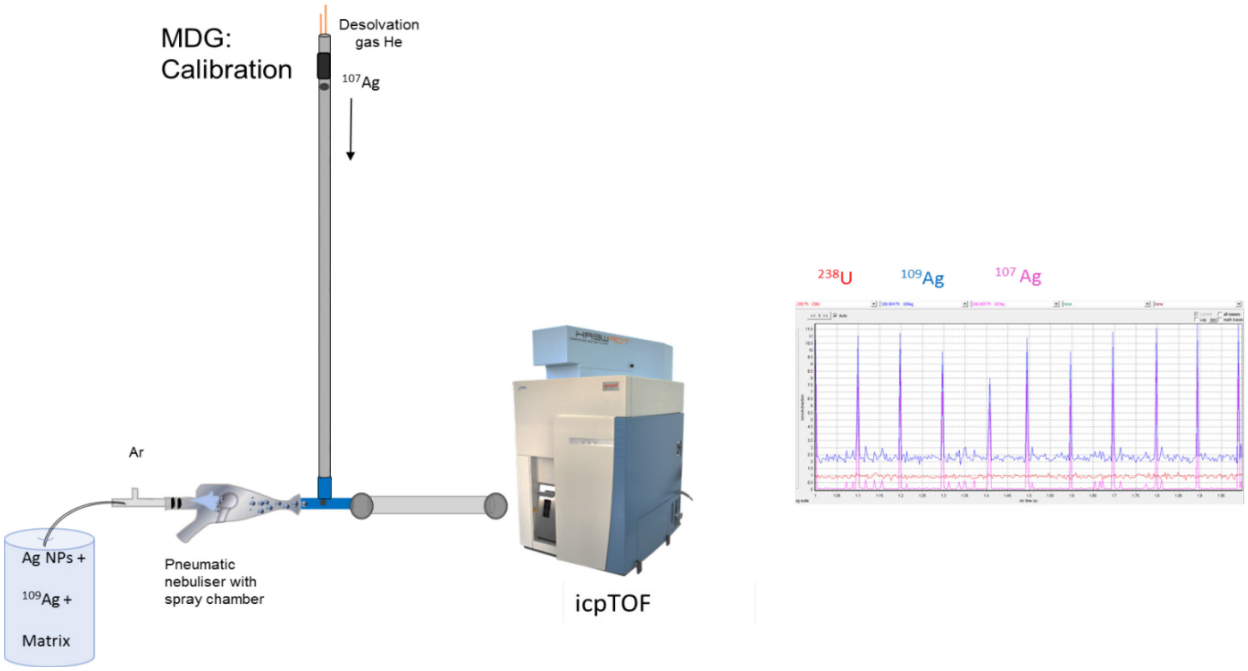

Figure 13: Illustration of an experimental procedure when an ICP-TOF-MS was used: ^{107}Ag was introduced as droplets from the MDG, Ag NPs, ^{109}Ag and matrices were aspirated by a nebuliser into the ICP-MS. Signals from these three Ag analytes were simultaneously measured by ICP-TOF-MS shown in the chromatogram. The regular spikes show the signal from the droplets. The droplets signal shows presence of multiple elements. Smaller irregular spikes correspond to NPs and the constant signal is from a dissolved analyte.

In the routine experiments, notch filters are applied attenuate ions from the plasma and matrices as shown in Table 3. During the analysis of matrix effects from elements, due to the high concentration of matrices introduced in the plasma, notch filters for the different experiments carried out starting in the absence of matrices were applied to reduce the number of ions measured and prevent detector saturation due to its high concentration.

Table 3: Standard operating conditions for ICP-TOF-MS with MDG

Instrumental parameter	Value
Isotopes monitored m/z	14 – 275
Masses Notched	$^{16}O^+$, $^{14}N_2^+$, $^{16}O_2^+$, $^{40}Ar^+$
Injector diameter (mm)	1.5
Time resolution	30 us or 10 ms
TOF repetition rate kHz	33
Cooling gas flow ($Lmin^{-1}$)	14.0
Auxiliary gas flow ($Lmin^{-1}$)	0.75
RF power (W)	1500
Sample gas - Ar flow rate ($L\ min^{-1}$)	0.8 - 1.16
Desolvation gas - He flow rate ($L\ min^{-1}$)	0.5 - 0.8
Sampling depth (mm)	3.0
Sample uptake rate ($mL\ min^{-1}$)	0.7
Data acquisition	High resolution/ Trigger mode

The data were extracted from the ICP-TOF-MS data acquisition and viewer software, TofDaq. The extracted data were processed in LabVIEW to find single-particle (i.e. NP) signals from several isotopes of interest. Steps for single-particle finding:

1. All mass spectra were mass calibrated. Mass spectra were qualitatively analysed to determine the elements of interest in each of the water samples.
2. The data files, .hf5, were loaded in LabVIEW and the peak data for a selected subset of isotopes was selected.
3. Peak data from this data subset were summed together to create a signal transient that can be used to identify NP events from any of the isotope signals summed together. A threshold was manually set to discriminate between single-particle and dissolved signals. This manually set threshold was used with the LabVIEW "peak finder.vi" algorithm in order to find all peaks above the threshold.
4. The indices of all found peaks were collected and data at each index in the array, as well as one data point before and after each index, were selected and deleted from the peakdata in order to generate peakdata matrices that only contain the background isotopic signals for each isotope of interest.
5. The mean and standard deviation of the background dataset of each isotope of interest was determined. A value equal to the mean + 5*standard deviation was calculated for each isotope to serve as the cut-off for single-particle selection for each isotope.
6. The LabVIEW peak finding algorithm was then applied with the threshold specific to the 5-sigma value of the background of each isotope. In this way, the single-particle signals from many isotopes can be extracted from the TOFMS data, even with different background levels for the diverse NP types. The indices of each found peak were used determine the peak area of all NP signals.
7. The peak areas of NP signals were determined as the sum of three adjacent data points because a NP signal can be split between two spectral acquisition windows and

because it is unknown whether the NP signal is split between the main detection window and the preceding one or the following one (Figure 14).

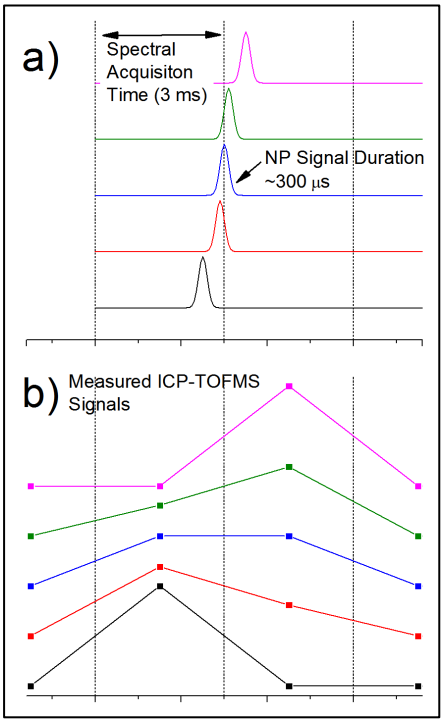

Figure 14: A NP signal can be split between two adjacent signal-acquisition windows (a). This will affect the measured peak shape and requires two or three data points to be summed to obtain the true NP signal (b).

3.4 Transmission electron microscopy

Transmission electron microscopy (TEM) images of the nanoparticles were obtained with a Philips CM200 TEM on carbon-coated copper grids at 200 kV acceleration voltage.

3.5 Data evaluation

For data evaluation all raw data, including calibration curves, spike intensity and mass fraction histograms, particle sizes and number concentrations, were transferred from the instrument software to Origin software version 9 (OriginLab Corporations, Northampton, USA) for further processing.

4 Results and Discussion

4.1 Single particle mode inductively coupled plasma mass spectrometer on gold nanoparticles

SpICP-MS is a technique commonly used to determine the metal mass content of each metal-containing NP and the concentration of NPs in the sample analysed. At the time the project started, spICP-MS was a relatively new method to analyse NPs. Not only did it require minimal sample preparation, NPs were also analysed in large quantities and the ease at which different NPs could be analysed consecutively was a major advantage in comparison to the various imaging techniques available for NPs analysis. The purpose of these experiments was to test the spICP-MS and use the established equations for analysing Au NPs.

A sample of Au NPs (60 nm, NIST) was measured using a quadrupole ICP-MS (X-Series II). The instrument was used in conventional operating conditions with the exception of a low dwell time of 10 ms as used in typical spICP-MS studies.[38, 94, 133] To measure and calculate values of the parameters for equations 1.4 - 1.7 (chapter 1.5.2) dissolved Au solution (4 ng mL^{-1}), standard reference material (60 nm Au NPs, NIST) and a sample of Au NPs, were analysed. The chromatograms corresponding to the signal from the dissolved Au and Au NPs are shown in Figure 15. The number of peaks shown in the chromatogram of the NP sample corresponds to the number of NPs detected, q_p. The sample uptake flow rate, q_s is determined by the difference in sample uptake and waste.

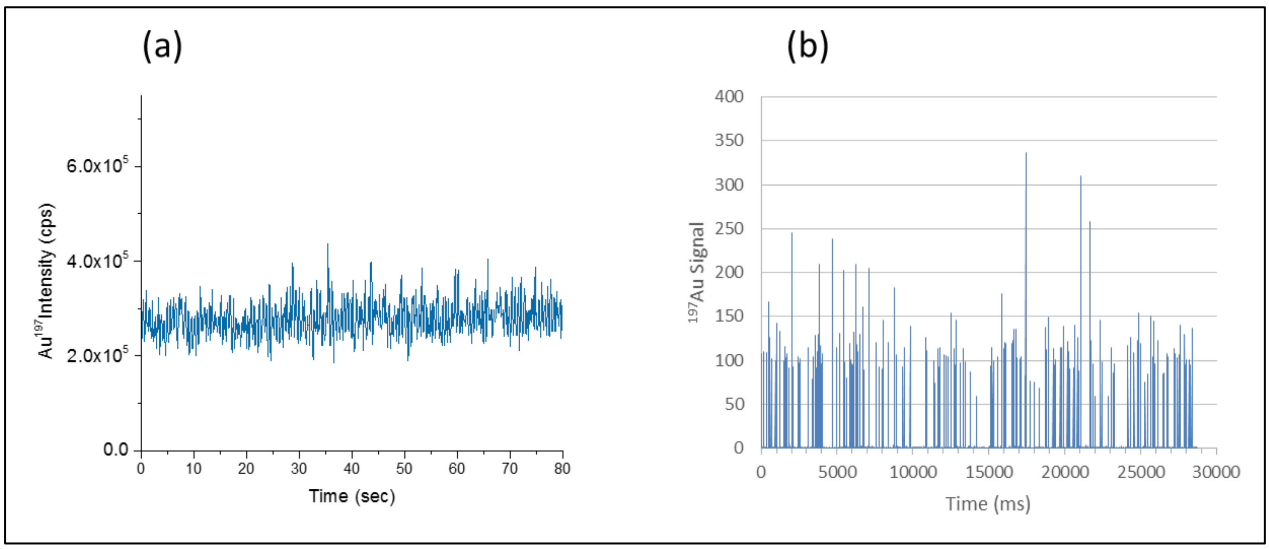

Figure 15: Time trace for 4 ng mL^{-1} Au solution (a). Time trace for Au NPs (cps/5 ms) at a concentration of 100 µg L^{-1} (b). Both measured in the spICP-MS mode at 5 ms. The signal intensities for a and b and the number of spikes in b were used to calculate the transport efficiency. The characterisation of a sample of NPs of unknown size and concentration was then possible.

Signal from the NP was considered to be greater or equal to mean of background + 5 SD. Assuming that all the particles that reached the plasma are detected, the transport efficiency can be calculated following the particle frequency (number concentration) method,[97] following equation 1.4, where the 60 nm Au NPs sample was used as the reference material.

The peak height from each Au NP signal corresponds to the number of ions present in the NP $n_{,i,p}$ and the signal from the dissolved Au solution corresponds to the ion flux per second, c_a. Consequently, following equation 1.5, the number of ions in 1 NP (unknown sample) signal was determined and eventually the mass of Au analyte in that NP calculated. The sample concentration was calculated following equation 1.6 and the concentration of the stock was back calculated after taking the dilution factor into consideration. The mean diameter of the NPs in a sample was calculated following equation 1.7, assuming the density of the NPs is equivalent to the density of its metal analyte. The diameters of each NP was used to generate a size distribution of the unknown sample. Figure 17 shows the determined size distribution of a sample of Au NPs, with a mean size of 52.6 ± 7 nm. The signals at 11 - 13 nm

correspond to the background which has not been subtracted from the raw data. The concentration was calculated to be 4.71 particles mL^{-1}.

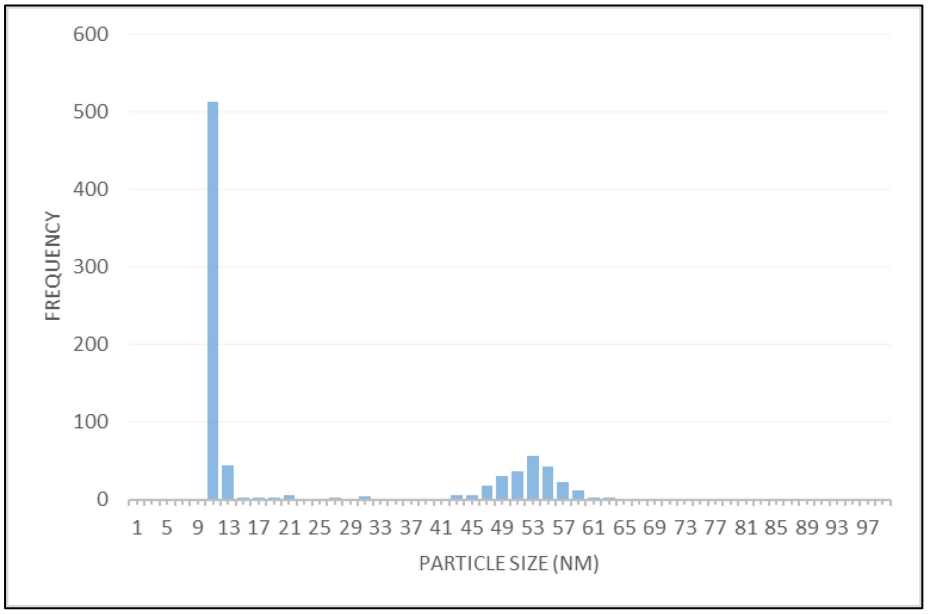

Figure 16: The determined size distribution in nm of a sample of Au NPs by spICP-MS. The histogram shows the presence of 2 sets of maxima, with the size distribution at 10 nm corresponding to the background signal. The mean diameter of the NPs was 52.6 ± 7 nm and the concentration was 4.71 particles mL^{-1}.

These initial experiments confirm that the spICP-MS and the established equations allow the characterisation of Au NPs in terms of diameter and concentration if an Au standard NP reference is used. The accuracy of the method will be addressed in more detail in later experiments (chapter 4.2).

With Au NPs as a reference material, spICP-MS can be applied in the characterisation of different metal-containing NPs as well. The main limitations of spICP-MS are that the quantification capabilities is limited to reference materials and the approximate calculation of mass transport, which in turn affect the calculation of the transport efficiency. Other problems related to the measurement parameters including dwell time and number of isotopes have also been addressed[30,98,102] and were discussed in the introduction (chapter 1). The dwell time attainable by most instruments results in lowering the noise due to the integration time of the background signal with respect to the particle signal. Furthermore, partial signal or

signals from multiple NPs simultaneously from a single droplet cannot be excluded, which makes it difficult to quantify the size of the NP.

4.2 Coupling of microdroplet generator to an inductively coupled mass spectrometer

The purpose of these experiments was to couple the MDG, to an X-Series II ICP-MS, and acquire data for the analysis of solutions containing dissolved metals (In) and/or Au NPs.

The MDG and adaptor that were used have been described by Shigeta *et al.*[114] As it had not been coupled to the X-Series before at BAM a special glass ball-joint connector was required. This was made and added to the coupling adapter. The connector allowed for the direct connection of the MDG to the back of the ICP-MS torch. In this setup the horizontal distance travelled by the droplets before entering the plasma, i.e. distance travelled once they entered the Ar stream, was approximately 28 - 29 cm.

As can be seen in Figure 17, for the analysis of the 100 μg L^{-1} In solution using the MDG-ICP-MS system stable operating conditions were achieved that allowed for minimum droplet jittering, 100 % transport efficiency and good sensitivity. More specifically, after measuring the droplets generated at a frequency of 10 Hz for In solution (100 μg L^{-1}) for 3 min, i.e. total of 1800 droplets, the following analytical figures of merit were calculated: mean 124.9 counts, SD 13.1 and 10.5 % RSD. The signal intensities distribution for the droplets is shown in Figure 18.

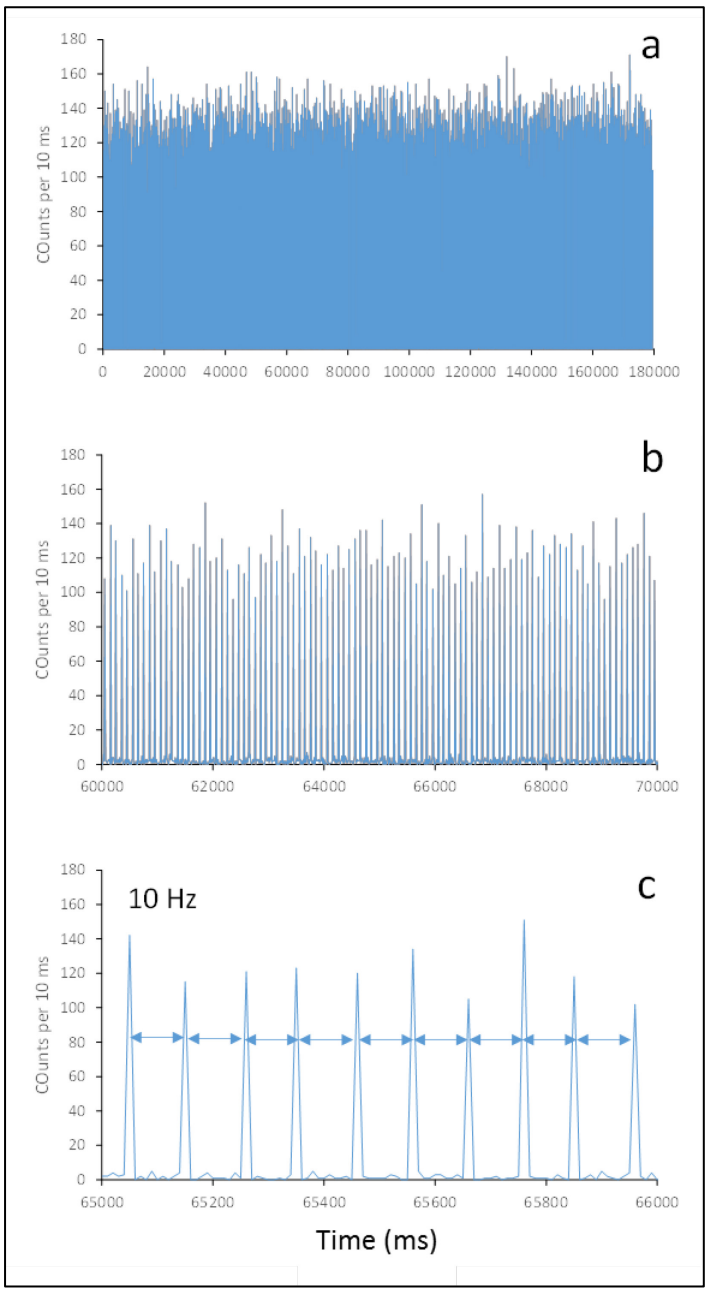

Figure 17: Signal intensities measured for an In solution of 100 µg L^{-1}; droplets were generated using the MDG-ICP-MS at a frequency of 10 Hz: 3 mins acquisition (a), 10 sec acquisition (b), and 1 sec acquisition (c). The signals from the droplets show that all the droplets generated were detected.

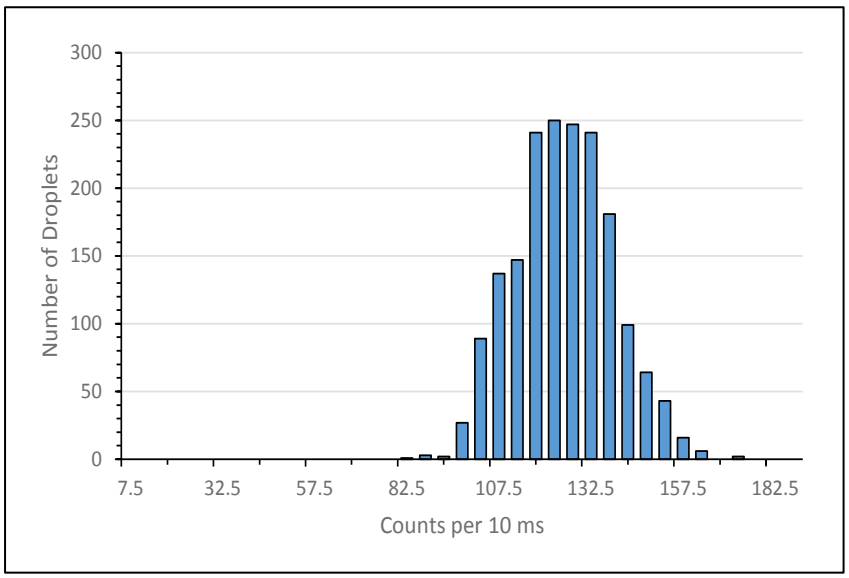

Figure 18: Histogram of recorded In signal intensities (100 µg L^{-1} In solution) for 1800 droplets, which shows that the droplets' generation was uniform.

In a separate experiment using the much longer dwell time of 500 ms the relatively stable signal of the In droplets was investigated at various MDG droplet generating frequencies (Figure 19). However, 200 Hz seemed to be the upper limit as severe instability was observed at 300 Hz.

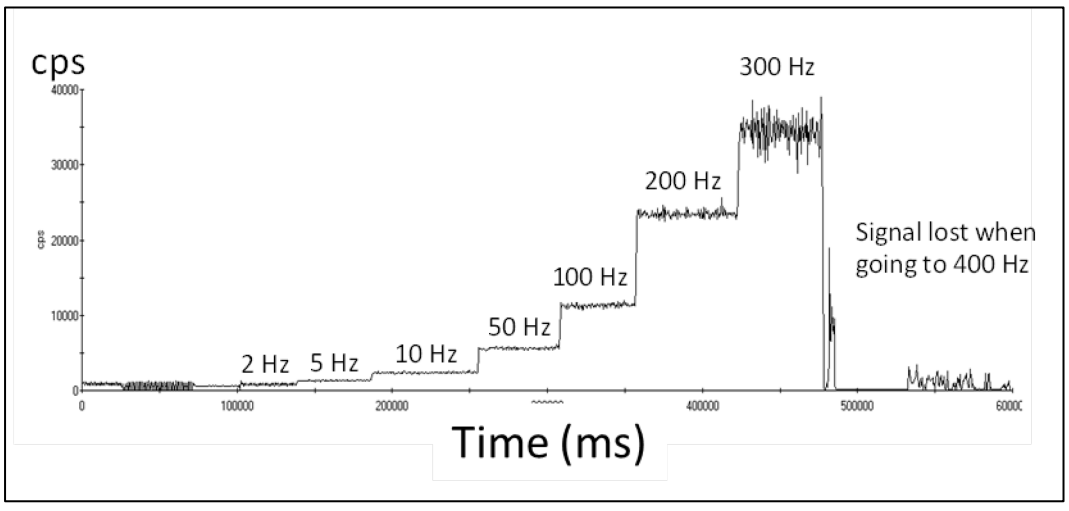

Figure 19: Signal intensity of In droplets acquired at 500 ms dwell times as a function of MDG frequency. Each step in the time trace represents the signal of the droplets generated at different frequency. From 5-10 Hz, the droplets were stable. Going upwards from 10 Hz, the stability of the droplets decreases and the signal intensity increases, which means more than 1 droplet was detected at a time.

In an attempt to switch to NP analysis, a dilute suspension of 5 ng L^{-1} of 60 nm Au suspension was introduced through the MDG. Given that this was a freshly prepared sample

and no Au NPs had been lost then it could be calculated that approximately 30 Au NPs were introduced. However, as can be seen in Figure 20, < 10 Au NPs were detected. This indicates that there is a substantial loss in the number of NPs. Upon trying to analyse more concentrated solutions, the generation of droplets of a 25 ng L^{-1} and 50 ng L^{-1} Au 60 nm NPs solution with the MDG was not efficient, i.e. droplets were not formed of uniform size and velocity. Moreover, the MDG nozzle seemed to become blocked more frequently. Even if the generation of the droplet-containing NPs would have been regular, the throughput from the MDG is quite low. The analysis of NPs with MDG would take a lot longer than with sp-mode.

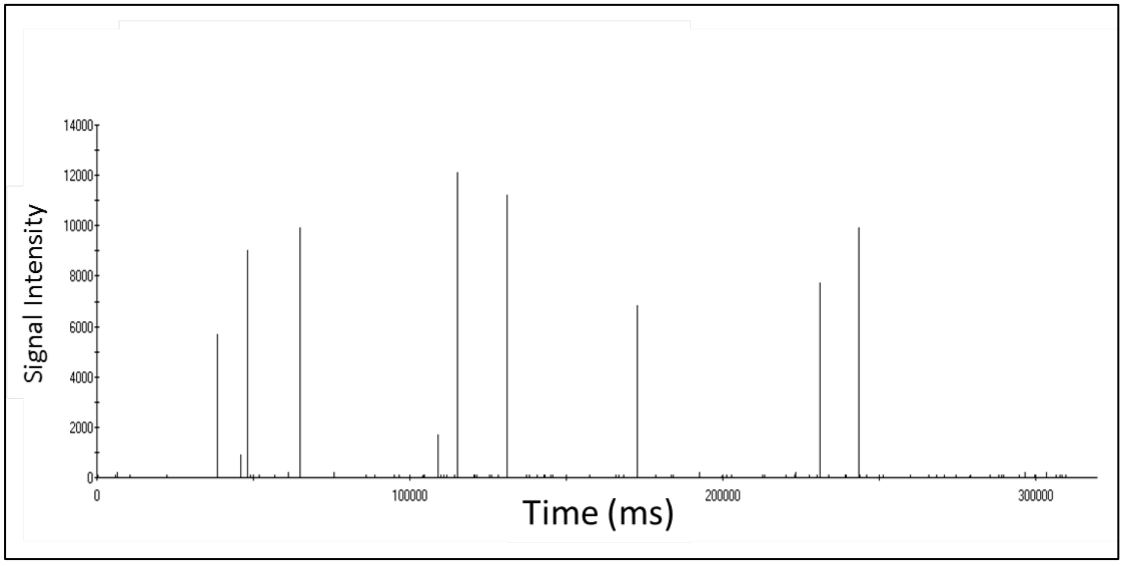

Figure 20: Signals corresponding to Au NPs introduced via the MDG into the ICP-MS in the sp-mode at a dwell time of 10 ms. The number of NPs that was detected did not correspond to the number of NPs introduced in the ICP-MS. The total amount of NPs introduced should have produced 30 signals.

The above experiments show that a MDG can be used in converting standard solutions of an analyte into droplets of known size and concentration. Providing a 100 % transport efficiency, high sensitivity and flexibility in the droplet size produced, a calibration can be performed by using a standard solution through a MDG. However, experiments on Au NPs reveal that the introduction of NPs by a MDG is insufficient. This can be overcome by

coupling a sample introduction device suitable for introducing NPs which is a pneumatic nebuliser. The next chapter will focus on a dual sample introduction system.

4.3 Investigation of a combined microdroplet generator and pneumatic nebulisation system for rapid quantitative determination of metal-containing nanoparticles using inductively coupled plasma mass spectrometry[134]

A hybrid approach combining both a MDG and PN was established and studied in detail. The MDG served to introduce well defined droplets of known dissolved metal concentration for response factor calculation. The NP-containing aqueous sample was introduced via the pneumatic nebuliser spray chamber system. Based on this approach, the metal mass fraction and thus size of the intact NPs can be readily determined. This novel sample introduction configuration was optimised in terms of the ICP-MS parameters in order to obtain high signal sensitivity as well as high reproducibility. The applicability of this arrangement and the figures of merit are demonstrated and reported for the analysis of Ag and Au NPs. Furthermore, the NP number concentrations, at different concentration levels, were also determined.

4.3.1 Investigation of possible interference of the two sample introduction systems

In a first step it was investigated whether an efficient operation without interaction/interference between a MDG and a PN during their operation is possible. The MDG was used to deliver a known concentration of dissolved metal and the PN was used to deliver a known Au NP solution.

The MDG allowed the determination of the nebulisation efficiency of the PN. This was conducted by running the same concentration of dissolved metal using both the MDG and the PN. The standard solution of the dissolved Au (for that two concentrations were tested 5 and 25 $\mu g\ L^{-1}$, with 25 $\mu g\ L^{-1}$ being used for the calculations) was delivered via the MDG. While the MDG was dispensing this solution, deionised water was being aspirated via the PN at a flow rate of 0.42 ml min^{-1}.

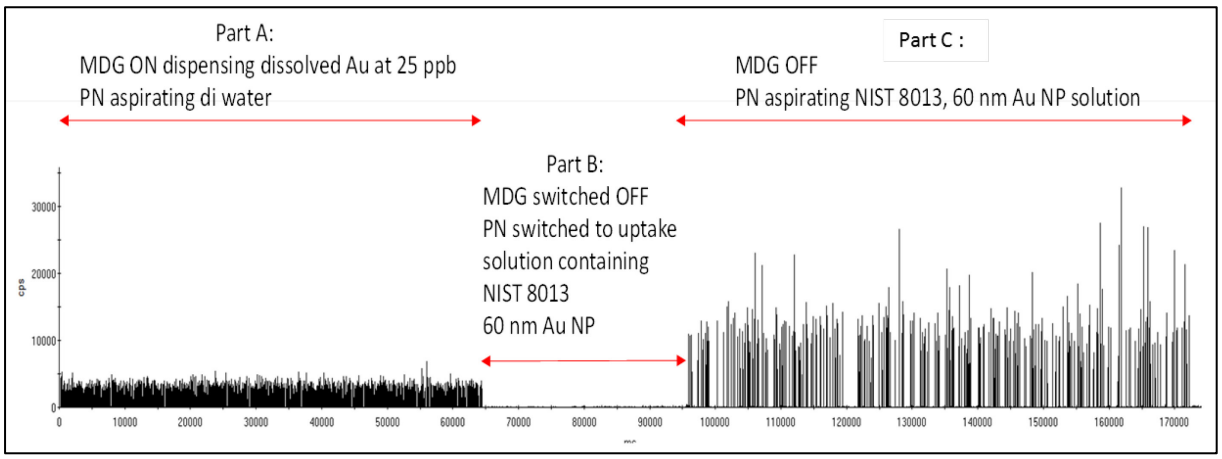

Figure 21: MDG with PN ICP-MS in operation. Part A shows the pulses obtained from the introduction of 25 µg L^{-1} dissolved Au via the MDG. Part B is when the MDG is turned OFF and the di water being aspirated by the PN is switched for the NIST 8013 Au 60 nm solution. Part C corresponds to the aspiration of the NIST RM via the PN in the SP mode (10 ms dwell times were used for all experiments).

Since the droplet and NPs are both of the same element, using an ICP-MS with single analyte detection capability, distinguishing between a droplet and NP is not feasible. Therefore, a NP sample was only analysed via the PN when the MDG was turned OFF as shown in Figure 21. The first part of the experiment consisted of generating Au-containing droplets while Milli-Q water is aspirated by the PN. The MDG is then turned off (Part B) and the sample of NPs is aspirated by the PN (Part C). Therefore, operating a MDG and a PN to an ICP-MS within one measurement cycle is possible.

4.3.2 Optimisation of inductively coupled plasma mass spectrometry parameters for the dual microdroplet pneumatic nebuliser inlet system

The ICP-MS parameters used for the developed dual MDG and PN system were optimised and compared to those required when the MDG was used alone. For this purpose, a solution containing dissolved Ag at 100 µg L^{-1} was supplied to the MDG dispenser head and introduced into the plasma as discrete droplets at a given frequency. Optimisation was conducted for maximum sensitivity and signal stability.

A comparison of the optimal operating conditions using the two configurations has been made (Table 4) when tuning the instrument for maximum sensitivity. The system using the

MDG alone operates under dry plasma conditions, which explains the low RF power values. On the other hand, the addition of an aerosol using a conventional pneumatic nebuliser requires increased RF power. Typical values between 1200 and 1300 W were found appropriate for aspiration of deionised H_2O at approx. 0.20 mL min^{-1}. The optimal RF power and Ar flow rate are affected by the liquid uptake rate. The Ar flow rate has a different effect on each system configuration. Higher Ar flow rates are thus required for the dual system configuration, whereas no significant differences were observed for the z-position of the torch (sampling depth) and the He flow rate used to push and dry the droplet through the vertical falling tube. The optimal He flow rate was around 0.350 L min^{-1} for both systems although variations ± 0.050 L min^{-1} did not affect the intensity of the signal significantly.

Table 4: Differences in experimental parameters used for ICP-MS detection of dissolved Ag using the dual inlet system (MDG and PN) and the MDG alone.

	MDG + PN	MDG
RF power (W)	1200 - 1300	800 - 850
Ar flow rate (L min^{-1})	0.78 - 0.82	0.72 - 0.78
He flow rate (L min^{-1})	300 - 400	300 - 400
Torch z-position (mm)	-3.5	-3.5

The stability of the signals is also comparable for both systems and optimised experimental parameters led to reproducible signals for both systems. Although the approach using the MDG alone provided better relative standard deviation values (ca. 4.3 %), the combination with the pneumatic nebuliser gave droplet intensities with RSD values close to 6 % (Figure 22a, c). Therefore, the new dual configuration maintains the good signal stability shown by the MDG alone and in both cases the intensity distribution of the measured droplet are fitted to a Gaussian curve (Figure 22b, d).

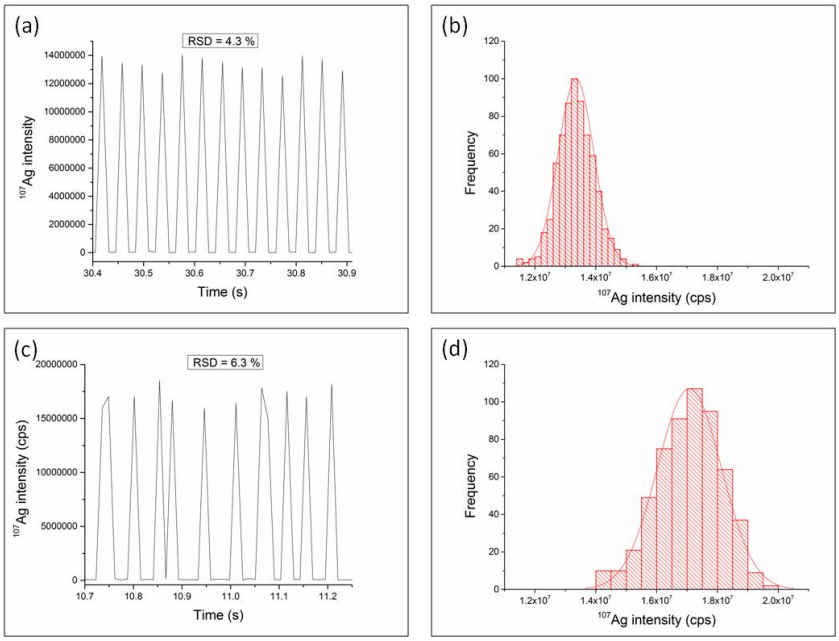

Figure 22: Measurement of Ag elemental solution (100 µg L^{-1}) using a MDG in two different configurations, alone (a and b) or orthogonally coupled with a PN aspirating H_2O (c and d). ^{107}Ag intensity of the generated droplets over an interval of time and histogram of the recorded ion signal intensities is shown.

In spite of the mentioned stability of the signal, the reproducibility in the arrival time of the MDG generated droplets was affected by the addition of the pneumatic nebuliser to the system. The signals acquired from the MDG generated droplets, without the operation of the PN, are shown in Figure 22a. As can be observed the detected signals corresponding to individual droplets were evenly distributed throughout the analysis, in accordance to the frequency of the MDG (25 Hz), i.e. nearly no jitter between the droplets was observed. The addition of water via nebuliser produces a significant alteration of arrival of the droplets in the plasma and the shape of the transient signals (Figure 22c). Variations in the time between droplets or even detection of droplets separated by temporal intervals lower than the frequency of generation were observed in some cases.

Regarding the data points acquired per droplet, additional differences were observed between the two configurations. The dual system showed a response in 6 - 9 consecutive data points. That means droplets were detected during 0.6 - 0.9 ms according to the experimental sample time (0.1 ms). On the other hand, the system with only the MDG showed droplet durations mainly of 3 - 4 samples per peak (0.3 - 0.4 ms, Figure 23). Therefore, an increase in the

duration of the droplet signal was observed for the dual system, i.e. in the presence of aqueous droplets in the plasma.

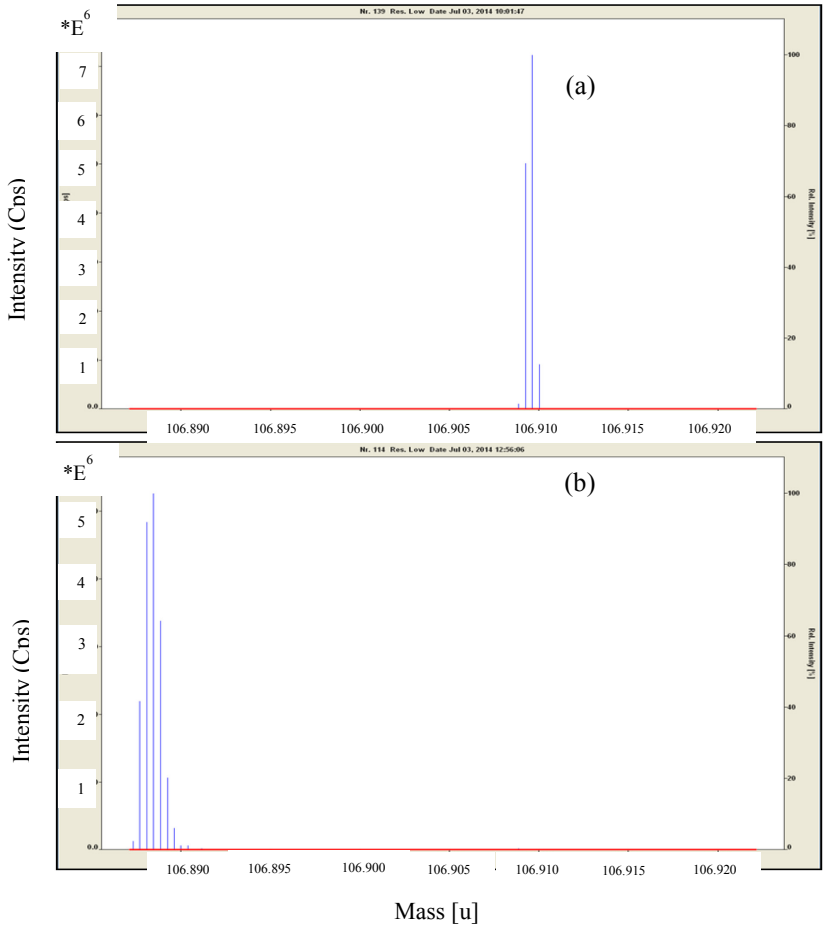

Figure 23: Comparison of the number of data points per droplet in the measurement of Ag elemental solution (100 µg L^{-1}) using a MDG in two different configurations, on its own, where the signal intensity is higher with less data points (a) or orthogonally coupled with a PN aspirating H_2O, where the signal intensity is lower but extends to more data points (b).

Comparing Figure 22b and d, higher intensity (20 - 30 %) and wider signal distributions were obtained with the MDG system when combined to the PN. A signal intensity increase as the result of H_2O addition has been already reported by Günther *et al.*[135] and O´Connor *et al.*[136] The more likely hypothesis is the so called aerosol penetration depths, which explains the signal increase due to the complete vaporisation of the sample closer to the sample cone and therefore, less material losses due to reduced out-of-axis diffusion. Flamigni *et al.*[137] also showed such effects and pointed out the importance of controlled addition of small amounts of H_2O. In the presented dual inlet system, relatively large amounts of H_2O are aspirated by

the PN. Thus, higher humidity in the plasma carries the droplets deeper into the plasma and a slow vaporisation is probably involved in the increased signal dispersion.

4.3.3 Dual inlet signal calibration

The system combining a MDG and a conventional PN allows multiple strategies for the measurement of elements either in solution or as NPs. Sample introduction through the MDG or the PN is possible. Due to the discrete sample introduction via MDG and the required time consuming manual sample exchange procedure, the required washout time, and solvent compatibility issues, this entrance was used for calibration of the signal. Therefore, in this work, the quick and reproducible size measurements of NPs were conducted using the MDG for signal calibration.

Firstly, the response equivalence of both inlets was demonstrated using the dual configuration. Both sample introduction inlets were tested while the other inlet was working under optimised conditions. Therefore, diluted samples of Ag NPs were measured in single particle mode from the PN and the MDG. The intensities obtained for single NPs introduced from both entrances were comparable (Figure 24). These results confirmed the equivalence of both signals in intensity and distribution, and enabled the quantification of the NPs using the MDG for calibration.

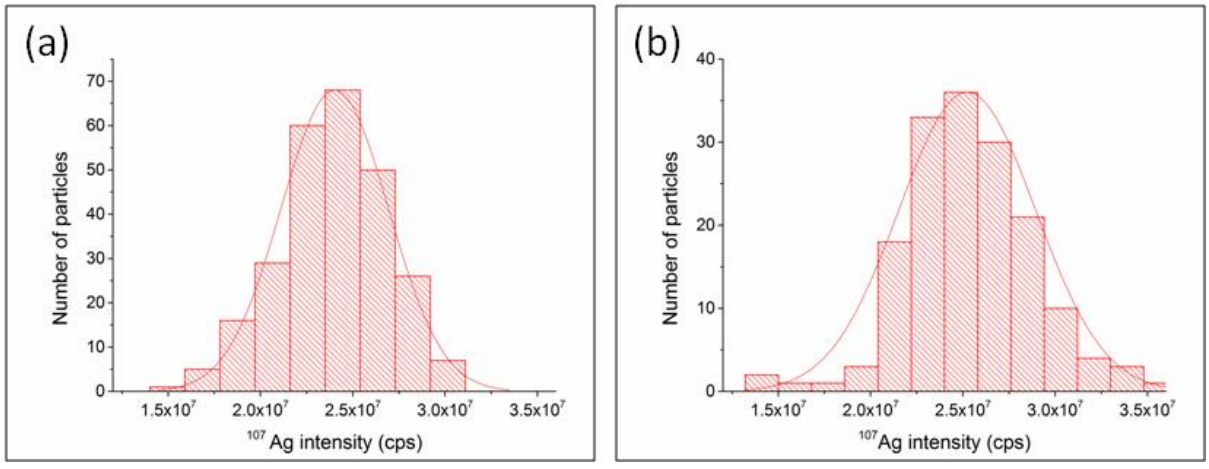

Figure 24: Measurement of 80 nm Ag NPs using the dual configuration (MDG & PN) while introducing the sample through a) the PN (200 ng L^{-1}), at flow rate of ca. 20 µL min^{-1} and b) the MDG (100 µg L^{-1}) at a flow rate of ca. 22.5 nL min^{-1}. This difference in flow rate is reflected on the y-axes of the histograms, with the

NPs introduced through the PN at a higher concentration (a) than the NPs introduced through the MDG (b). However, the signal intensities from the NPs are comparable.

Furthermore, calibration of the signal using dissolved Ag solutions and Ag NPs both introduced via MDG was performed. The results of these calibrations show a good linear response with the concentration of the solution and with the Ag content in the NPs (Figure 25). The introduction of NPs into the ICP-MS through the MDG was successful in these set of experiments, which is not always the case (as shown in chapter 4.2).

The difference in the vaporisation process for NPs and dissolved metal solutions has already been described by Borovinskaya *et al.*[105] where they reported that the signal duration for dissolved salts is significantly lower than for alloy NPs, where they observed earlier vaporisation and higher diffusion for the NPs. However, the authors also pointed out the feasibility of a calibration with standard solutions for the mass quantification of Au NPs and Ag NPs using a MDG coupled independently to the ICP-MS. In the dual-inlet system presented here, the calibration signal from the MDG may be used for the quantification and size determination of metal NPs introduced through the PN. The following experiments address the accuracy of this approach in determining size and number of NPs.

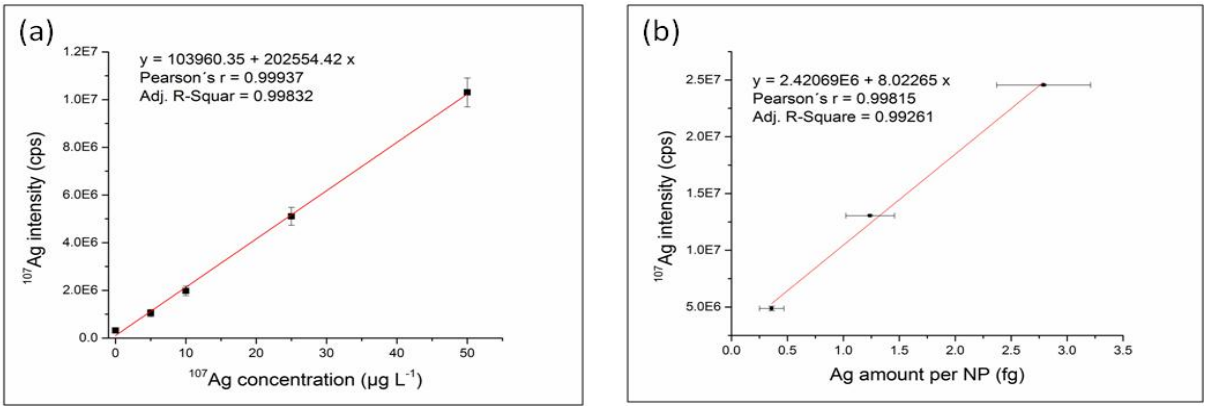

Figure 25: Calibration curves for (a) dissolved Ag and (b) Ag NPs, both introduced through MDG. Y-error bars (a) correspond to the standard deviation in the detected ^{107}Ag counts per second from three replicates, n = 3; x-error bars (b) correspond to the uncertainties in the Ag content reported by the manufacturer of the NP material.

4.3.4 Particle size determination

As discussed previously, the analysis of NPs by spICP-MS involves some calculations and more importantly requires the use of well-characterised NP reference materials in order to determine the nebuliser efficiency. Assuming that every NP that reaches the plasma is detected, the nebulisation efficiency (ε_n, dimensionless) can be calculated using NP solutions of known concentration:

$$\frac{q_p}{c_p} = q_s \times \varepsilon_n \qquad (1.4)$$

where q_P = flux of particles detected in plasma (s^{-1}), c_p = concentration of NPs containing the detected metal (mL^{-1}), q_S = sample uptake rate (mL s^{-1}) (Note: parameter abbreviations taken from Heithmar & Pergantis[97]). The mass of the analyte element in a single NP ($m_{a,p}$), and therefore the theoretical diameter of spherical NP, can be calculated following equation. 1.5:

$$m_{a,p} = [q_s \, \varepsilon_n \, c_a / q_{i,a}] \, n_{i,p} = k \, n_{i,p} \qquad (1.5)$$

where $n_{i,p}$ = number of ions of analyte elements detected in a single NP pulse, c_a = the analyte concentration in a dissolved standard (g mL^{-1}), and $q_{i,a}$ = ion flux measured for the dissolved standard (s^{-1}). To calculate k (response factor), an ICP-MS standard of the dissolved element is used and same sensitivity than for NP form is assumed.

The MDG allows the analysis of discrete sample volumes and offers transport efficiencies close to 100 % ($\varepsilon_n \approx 1$). For this reason the MDG was used for signal calibration measuring known concentration standard solution of dissolved analyte and calculating the response factor k as follows,

$$k = v_d \, \varepsilon_n \, c_a / n_{id,a} \qquad (1.8)$$

where v_d = volume of the droplet (mL), and $n_{id,a}$ = number of ions of analyte elements detected in a single droplet. Subsequently, $m_{a,p}$ can be calculated following equation 1.5 measuring the $n_{i,p}$ in an unknown NP sample either through the MDG or by the pneumatic nebuliser. This is possible due to the equivalence of the NP signal introduced from the MDG

or the pneumatic nebuliser, as it has been demonstrated and discussed previously (Figure 24). Therefore, an interesting application of this dual inlet configuration is the fast determination of the size of engineered NPs without the necessity of using NP reference materials as it has been reported using a normal pneumatic nebuliser set-up for spICP-MS.

In this study, the new configuration was tested using a dissolved Ag solution introduced through the MDG for single-point calibration (calculation of the response factor k). Then, NPs from the same element, i.e AgNPs, were introduced through the PN. Since the mass of Ag is known for the MDG generated individual droplets (by measuring the droplet size and knowing the concentration of the dissolved Ag solution), the corresponding Ag mass in a single NP can be calculated based on equation 1.5 and 1.8. Using the density of solid Ag and the mass of Ag in a single nanoparticle ($m_{a,p}$), the diameter of a spherical Ag NP can be calculated (equation 1.9).

$$d_p = (6\, m_{a,p} / \pi\, \rho_p)^{1/3} \qquad (1.9)$$

where ρ_p = density of the metal at room temperature (g nm^{-3}).

Ag NPs of 20, 30, 40, 60, 80 and 100 nm were used to test the new approach and the results are summarized in Table 5. 20 nm Ag NPs were the smallest that were detected, although 30 nm Ag NP was the smallest that could be quantified. The dispersion of material was not taken into consideration to calculate the size of the NPs. The calculated sizes were however found to be in good agreement with the values provided by the manufacturer. Moreover the experiments were reproducible on a day to day basis. In Figure 26 we show the intensity distribution of 30 nm Au NPs, which fit in a Gaussian distribution. Some higher intensity counts in the histogram indicate double particle detection during the analysis.

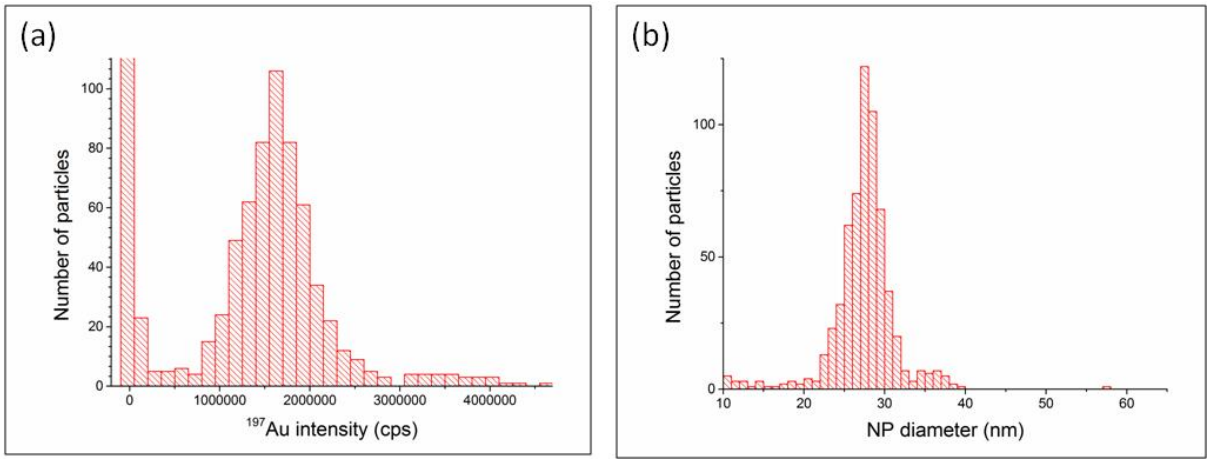

Figure 26: Histogram showing a) intensity counts and b) diameter distribution of 30 nm Au NPs using the dual system. The Au NPs were introduced through the nebuliser.

Au NPs certified reference materials were also analysed using the described dual system obtaining size values within the uncertainties given by the manufacturer (Table 5).

The simultaneous use of the MDG and the pneumatic nebuliser for particle size determination is straightforward, more flexible and routinely applicable when compared to the standalone use of spICP-MS or MDG. Importantly, it is not necessary for particle size determination to know the transport efficiency and therefore, no standard NP reference material is required. Compared to the sole usage of the MDG, the addition of the PN gives the flexibility to instantaneously change between different samples without having to change the sample in the MDG.

Table 5: Size determination of NPs using a dual inlet system (MDG & PN). Measured NPs: Au NPs (30 and 60 nm), Ag NPs (30, 40, 60, 80 and 100 nm). Uncertainties correspond to the standard deviation in the calculation of the NP diameter from three replicates, n = 3.

Certified size	**Measured size**	**Theoretical NP mass**	**Experimental NP mass**
(nm)	**(nm)**	**(fg)**	**(fg)**
		Ag NPs	
		(Standard material)	
32.7 ± 4.8	29.7 ± 0.1	0.19	0.140 ± 0.0016

40.6 ± 3.0	42.0 ± 1.5	0.37	0.410 ± 0.0438
60.8 ± 6.6	60.4 ± 1.0	1.23	1.21 ± 0.0521
79.8 ± 5.4	80.0 ± 1.4	2.79	2.81 ± 0.1666
103 ± 11	93.3 ± 0.7	6.00	4.46 ± 0.1014
	Au NPs		
	(Certified Reference Material)		
27.6 ± 2.1	28.7 ± 0.2	0.21	0.24 ± 0.0050
56.0 ± 0.5	57.7 ± 0.1	1.77	1.94 ± 0.0096

4.3.5 Transport efficiency determination

In contrast to NP size determination, knowledge of the nebuliser transport efficiency is a prerequisite for calculation of NP number concentrations. The calibration of the signal using the MDG in the dual system was used to develop an alternative approach to calculate the nebuliser transport efficiency. Once the NP size is known, using either a certified material or determining the size by MDG signal calibration, the nebulisation efficiency can also be determined. The new method is based on the counts (intensity method) detected in a given time instead of the number of detected NPs (NP counting method) in a given time. That is possible because k (equation 1.8) is already known from the dissolved analyte solution measured through the MDG.

Using the traditional single particle method (NP counting method), after the measurement of the sample uptake rate, the nebulisation efficiency for a standard NP material is determined comparing the number of NPs reaching the detector in a certain time with the expected number of NPs (equation1.4). In the intensity method (equation 2.0), the sum of the intensities of the detected NPs per second ($q_{i,p}$) is considered instead of the number of detected NPs per second (q_p), and it is compared with the expected number of ions. The latter can be obtained from the previously calculated response factor k (equation 1.8) and the concentration of the analyte in the standard NP material.

$$(q_{i,p} / c_{a,p})\, k = q_s\, \varepsilon_n \qquad (2.0)$$

where $q_{i,p}$ = ion flux measured for the analyte in the NPs (s^{-1}), $c_{a,p}$ = analyte concentration in the NP suspension (g mL^{-1}), q_s = sample uptake rate (mL s^{-1}), and ε_n = the nebulisation efficiency (dimensionless).

Therefore, to determine the NP size and the nebulisation efficiency of a sample containing NPs it is not necessary to use a NP reference material since the NP size can be calculated independently from this information and the NP concentration can be obtained from bulk analysis of the material. Once the nebulisation efficiency is known, the analyte concentration determination in the NP samples ($c_{a,p}$) can be calculated using equation 2.0. The signal coming from more than one NP can be considered for nebulisation efficiency calculations using the intensity method. In contrast, counts from two NPs detected simultaneously are difficult to consider applying the NP counting method, mainly when the intensity histograms of single and double NPs overlap. The intensity method is affected by the dissolved metal present in the NP samples. Therefore, background correction must be considered for accurate calculations.

Both methods were compared for the ε_n determination of 80 nm standard Ag NPs. The results of four sample preparations on two different days are shown (Table 6). As can be observed, the reproducibility in the calculation of the ε_n is high with standard deviations of less than 5 %, there the ε_n is around 6.4 %. It should be noted here that the error in ε_n does not include dispersion of nanomaterial. Moreover, both methods led to similar results demonstrating that the new approach as a feasible alternative to the commonly used NP counting method. Once the reproducibility in the calculation of the nebulisation efficiency was assessed, this parameter was measured for different NP sizes (Ag and Au NPs). The agreement between both approaches is demonstrated once more in Table 7. It is interesting, however, that transport efficiencies varied for the different NP sizes measured. According to many

authors,[94, 95, 97, 98] the transport efficiency can be calculated for a known NP material and applied to measurements of other NPs sizes. However, our results indicate that significant errors in the NP determination can occur when common transport efficiency factors are applied to different sized NPs. For unknown NPs the ε_n can be determined by the intensity method after bulk analysis, i.e. after sample digestion. Thus, the digestion of the NP suspension allow us to obtain the concentration of analyte ($c_{a,p}$) and calculate ε_n applying equation 2.0. In this way, neither the size nor the concentration needs to be known in advance for the transport efficiency determination using the dual inlet system.

4.3.6 Validation of the new approach

The dual inlet configuration was used for size and concentration determination of an Au NP reference material (NIST) using the above presented intensity method. For validation two dilutions of the Au NPs reference material (NIST), were defined to be "unknown samples" The concentrations and diameters of these unknown samples were calculated and compared to the data given by the manufacturer.

Table 6: Nebulisation efficiency for 80 nm Ag NPs analysed with the dual inlet configuration. Comparison of two different calculation procedures based on signal intensity and NP counting respectively. Uncertainties correspond to the standard deviation in the calculation of the nebulisation efficiency from four replicates, n = 4.

	80 nm Ag NPs	
Day	ε_n (intensity method)	ε_n (counting method)
1	0.0627 ± 0.0007	0.0620 ± 0.0006
1	0.0622 ± 0.0001	0.0613 ± 0.0004
2	0.0671 ± 0.0013	0.0668 ± 0.0014
2	0.0623 ± 0.0032	0.0648 ± 0.0030
Mean	0.0636	0.0637
St. Dev.	0.0024	0.0025

Table 7: Nebulisation efficiency for Ag and Au NPs of different sizes analysed with the dual inlet configuration. Evaluation of the calculation procedure based on signal intensity (intensity method) by comparison with the conventional single particle mode (NP counting method). Uncertainties correspond to the standard deviation in the calculation of the nebulisation efficiency from 3 replicates, n = 3.

NP size (nm)		ε_n **(intensity method)**	ε_n **(counting method)**
Ag NPs	30	0.0319 ± 0.0013	0.0349 ± 0.0011
	40	0.0301 ± 0.0003	0.0316 ± 0.0003
	60	0.0604 ± 0.0020	0.0622 ± 0.0014
	80	0.0636 ± 0.0024	0.0637 ± 0.0025
	100	0.0412 ± 0.0054	0.0406 ± 0.0017
Au NPs	**30**	0.0198 ± 0.0008	0.0202 ± 0.0008
	60	0.0274 ± 0.0012	0.0275 ± 0.0013

The response factor k was calculated using the reference signal from the MDG (50 µg L^{-1} of dissolved Au). A solution containing 100 ng L^{-1} Au NP was used for nebulisation efficiency (ε_n) calculation either applying the certified concentration of the material or the concentration determined after bulk analysis of the NPs. Finally, two dilutions of the same Au NP material were used as unknown samples. The sum of the signal intensities obtained for each NP sample was used for $c_{a,p}$ and d_p determination. Table 8 shows a good agreement for the expected and the experimental values using both strategies in ε_n calculations. For the concentration values the error in the measurement is in the range of 1 to 8 % depending on the sample dilution, while the error in the calculation of the particle size is lower than 1.3 % for all the samples. Thus, the intensity-based calculations appear as a reliable alternative to the traditional NPs counting methods.

Table 8: Determination of concentration ($c_{a,p}$) and diameter (d_p) of two different concentrations of a Au NPs reference material (NIST) using the dual sample introduction system (PN and MDG) (Figure 27).

	Conventional method	Intensity method	Expected
Concentration of stock solution ($C_{a,p}$)	51.9 ± 0.6 (certified)	52.0 ± 0.1 (bulk)	
Transport efficiency, ε_n	0.0273	0.0272	-
Sample 1			
Diameter d_p (nm)	56.7 ± 0.2		56.0 ± 0.5
Concentration, $C_{a,p}$ (ng L^{-1})	77.19 ± 2.48	77.40 ± 2.49	76.29
Sample 2			
Diameter d_p (nm)	56.6 ± 0.9		56.0 ± 0.5
Concentration, $C_{a,p}$ (ng L^{-1})	54.65 ± 1.76	54.79 ± 1.76	50.56

Figure 27 summarises and compares the workflow for analyzing NPs using only a PN (spICP-MS) to the dual MDG and PN introduction system.

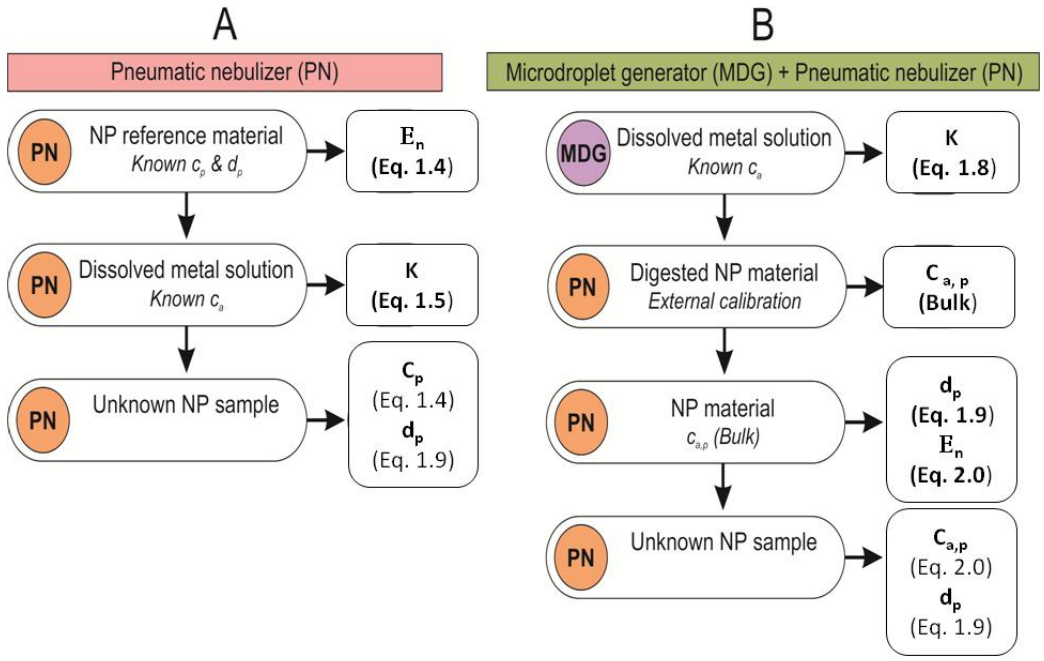

Figure 27: Workflows for NP determination by ICP-MS using two instrumental configurations for sample introduction. A) Single pneumatic nebuliser (PN) and B) dual inlet consisting of the orthogonal connection of a MDG and a PN.

The combination of MDG for signal calibration with a PN for NP measurements allows for the routine determination of NP diameters without the need to use matching reference materials. This approach combines the advantages of the efficiently transported MDG droplets (ca. 100 %) as a reference and is able to introduce large volumes of dilute samples via a pneumatic nebuliser for a representative sampling of the NPs. Moreover, the dual-inlet configuration enhances the standalone MDG signals due to the later vaporisation of the droplet as consequence of the solvent aerosol incorporated from the nebuliser.

Bulk analysis of the unknown Ag and Au NP samples permits the complete characterisation of these NPs in the sample with a dissolved analyte solution as the only reference. In addition, the quantitative transport efficiency of the MDG and the orthogonal coupling of the pneumatic nebuliser are of potential interest for many other studies such as the investigation of matrix effects in the ICP. Therefore, this new configuration offers important advantages for analysis of NPs in real samples, where the lack of reference materials and/or the variable matrices hamper NP characterisation.

4.4 Metal oxides nanoparticle studies using dual configuration

SpICP-MS is a valuable tool not only in the analysis of very low amount of metal based NPs but also in the differentiation between dissolved metal ions and NPs. It has been shown that the combined technique works very well with the well characterised Au and Ag NPs of a range of dimensions (chapter 4.1).[134] Ranville *et al.*[103] have previously reported some difficulties that may arise in the analysis of polydispersed metal oxide NPs. Recently, Hadioui *et al.*[111] showed that by coupling an ion-exchange column (IEC) to an ICP-MS in the single particle mode, the characterisation and quantification of ZnO NPs in river water and waste water effluent was possible. The authors compared quantification techniques between spICP-MS on its own and spICP-MS coupled to ion-exchange resins. The IEC was used for removing dissolved ZnO NPs which otherwise resulted in an overlap between dissolved Zn ions and low mass ZnO NPs.

After investigations on Au and Ag NPs, the dual sample introduction system of a MDG-ICP-MS is applied to characterise ZnO and Al_2O_3 NPs in terms of their size. However, due to the high concentration of dissolved ions, a few clean up techniques had to be tested prior to analysis by spICP-MS.

4.4.1 Analysis of ZnO nanoparticles

What makes spICP-MS important in the analysis of Au and Ag NPs sample, is that the response from the NPs can be differentiated from the ionic signals. However in the case of oxidic NPs, there is a substantial presence of metallic ions which make it extremely challenging to obtain a NP signal and size distribution. One way of getting around it is to reduce the background signal caused by ions and to improve the signal to noise ratio for the NP signal.

Initially, just like for a routine analysis of Ag and Au NPs,[134] ZnO NPs were diluted in H_2O to give a final concentration of 5 ng L^{-1} and analysed in the spICP-MS mode. This high

degree of dilution was done not only to dilute the number of NPs present but most importantly to reduce the background signal due to Zn^{2+}. However as seen in Figure 28, the signal from Zn^{2+} was still very high and overshadowed the signal from the ZnO NPs. This shows that dilution alone is not enough to prepare the sample for spICP-MS and more steps need to be undertaken in order to reduce the background noise due to Zn^{2+}.[134]

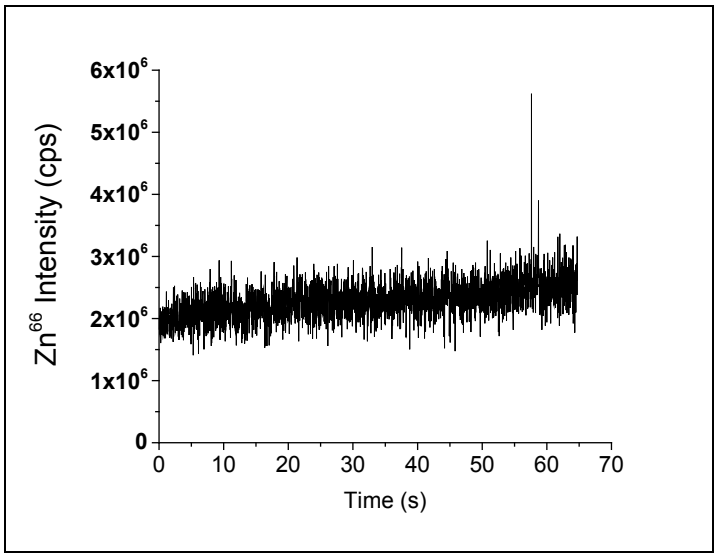

Figure 28: Time resolved signal showing analysis of ZnO NPs by spICP-MS at dwell time of 10 ms. The NPs were prepared in H_2O to give 5 ng L^{-1}. The noise signal is very high which hides presence of any NPs.

4.4.1.1 Ion exchange chromatography

Recently a successful characterisation of ZnO NPs using spICP-MS[110] following ion exchange chromatography (IEC) was reported. This achieved a reduction in the concentration of Zn^{2+} ions and thereafter a size distribution of the ZnO NPs sample could be obtained.

In this present study, for the analysis of a sample of ZnO NPs (< 130 nm), an ion exchanger consisting of a 40 % strongly acidic cation and 60 % strongly basic anion resin was used. By using the stock concentration of ZnO NPs, a slow elution was observed and the outlet of the column obstructed. Therefore the NPs were first diluted in H_20 with a final concentration of 500 ng L^{-1} before being run through the ion exchange column.

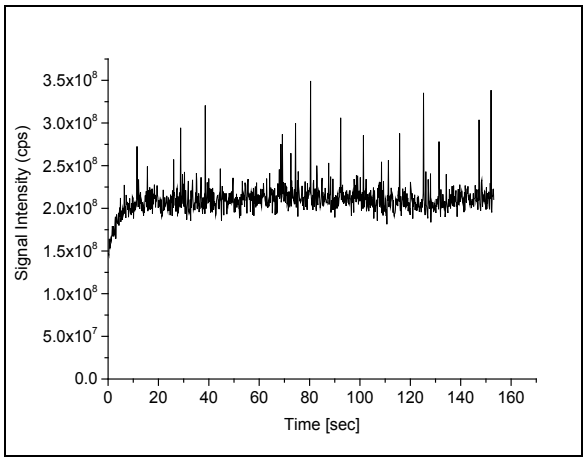

Figure 29: Signal-noise ratio after makeshift IEC. Signal intensity shows high Zn^{2+} background and NPs signals.

After elution from the IEC, the sample was collected and analysed by spICP-MS and the resulting signal intensity is shown in Figure 29. The spikes seen in the chromatogram represent the large NPs and NP aggregates present in the sample. It can also be concluded that this method does not remove Zn^{2+} ions efficiently due to the low signal to noise ratio from the analysis of the eluent. Moreover, from the milky layer on the exchange beads' surface after elution, it was detected that ZnO NPs are being retained on the surface of the beads.

4.4.1.2 Centrifugation

The alternative method for improving the signal noise ratio was to separate NPs from ions by centrifugation. For the samples analysed in H_2O, (Figure 30b and d), the background is at a much lower noise than when IEC was used as a separation technique (Figure 29) and so the signals of particles and/or aggregates are more visible. It is likely that the ZnO NPs were present as aggregate and needed time to stabilise as the re-analysis of the samples after 1 week (Figure 30c and d) shows According to earlier studies on the stability of ZnO particles, at pH < 7.5 the solubility of the particles should increase and between pH 9 and 11 decrease.[138] Both aggregation and stability of the particles depend on a lot of factors including the solvent they are in, the isoelectric point, surface properties and the pH.

Moreover no information is provided about the surface coating of the particles. Since the NPs used consisted of a wide range of sizes, it is not possible to deduce whether the high intensity spikes are due to large particles or aggregates or both.

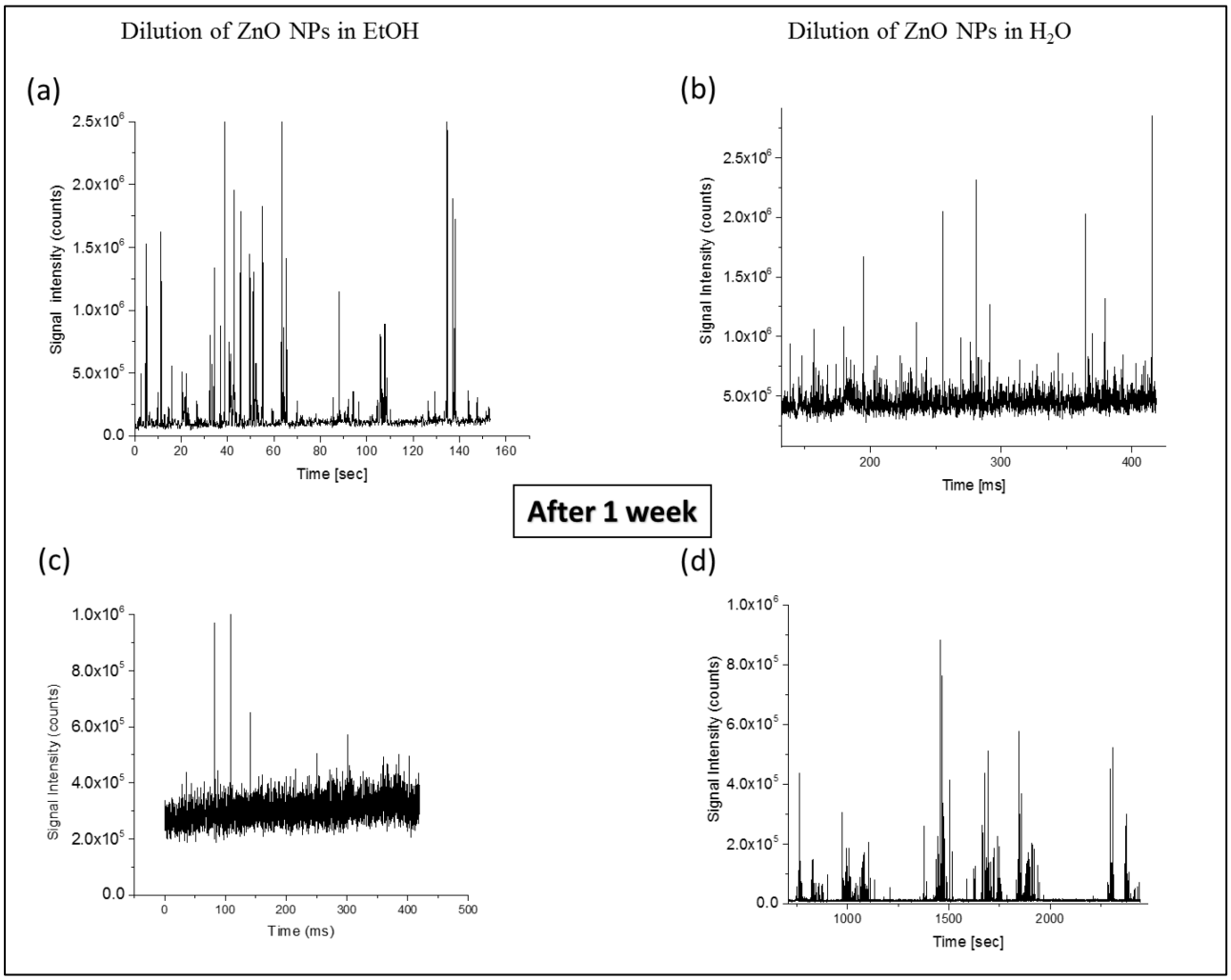

Figure 30: Background and NP signal of resuspended ZnO residue by ICP-MS analysis at a dwell time of 10 ms on ^{66}Zn (a) EtOH and (b) H_2O (dilution of 10^6). The analysis of ZnO NPs after restabilising for 1 week are shown in (c) EtOH and (d) H_2O.

When comparing the dilution of the sample in EtOH and H_2O from Figure 30 (a and b), the background is initially much lower with ZnO NPs in EtOH (Figure 30a) than in H_2O (Figure 30b). The EtOH possibly helped in stabilising the NPs and slowed down the equilibrium process between Zn^{2+} and ZnO NPs. However, after 1 week, it seems that in EtOH the larger NPs and aggregates were dissolved and disaggregated into Zn^{2+} and/or smaller NPs, which in

this case is not visible due to the high background (Figure 30c). In the dilution of the NPs in H_2O, the free Zn^{2+} seems to have aggregated with NPs and bigger particles were formed.

The presence of the high number of ions in the analysis of the ZnO NPs despite the washing steps and the high dissolution of ZnO NPs is a well-known phenomenon. To separate Zn ions from Zn NPs, ultracentrifugation has been employed, whereby it was observed that at low concentration of ZnO NPs the dissolution is higher. This observation was also reported by Hadioui *et al.*[111] and Miao *et al.*[139], where the background due to Zn^{2+} was statistically higher at low concentration of ZnO NPs. However, the dissolution was not as significant in natural water samples. The reason is most likely due to the presence of natural organic matter in the environment which acts as stabilising agent and prevents dissolution, but also causes some agglomeration.[16]

It seems to be that an equilibrium needs to be reached for the ZnO NPs to be stabilised. In the washing steps, the equilibrium of the sample is disturbed whenever fresh milli-Q or EtOH is added to the residue. This probably shifts the equilibrium towards the formation of Zn^{2+} such that the intensity of the Zn^{2+} after the washing step seems to remain constant, and the ZnO NPs are not able to stabilise due to the constant formation of Zn^{2+}.

However, the equilibrium is additionally affected by the tendency of ZnO NPs to aggregate. It has been reported that the size of ZnO NPs increases with increasing mass concentration in the NPs sample and that ZnO NPs are more likely to aggregate due to their surface charge and electrostatic instability.[140] In natural water environments ZnO NPs stabilise due to the presence of colloids which enables the stabilising of NPs.[140, 141] Since the chromatogram obtained from the spICP-MS analysis of ZnO NPs shows that the signal intensity of the NPs is varied, a TEM image was acquired of the ZnO NPs as shown in Figure 31. The TEM images show that the sizes of the NPs were not only varied but the shapes of the NPs were not uniform. Therefore, the analysis of the ZnO NPs used here would not be feasible via MDG-spICP-MS.

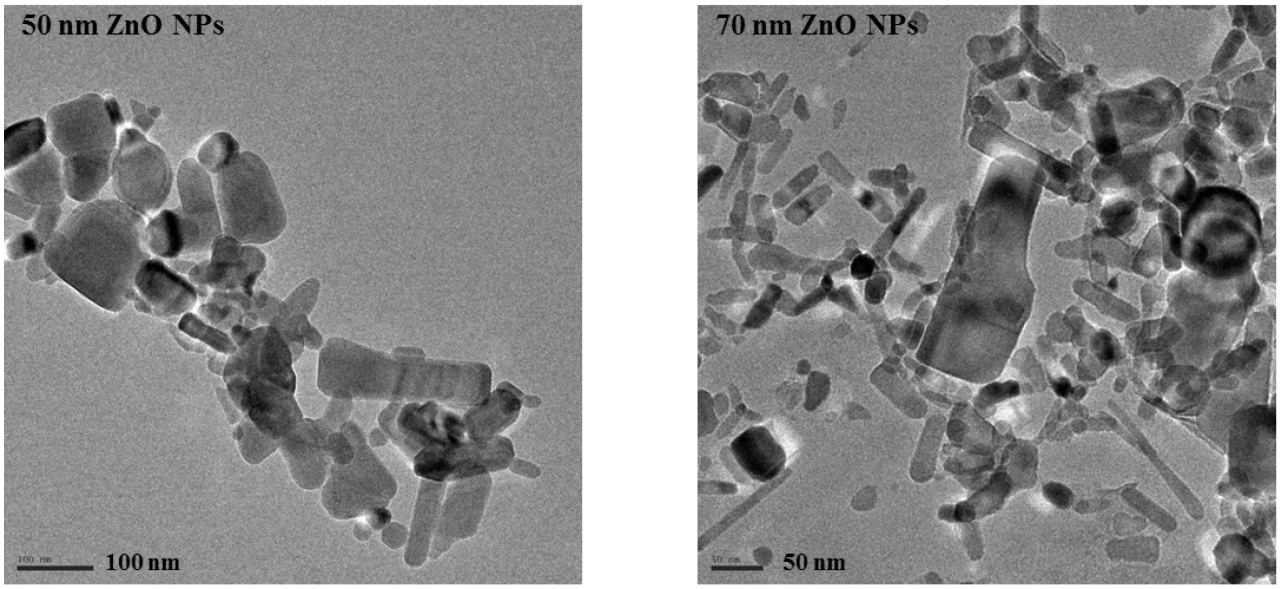

Figure 31: The TEM image of the NPs used in this study: ZnO NPs. 50 nm particles (left), 70 nm particles (right). The sizes are provided by the manufacturer however, the images show the inconsistent size and shape of the NPs.

4.4.2 Analysis of Al_2O_3 nanoparticles

4.4.2.1 Size distribution of Al_2O_3

The washing and centrifugation technique of the ZnO NPs seemed to have worked better than when using an ion exchanger. Therefore the same steps were applied for the analysis of Al_2O_3 NPs. In this work however, the efficiency of each washing step was monitored. The Al_2O_3 NPs were resuspended in H_2O and after each centrifugation step, the residue was saved for the next washing cycle. The supernatant was collected to be analysed by ICP-MS. The resulting Al^{3+} concentrations are shown in Figure 32a. The washing steps seem efficient in reducing Al^{3+} from the NPs sample. After 5 washing steps, there are still some metallic ions causing background signal (Figure 3b) but analysis of NPs can be performed.

In order to obtain an accurate size distribution of the Al_2O_3 NPs, calibration was done using the MDG. A dissolved Al solution at 200 ug L^{-1} was introduced as droplets through the MDG, while Al_2O_3 NPs were introduced via the PN. With the knowledge that the Al_2O_3 particles were all of a regular spherical shape and following the equation for particle size determination (Chapter 4), the size of NPs in the sample could be determined (Figure 32c).

The size distribution has a maximum at 25 nm but extends well beyond the upper size limit given by the manufacturer (< 50 nm).

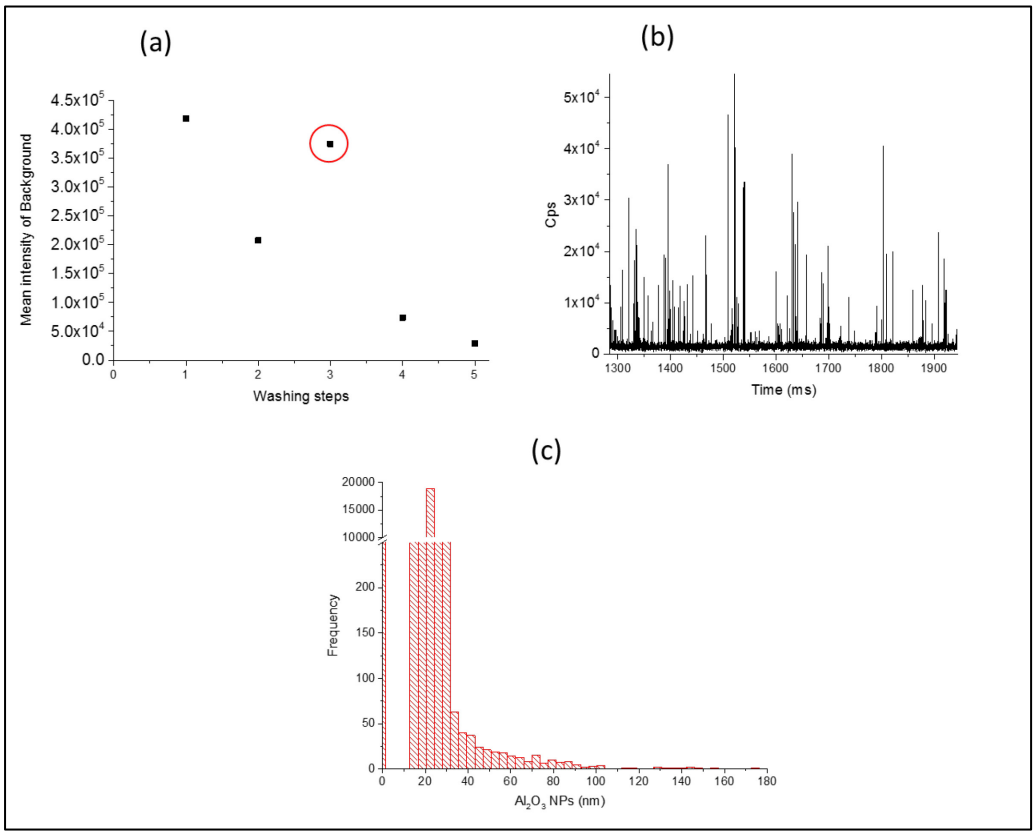

Figure 32: (a) Al^{3+} concentration in supernatant after each washing step 1-5. Washing step 3 is an outlier as the supernatant was collected at 15 mins instead of the 10 mins interval. (b) Signals of residue after final washing step. c) Distribution of particles in terms of size following MDG-spICP-MS.

4.4.2.2 TEM imaging of Al_2O_3 nanoparticles

After the analysis of Al_2O_3 NPs by spICP-MS and a resulting wide range of size distribution, TEM measurements were performed on the samples of Al_2O_3 NPs (< 50 nm according to manufacturer).

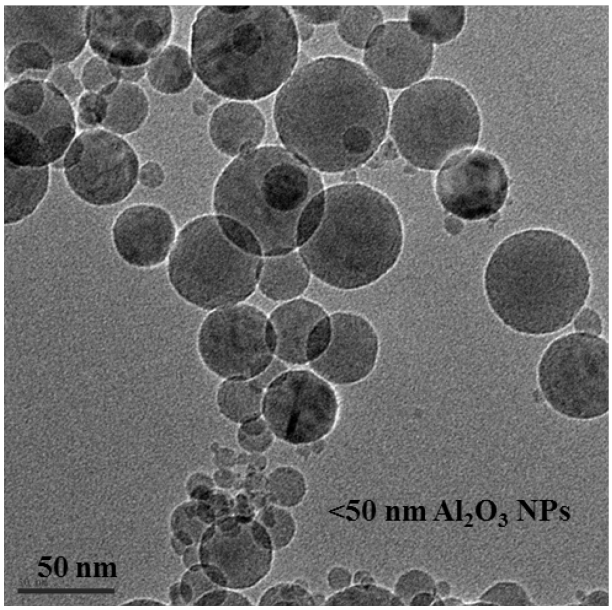

Figure 33: TEM image of the NPs used in this study Al_2O_3 (size provided by the manufacturer: < 50 nm). The size of the NPs is diverse and inconsistent with the size provided however, the shape is regular and spherical so that a size distribution can be done.

The shape of the Al_2O_3 NPs, was found to be spherical (Figure 33), but unlike stated by the manufacturer the size distribution is much larger than the < 50nm. From the TEM images, it can be deduced that the size of the Al_2O_3 NPs ranges from 10 to > 100 nm. More importantly, by comparing to TEM images of the NPs, it was possible to conclude that the MDG-spICP-MS calibration approach can provide a more accurate size characterisation of the NPs for these types of samples.

Dissolved Al^{3+} introduced as droplets through the MDG was used as standard for calibration purposes. This way, any matrix interference that would affect the Al-based NPs in the plasma will be accounted for since the calibration is done using the same element as opposed to other calibration techniques.[110] The additional TEM measurement was performed to ensure that the NPs are of a uniform size (in this case; spherical) so that the size calculation is valid. So far only laser ablation- and bulk nebulisation ICP-MS have been performed before on an Al_2O_3 sample.[142]

4.4.3 Overview

In this chapter, a couple of methods have been described to reduce the amount of ionic metals from ZnO and Al_2O_3 NP samples, so that the technique of MDG coupled to spICP-MS can be applied. With the use of an IEC column, the background noise was still too high for analysing the ZnO NPs. Therefore, repeated steps for dilution and centrifugation steps were applied on commercially available ZnO NPs of given sizes of 50 and 70 nm. The high concentration of ionic Zn present in the samples caused a high interference with signals coming from their corresponding NPs and the decrease in the background signal following separation seem to be minor. Although chromatograms showed presence of large NPs or aggregates, TEM images undertaken for the ZnO NPs revealed that the NPs are of varied shapes and generating a size distribution for the ZnO NPs is not feasible. However, by using a MDG-spICP-MS, a size distribution for Al_2O_3 NPs was successfully determined. The Al_2O_3 NPs, as with the ZnO NPs were subjected to some clean up processes before being analysed by spICP-MS. The size distribution of the Al_2O_3 in nm was obtained without the use of a reference material and a size distribution in terms of nm was deduced from the NP signals.

These experiments show that analysis of metal oxide NPs by spICP-MS in the dual configuration while applying a matrix matched calibration is possible. The hurdles and restriction due to ions causing high background or irregular shape of NPs causing problems for size distribution determination are linked to the NPs samples and cannot be attributed to the dual configuration. This work is a first step for the analysis of metal oxide NPs by spICP-MS, where a matrix matched calibration method is used.

4.5 Evaluation of acidic matrix effects on size calibration of gold nanoparticles by a dual sample introduction

In order to test the influence of acid concentration on signals from individual NPs, Montaño *et al.*[133] investigated the use spICP-MS for the analysis of silica shelled (SiO_2)-Au NPs. With these particles, the SiO_2 shell acts as a protective layer around the Au, such that the metal did not dissolve in the acid solvent. This work was done using a conventional sample introduction system with a low flow nebuliser to introduce the sample. The authors found that the Au solution were more sensitive by a factor of 200 % and the sensitivity of SiO_2-Au NPs changed only by > 3 % with HCl at concentration of up to 2 %. This resulted in either a correct or lower NPs' diameter depending on the method of calculating the transport efficiency.[95, 133] The correct size is obtained by using the 'particle size method', where the ratio of solution sensitivity to NP sensitivity determines the transport efficiency.[102]

In this section, the effect of acid on the detection of NPs by sp mode is studied with online calibration by analyte-doped microdroplets in an ICP-TOF-MS. In addition to the effect of acid on the analysis, combination of the dual sample introduction should provide insight into the location of the acid-matrix effects: if the acid only affects transport efficiency, the microdroplet signals should not be affected by acid concentration, but if acid concentration changes plasma conditions, then this will also influence droplet signals from the MDG.

4.5.1 HNO_3 vs HCl

The dual sample introduction system has been used to study the effects of an increasing acid concentration, of HNO_3 and HCl, on the size calibration of SiO_2 -Au NPs on an ICP-TOF-MS. Au solution at 250 ppb in 1 % HCl was introduced as monodispersed droplets via the MDG; the sensitivity obtained from these droplets was used for calibration. The SiO_2 coating ensures that the Au NPs are not digested in the acid solution which stabilise them makes them versatile to use. Moreover, Au NPs are well characterised NPs, which made them suitable for

use in this study. The SiO_2-Au NPs were introduced in a solution of 0 - 10 % of each HNO_3 and HCl respectively.

The experiments were performed after a routine instrumental optimisation together with Au droplets. The parameters for the subsequent experiments were kept unchanged. In this study, the sample gas flow and plasma power were retained at the value where both the sensitivity and stability of Au droplets were optimal. The use of lower nebulisation gas flow has been shown to reduce signal suppression.[71] With the use of a MDG, the selected sample gas flow is critical because not only the sensitivity of the droplet can be affected, but also its stability as it travels to the ICP-MS. The frequency of the droplet generation was set to 10 Hz so that the probability of droplet signal from the MDG merging with and Au NPs signal is substantially low. Jitter in arrival of the droplets and the slight difference in peak heights were most likely due to the sample introduction through the spray chamber which creates a turbulence at the bottom of the falling tube where the droplets get into contact with the incoming sample.[144] However, this is accounted for by using the peak area as droplet signal.

The size of the SiO_2-Au NPs was calculated on a single-point droplet-based calibration. The values of the signal intensities of the increasing acid concentration on Au droplet, SiO_2-Au NPs and the subsequent size determination of the NPs are listed in Table 9. The normalised plots in Figure 34 (b and d), represent the change in signal intensity with added HCl and HNO_3. The calculated size of the SiO_2-Au NPs is not as drastically affected as that of signal obtained from the Au droplet. There is a slight overestimation of < 10 % of the size of NPs with a change of 0 - 10 % acid concentration.

Table 9: Signal intensities of Au droplet, NPs and size of NPs with increasing [HNO_3] and [HCl] from 0 to 10 %.

[HNO_3] %	**Au signal MDG (counts / 3 ms)**	**SiO_2- Au NPs (counts / 3 ms)**	**Calculated size of SiO_2- Au NPs (nm)**

0	2731	195	71
1	2403	194	72.5
2	2191	186	73.7
5	2050	185	71.2
10	1875	184	75.9
[HCl] %			
0	2731	207	71.0
1	2403	194	72.2
2	2191	186	73.7
5	2050	185	74.0
10	1875	184	77.2

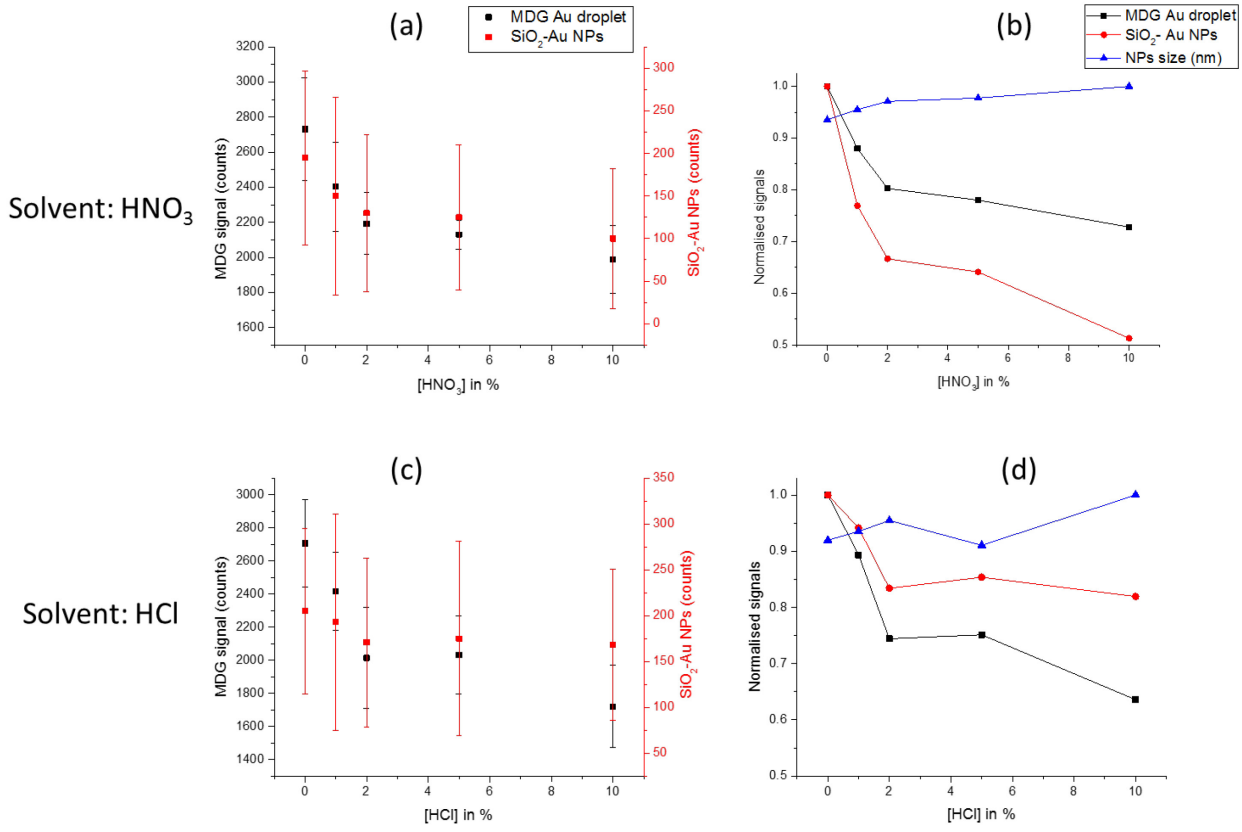

Figure 34: Effect of [HNO_3]((a) and (b))and [HCl] ((c) and (d)) on analysis of Au droplets and SiO_2-Au NPs. (a) and (c) signal intensity of Au droplets (MDG) and Au NPs (PN), (b) and (d) normalised signal

intensities, and size calculated of the NPs so that any changes in signal are comparative. Although the droplet and NPs signal intensity decreased to < 90 %, the calculated size were not drastically affected.

These results demonstrate that increasing concentrations of HNO_3 and HCl do cause a plasma-based matrix effect. Significantly, increasing concentration of acid lowers the absolute sensitivity from the ICP-TOF-MS for Au. In addition, the Au-containing microdroplets show sensitivity decrease in a similar manner, but not identical, to that of the SiO_2-Au NPs suspended in the acid-containing solution. Thus, it seems that the acid from the solution creates a range of matrix effect throughout the plasma. The cause of the difference between signal intensity attenuation between SiO_2-Au NPs and Au-containing microdroplets is not yet clear. It could be that the SiO_2-Au NPs and Au salt particles from the microdroplets vaporise and ionise at different positions in the plasma and this affects the magnitude of matrix effects experienced. The influence of HNO_3 and HCl on SiO_2-coated Au NPs with external calibration by dissolved Au in 1 % and 5 % HCl was investigated. Identical sensitivities were found for Au between these two matrix compositions (Figure 34c and d). This result contradicts that of Olesik et al. (WC 2016, Tucson),[133] in which Au signals enhancement in HCl acid caused by increased sample uptake efficiency, causes NP-diameter inaccuracies of up to 20 %. While the latter reports only sample-introduction matrix effects related to HCl concentration, here mainly plasma-related matrix effects were observed. This difference in results can be explained by the many co-dependent parameters in an ICP-MS experiment, from nebuliser and spray chamber design, various gas flows, to sampling position, to plasma power.

4.5.2 Au droplets vs Au nanoparticles

The effect of HNO_3 and HCl on the Au-droplet signals from the MDG and the SiO_2-Au NPs signals from the PN are shown in Figure 35. In both cases, a similar general trend can be seen, in which the signal intensities for both the Au droplet and the NP sample decrease. The signal suppression on the droplets and NPs are different when the solvent is HCl or HNO_3.

The Au-containing droplets from MDG are generally more affected by the presence of HCl (decrease of 35 %) than by HNO_3 (decrease of 25 %). SiO_2-Au NPs are less affected in HCl by 17 % but more affected in HNO_3 by almost 50 %. In both solvents, the size calibration of the NPs is overestimated by < 5 % but falls into the size range given by the manufacturer. Signal intensities were affected mostly in the range of 0 - 2 % of acid and decrease to a lower extent in the range of 2 - 10 % acid content. The suppression in the analyte signal could also be due to a decrease in the plasma temperature that results with increasing acid concentration.[145] This consequently reduces vaporisation and ionisation of the analyte, which results in the decrease in signal intensity for the Au droplets and NPs.

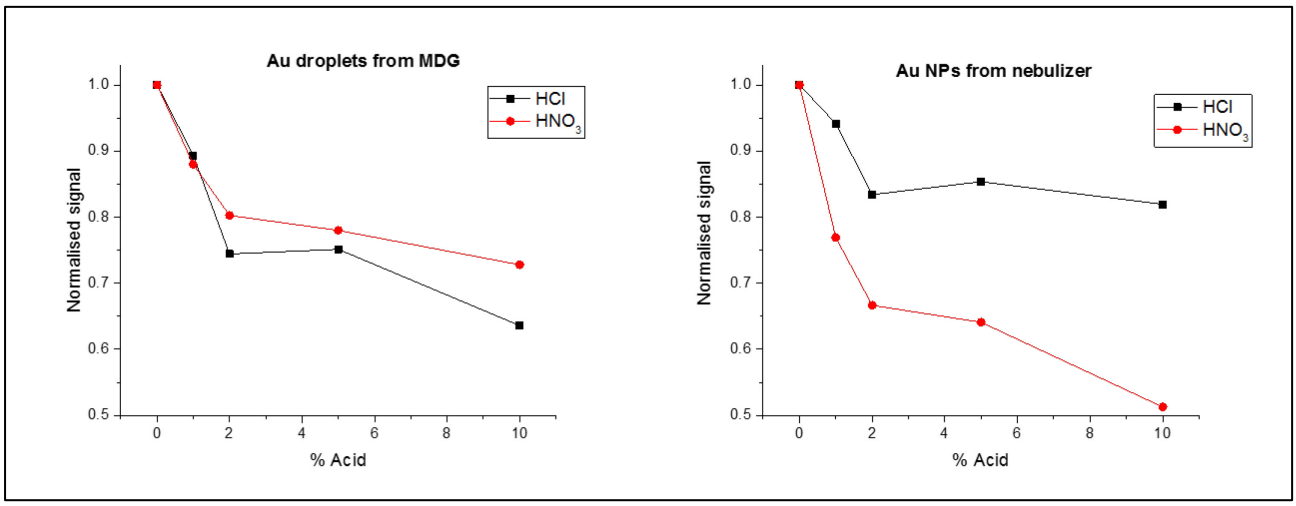

Figure 35: Comparison of acid effect on Au droplets from the MDG (a) and SiO_2-Au NPs from pneumatic nebuliser (b). These normalised plots compare matrix effects that seem to occur in the plasma (Au droplets from MDG) (a) as well as a combination of matrix effects that occur in the plasma and via sample introduction (SiO_2-Au NPs) (b).

4.5.3 Nebulisation and plasma effect

The normalised plots in Figure 35 compare the extent of signal suppression of SiO_2-Au NPs and Au droplets. This provides further insights into the effect of acids on the transport efficiencies. The suppression in signal intensity for the SiO_2-Au NPs of about 50 % is substantially lower than that of Au droplet (30 %) in a presence of increasing [HNO_3].

Since the use of a MDG would involve the introduction of a lower volume of sample, any loss of analyte through the conventional use of a nebuliser and spray chamber or any

interaction with the solvent prior to the droplets' entrance into the plasma is avoided. Therefore, sample introduced through the MDG is affected to a lower extent by effect due to acid, and this could explain why the sizing of NPs is affected to a lower extent than previously reported by Olesik et al. (WC, 2016 Tucson)[133] in the MDG-PN sample introduction technique.

In the dual sample introduction configuration, instead of using an Au NPs reference material to size the SiO_2-Au NPs, an Au droplet, acting as a pseudo NP is used and produced by a MDG. The dual sample introduction mode allowed us to distinguish matrix effects from the sample introduction, nebulisation and aerosol transport efficiency using NPs through the nebuliser and from plasma effect through the effect of the acid on the droplets.

4.6 Evaluation of elemental matrix effects on size calibration of silver nanoparticles by a dual sample introduction

With the use of a conventional method of sample introduction, i.e. nebuliser and spray chamber, droplets of varied sizes enter the plasma in a disorderly manner. This not only leads to plasma cooling but also to different spatial locations for ionisation in the plasma. With a MDG, the sample is introduced with controllable size and at a reproducible location in the plasma, and therefore offers a more quantitative approach to assess matrix effects and elucidate their origins.[84] In order to have a controlled sample introduction in terms of volume and reproducibility, Olesik *et al.*[122] conducted an experiment using a monodisperse dried micro-particulate injector (MDMI). An ICP-OES was also used in addition to an ICP-MS so that the location of the matrix effects could be studied. The mass-dependent non-spectral matrix effects were shown to occur during the passage of the ions from the plasma to the detector and not to originate in the plasma itself. Space-charge repulsion, which is the reduction in transmission efficiency of lower mass analyte ions due to coulombic interaction with heavier analyte ions, that takes place between the plasma region and expansion chamber, is an important cause of matrix effects and consequent loss in sensitivity in ICP-MS.[146-149] A similar effect was observed for a vertical MDMI-ICP-MS connection to introduce the analyte and matrix droplet.[84]

In the following experiments, the dual sample introduction system is used to introduce microdroplets, nebulised solution, and NPs, all containing the same element- Ag. This study addresses the different ways in which a matrix element affects an analyte of identical element. More importantly, this study is to investigate whether the dual sample introduction system is a reliable technique for the size calibration of Ag NPs.

4.6.1 Absence of matrix elements

In order to characterise NPs, it is important to be able to account for any matrix effect. For example, NP analytes present in foodstuffs, wastewaters, or high-salt matrices, for e.g. ocean water, will certainly need to be measured in the presence of substantial matrix effects. In conventional spICP-MS analysis, dissolved standards and NP-containing samples are both introduced via a pneumatic nebuliser and spray chamber. When this method is applied to measure NPs in environmental samples, it is difficult to know how matrix effects influence accuracy of NP mass and particle-number concentration determinations. The use of the dual sample introduction system allows the study of matrices as they act upon the calibrant microdroplets and on the NPs introduced via a PN (Figure 13). In these experiments, influence of matrix effects on the size determination of Ag NPs is studied.

Both the plasma power and sampling depth were set to the optimum values, as determined from the tuning conditions, for a robust plasma and maximum signal. The sample gas flow has been shown to strongly influence the extent of matrix effects in the ICP-MS.[80] For this reason, in these experiments, the sample gas flow rate is the parameter that is used to adjust the ion signal.

The influence of varying the sample flow rates on the signal from Ag NPs, Ag-containing microdroplets and nebulised Ag-containing solution (enriched ^{109}Ag) is shown in Figure 36. In the case of the droplets, the sample gas flow rate is crucial in making sure that all the droplets generated reach the plasma. Figure 36 shows that the gas flow of 1.03 L min^{-1} is the optimum for the analyte from the MDG, the nebulised ^{109}Ag, and Ag NPs.

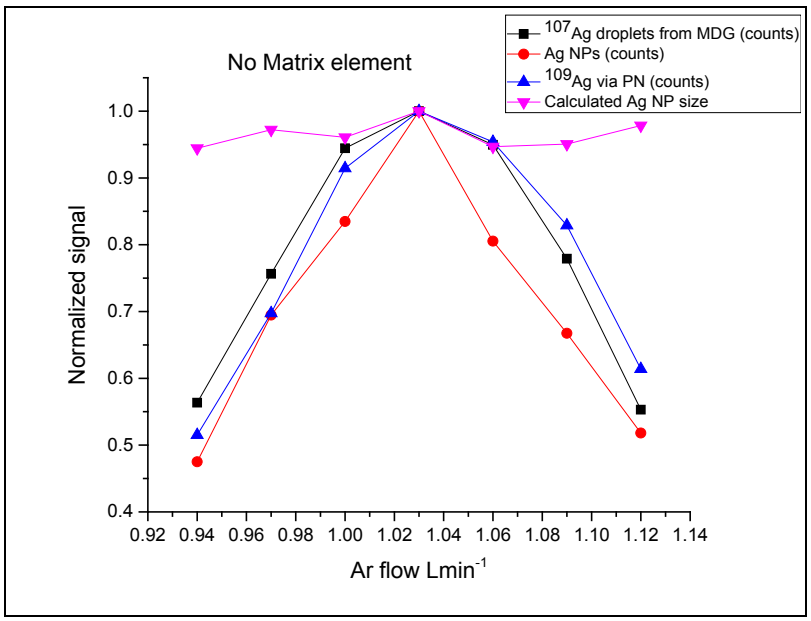

Figure 36: Effect of sample gas flow on the signal of analytes simultaneously analysed in the ICP-TOF-MS: ^{107}Ag through the MDG, ^{109}Ag and Ag NPs through the PN. The optimum sample gas is at 1.03 L min^{-1}. The calculated NP size stays mostly constant at all gas flow rates used even though the analyte signals are affected.

Table 10: The calculated size of the Ag NPs measured at different sample gas flows in the absence of matrix elements shows that the sizes fall within the range given by the manufacturer was 79.8 ± 5.4 nm. Values are given as mean ± SD (n = 3).

Ar flow L min-1	Calculated Ag NP Size (nm)
0.94	74.7 ± 22.4
0.97	76.9 ± 23.0
1.00	76.0 ± 22.8
1.03	79.1 ± 4.0
1.06	74.9 ± 22.5
1.09	75.2 ± 15.0
1.12	77.4 ± 23.2

Importantly, regardless of sample gas flow, the size calculated of the NPs remains within 5 % of the value given by the manufacturer (79.8 ± 5.4 nm), even with signal intensity from calibrant and NP samples diminished by up to 50 % at lower gas flow rates. The calculated size of the Ag NPs is listed in Table 10 and shown in Figure 36. At the optimum sample gas flow of 1.03 L min^{-1}, the size obtained for the Ag NPs is closer to the value given by the manufacturer and this includes a lower error in the calculated size.

4.6.2 Effect of sample gas flow rate on analyte signal at high and low concentrations of matrix elements

Elements of different physical properties were investigated for their matrix effects (Table 11).

Table 11: Mass, ionisation potential, melting point, heat of vaporisation and oxide boiling point of the analytes and matrix elements.[150] The elements are sorted from low to high elemental mass. These matrix elements of varied physical properties are chosen to study their effect on Ag in the form of: ^{107}Ag droplets, NPs and dissolved ^{109}Ag solution.

Elements	Molar mass of element	Ionisation potential (eV)	Heat of vaporisation KJ/mol	Boiling point of oxides (K)
^{107}Ag*	108	7.6	255	Decomposes
^{109}Ag**	109			
Li	6.9	5.4	147	2870
Mg	24	7.6	128	3870
Rb	85.5	4.2	71	NA
Cs	132	3.8	64	Decomposes
La	139	5.6	400	4470
Ce	140	5.5	350	3770
Lu	175	5.4	415	4250
Pb	207	7.4	178	1750
U	238	6.3	420	NA

*Analyte introduced via MDG
** Analyte introduced via PN

The responses of the three different Ag analytes (^{107}Ag droplets, enriched ^{109}Ag and Ag NPs) were measured in the presence of no, low (0.001 mg L^{-1}), and high-matrix (10 or 100 mg L^{-1}) concentrations of each of the matrix elements. For each of the matrix elements analysed, the notch filter on the ICP-TOF-MS instrument was applied to reduce the number of matrix ions measured and to prevent detector saturation. Figure 37 shows the effect of Li at concentrations of 0.001 and 100 mg L^{-1} on the signal of the analytes at varying sample gas flow. Similar to Figure 36, there is an optimum Ar gas flow rate of 1.03 L min^{-1} at which the

analytes display the highest sensitivity at the different matrix intensities. Differences in droplet size and therefore the magnitude of the signal were accounted for in the data analysis.

A similar response was obtained of the analytes in 0 and 0.001 mg L^{-1} Li (low matrix) matrix. With the addition of 100 mg L^{-1} of Li, the responses of the analytes are suppressed to similar extent. This shows that the analytes introduced via the PN and the MDG experience the same plasma-related matrix effect whether they are introduced in solutions, droplets or in the form of particles. Therefore, using the MDG-PN calibration method, the calculated size of the Ag NPs hardly differs in the presence of the matrix (Figure 37d).

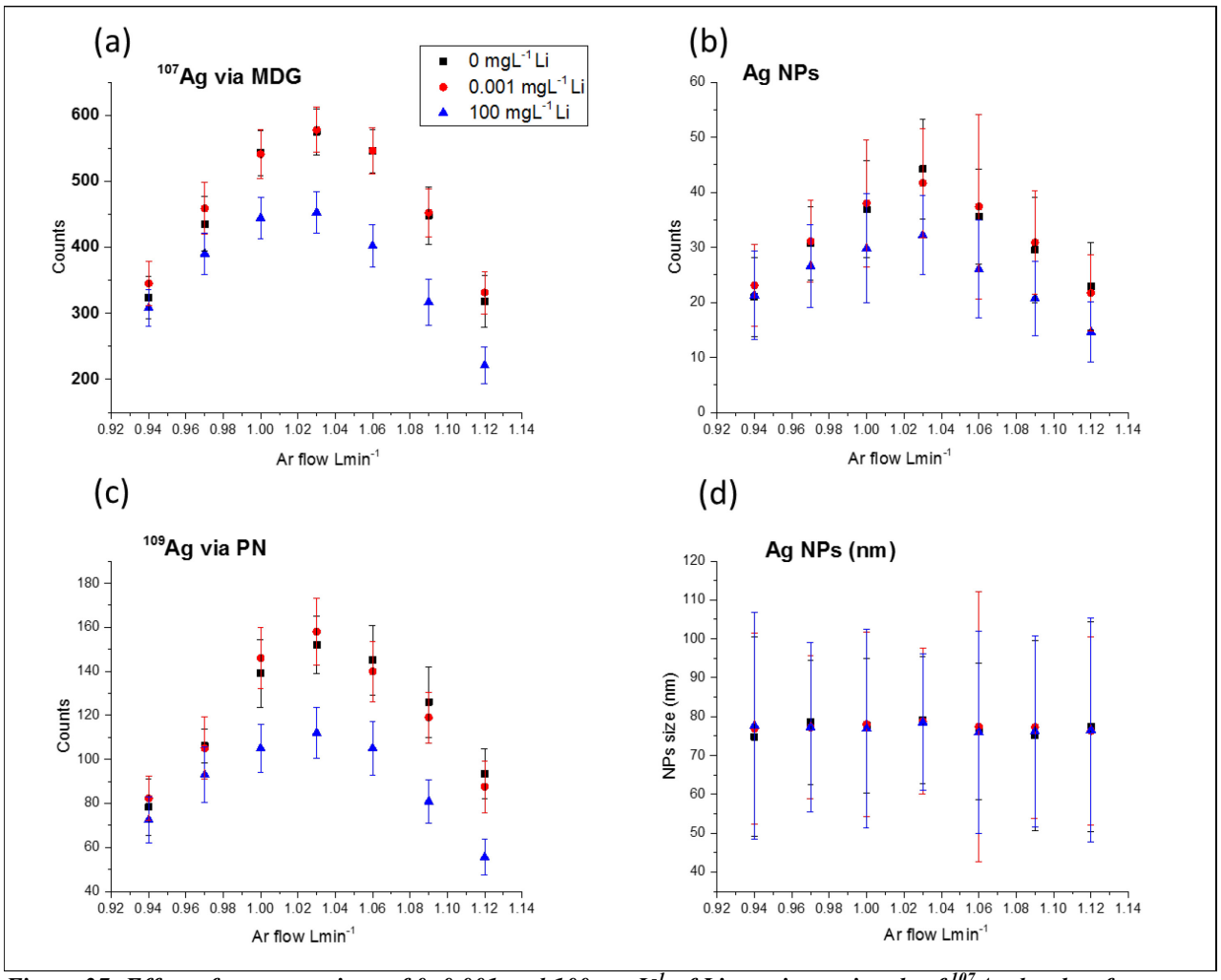

Figure 37: Effect of concentrations of 0, 0.001 and 100 mg L^{-1} of Li matrix on signals of ^{107}Ag droplets from MDG (a), Ag NPs (b) and ^{109}Ag (c) via a PN and the calculated size of the Ag NPs (d) between 0.94 and 1.12 L min^{-1} Ar flow rate. The error bars represent the variation in droplet signals (^{107}Ag), spread of the ^{109}Ag and Ag NPs. The error bars for the calculated Ag NPs size is the combination of errors from the droplet and NPs signals.

Similarly, the effect of the matrix elements of Pb, La, Mg, Lu, Cs, Rb, and Ce at low (0.001 mg L^{-1}) and high (100 mg L^{-1}) concentrations and of U at 0.001 and 10 mg L^{-1} was investigated at their optimum gas flow rate ± 0.09 L min^{-1} ranges of Ar flow rate between 0.88 - 1.06, 0.94 - 1.12 or 0.97 - 1.15 L min^{-1} (Figure 38). Since the analyses were ran on 3 different days: day 1: Pb, Mg and La, day 2: Li, Lu and Cs and day 3: Rb, U and Ce, the optimum gas flow rates differed slightly. Optimum gas flow rates were also influenced by the size of the droplets generated from the MDG and the velocity at which they were generated and travel down the falling tube.

In all the settings in Figure 38, the Ag samples follow the same trend: signal is highest for both concentrated and dilute matrix at the same gas flow rate. In the case of high concentrations of Li, Lu, Cs and Ce, there is an apparent signal suppression for the Ag samples, except for the Ag NPs in the presence of Lu. For matrices composed of U, Mg (on ^{109}Ag) and Pb (on Ag NPs), signals were enhanced at high matrix concentration. Additionally, in the case of Mg, as the gas flow rate is increased beyond the optimum flow (Figure 38), the enhancement of signals from droplets (^{107}Ag) is greater with concentrated matrix than diluted matrix. The same effect is observed for ^{107}Ag droplets and ^{109}Ag with the Pb matrix.

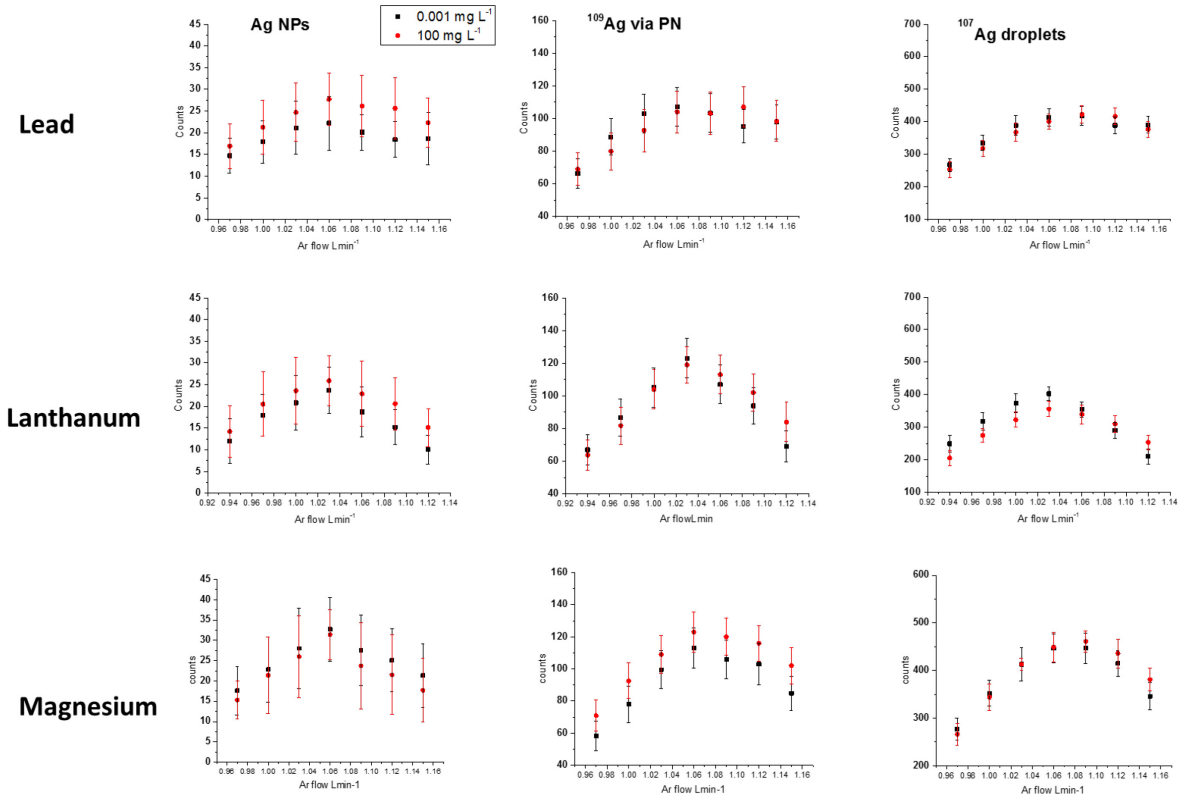

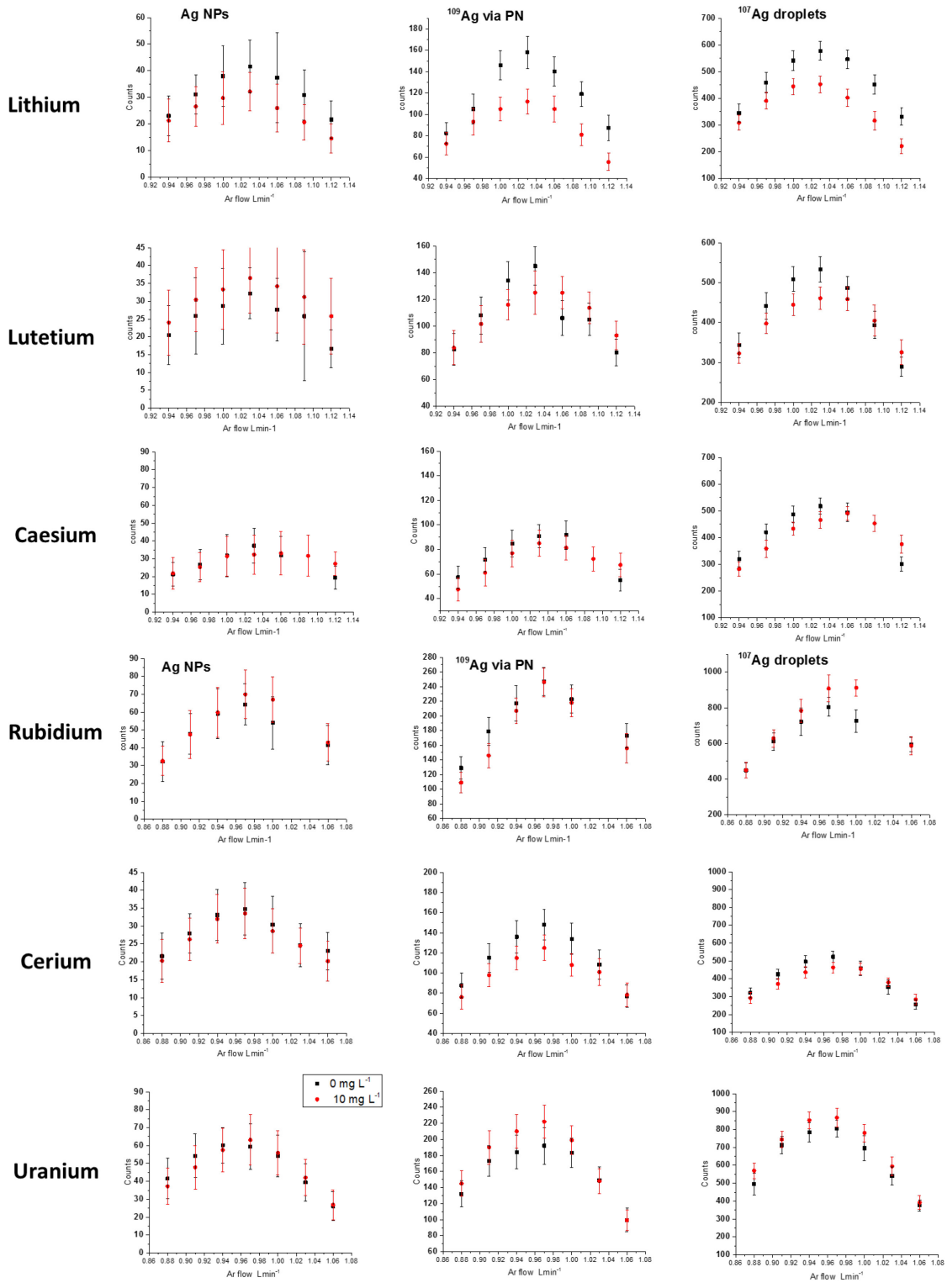

Figure 38: Effect of low (0.001 mg L^{-1}) and high (100 mg L^{-1}), except for U (10 mg L^{-1}), matrix elements' concentration on the analytes monitored at different Ar gas flow rates. Matrix studies of Li, Lu and Cs were conducted on Day 1, Mg, Pb and La were conducted on Day 2 and Rb, U and Ce on Day 3. In all cases the optimal gas flow rate is the same for Ag analytes: ^{107}Ag droplet, NPs and ^{109}Ag.

4.6.3 Effects of low to high matrix concentrations on Ag analytes

The matrix effect along the whole range of the matrix concentrations analysed is shown in Figure 39 at the optimum gas flow rate. The logarithmic graphs plotted show the effect of 0,

0.001, 0.025, 0.1, 0.25, 0.5, 1, 10, and 100 (omitted for U) mg L^{-1} of the elements on ^{107}Ag droplets, ^{109}Ag and the calculated size of Ag NPs. Signal suppression in both Ag droplets from the MDG and ^{109}Ag from PN occurs in the presence of the matrix elements: La by 15 - 20 %, Li by 30 %, Lu by 20 %, Cs by 15 % and Ce by 15 %. In the case of Rb, it seems that there is a suppression until 10 mg L^{-1}; however, for the matrix concentration of 100 mg L^{-1}, the signals are enhanced once again. The reason for signal enhancement in high Rb matrix is not yet clear and requires further study. The most noticeable signal enhancement occurs in the presence of U for both the Ag analytes. In Mg, the signal enhancement of ^{109}Ag throughout an increasing matrix concentration and gas flow rate (Figure 38) is clear, but the response of ^{107}Ag droplets stayed constant with increasing matrix concentration.

As seen from the plots of La, Li, Lu, Cs and Ce, these single-element matrices all cause signal suppression on the Ag samples with increasing matrix concentration. One physical property they have in common is their relatively low ionisation energy (Table 11). Elements of lower ionisation potential were observed to cause a more severe matrix effect than elements of higher ionisation potential.[80, 81] In this study, the analyte (Ag) has a higher ionisation potential than all the matrix elements used except for Mg. And indeed, the same effect of suppression is observed with the low ionisation potential matrix elements of La, Li, Lu, Cs, Ce and Rb (except for signal from 0.001 mol L^{-1} is absent). Another common characteristic of those matrices is their lower atomic mass compared to that of Ag - 107 and 109.

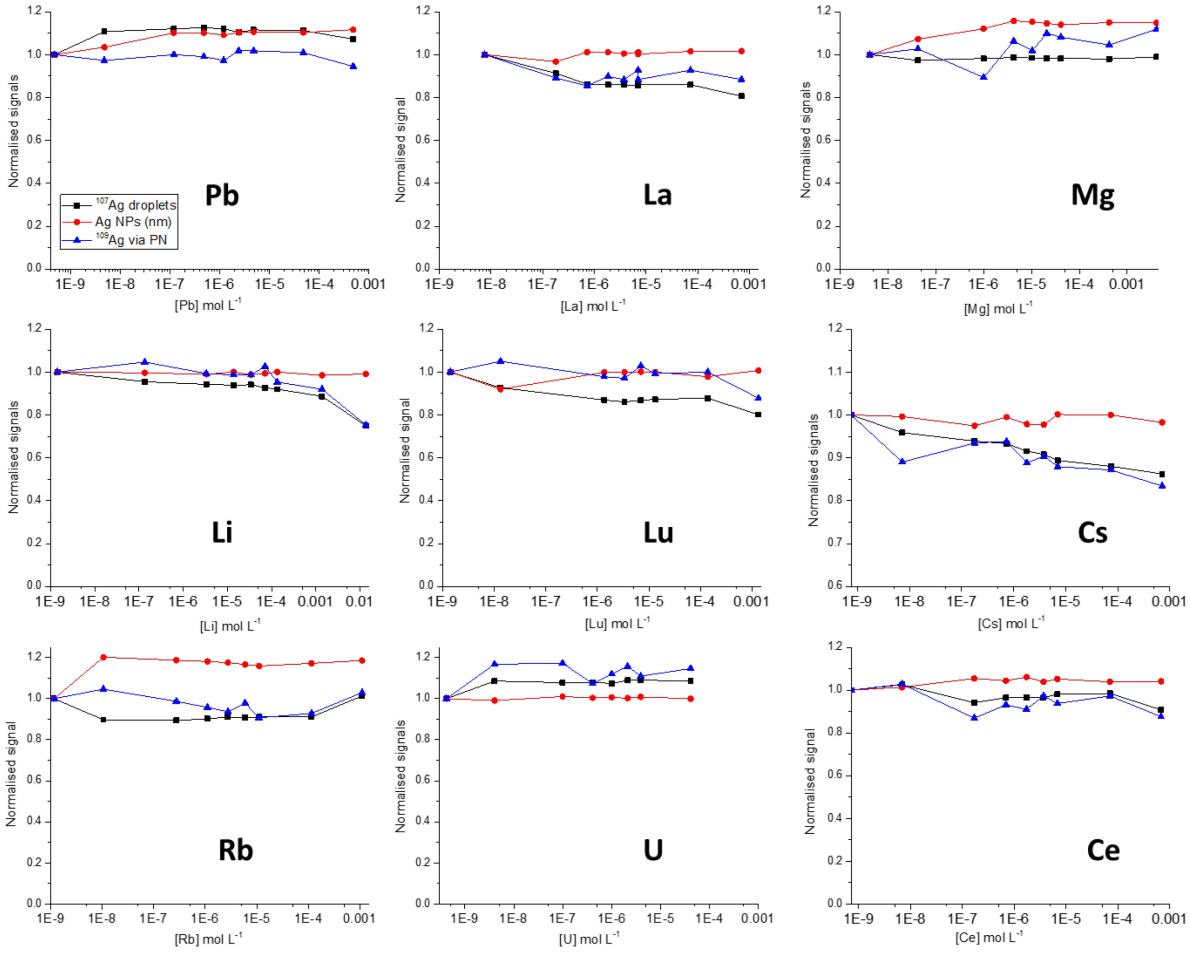

Figure 39: Normalised signal of ^{107}Ag droplets (MDG) and ^{109}Ag (PN) and calculated size of Ag NPs as a result of increasing matrix concentration introduced along with the Ag NP and enriched-^{109}Ag via a PN. The legend shown in graph Pb applies to all the other plots. The data plotted for each of the element matrix were calculated at their optimum gas flow rates in matrix concentrations of 0, 0.001, 0.025, 0.1, 0.25, 0.5, 1 , 10 and 100/ (omitted for U) mg L^{-1}.The concentrations of the matrix elements in the graphs are given in terms of their molar concentration.

There are theories about the mechanisms[147, 148] to explain the causes of matrix effect as a result of the low ionisation energy of matrix element, more commonly known easily/efficiently ionised elements (EIE). One of the mechanisms of the EIE effect on the analyte ions is known as the lateral diffusion interference.[78, 151] It involves the change in the analyte ion and atom density in the central plasma zone, due to the presence of EIE which affects the rate of vaporisation of the ions. This, in turn, encourages the ions to shift or diffuse off axis from the central plasma zone hence known as the lateral diffusion interference.[77, 79, 152] Another effect of the EIE occurs as a result of plasma cooling; the vaporisation of the

large concentration of matrix would consume large amount of plasma energy and in turn reduce atomization of the analyte.[77] However, in this work, Rb which has the second lowest ionisation potential, does not conform to the trend, therefore none of the mechanism connected with the ease of ionisation of the elements can be applied. In order to draw effective conclusions about the applicability of EIE, this study can be extended to investigate the effect of a wider number of matrix elements with similar ionisation potential on elements of variable ionization potential.

As for U, although it has an ionisation potential lower than Ag, the matrix element resulted in a slight increased sensitivity for the Ag droplets and ^{109}Ag. This is possibly because of the higher mass of the U decreases the impact of the effect of its low ionisation potential. Nevertheless, heavier matrices are known to cause more severe matrix effects and the lighter elements are more affected as a consequence.[80] In this work, the lighter elements are the Ag analytes in the 3 different forms and the heavier matrix is U. But instead of experiencing a stronger suppression due to a combination of the U being easily ionised and a space charge effect, the Ag signals are not suppressed. According to Horlick and Tan.,[80] the suppressive effect of the U as a matrix is not displayed until the matrix concentration is above 10 mg L^{-1}.[80] In this project the maximum [U] was 10 mg L^{-1}. This was to avoid detector saturation, as even if the notch filter is applied for U, the signal from the Ag was also affected. Another high mass matrix analyte used in this work is Pb, which in this work gave different results than expected; with an overall suppression of ^{109}Ag (5–10 %) and signal enhancement of ^{107}Ag (5 %).

Another observation from this work is that the sample introduction technique does not seem to have a major impact on the analyte signal. The overall signal for the analytes ^{107}Ag introduced as discrete droplets from the MDG and ^{109}Ag/Ag NPs introduced together with the matrices seem to follow a similar trend. Had a matrix effect due to the type of sample introduction been seen, the signal change in the ^{109}Ag and Ag NPs would have been more

different. Therefore, contrary to what was previously proposed and reported, matrix effect due to the use of a nebuliser and spray chamber has not been observed in this work.[71, 73]

4.6.4 Correlation of matrix effect with physical parameters of matrices

In order to better understand and rationalize the origins of the matrix effects observed, in this section, correlations between the observed matrix effects and physical constants of the matrix elements is explored. Figure 40 shows the effect of increasing matrix-element mass on the Ag signal from droplets. In an environment of low matrix concentration ($1E^{-9}$-$1E^{-7}$ mol L^{-1}), the ^{107}Ag droplets are affected to a lower extent by the elemental mass than in the presence of a high concentration of matrices ($1E^{-5}$-$1E^{-2}$ mol L^{-1}) as it was expected. With the exception of Mg and Rb, the low-mass matrices suppress Ag signal, whereas for the higher mass (Pb and U), slight signal enhancement is observed, though this enhancement does change with increasing matrix concentration.

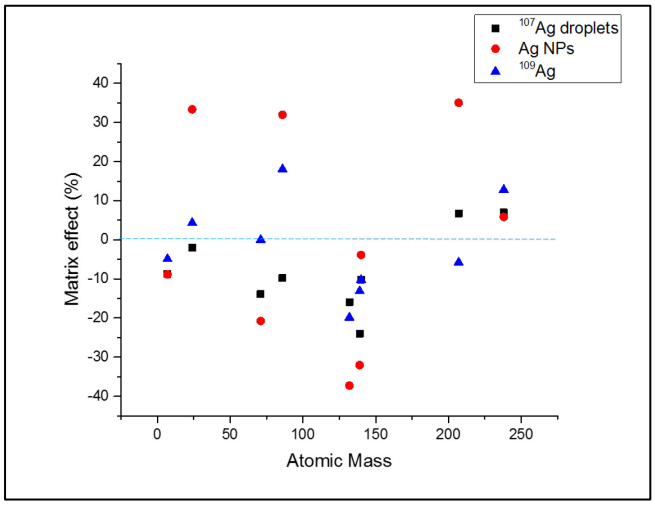

Figure 40: The effect of elemental mass on the ^{107}Ag droplet, Ag NPs and ^{109}Ag solution via PN at matrix concentrations within $1E^{-4}$ - $1E^{-5}$ mol L^{-1}.

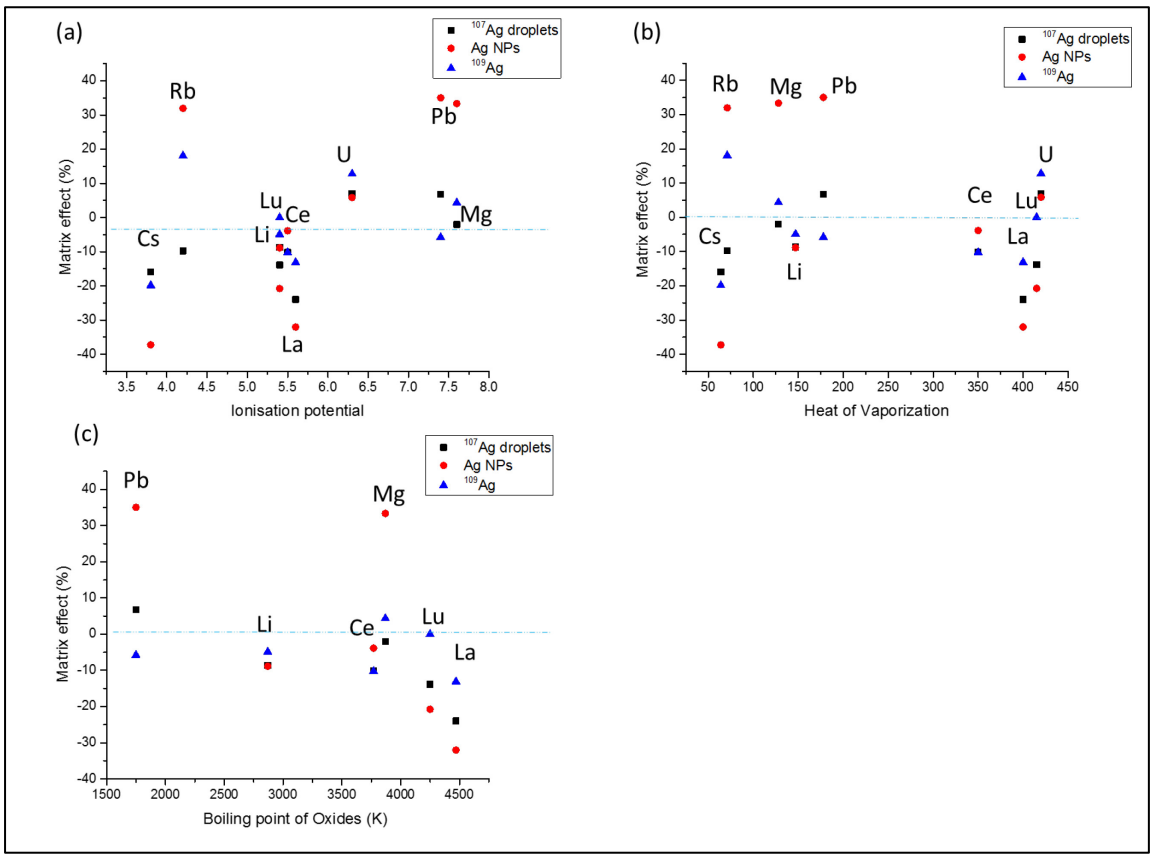

Figure 41: (a) Effect of increasing ionisation energy of matrices, b) increasing heat of vaporisation of matrices and, c) increasing boiling point of the oxides of the matrices on ^{107}Ag droplet, Ag NPs and ^{109}Ag. The concentrations of the matrices are all within 1E^{-4} - 1E^{-5} mol L^{-1}. The boiling point of Rb, Cs and U are not available as they decompose before reaching boiling point.

While most of the matrix elements have a suppression effect on the analytes, there seems to be a general tendency towards a higher or no matrix effect as the ionisation potential of the matrix elements increases. In the plot of heat of vaporisation vs matrix effect, there seems to be no clear trend. However, in both the cases in Figure 41a and b, the Ag NPs seem to experience a stronger matrix effect, than ^{107}Ag droplets and ^{109}Ag, as enhancement or suppression. The matrix effect experienced by ^{109}Ag is in turn higher than for ^{107}Ag droplets. This could mean that the way in which the sample are introduced into the plasma play a role in the extent of the matrix effects. Therefore, it could be that in addition to experience plasma related matrix effect, the Ag NPs and ^{109}Ag are also experiencing matrix effect during sample introduction.

Other physical aspects of the matrices which were initially expected to affect their impact on the Ag analytes are shown in Figure 41. The notable trend is the impact of the ionisation potential, with elements of low ionisation potential having a strong suppression on the signal of ^{107}Ag droplets and ^{109}Ag as discussed above except Rb, which does not seem to follow the trend. With an increasing boiling point of the oxides of the matrices, there seem to be general trend of suppression of the analytes, with the exception of Ag NPs in the presence of Mg and Pb. One explanation can be that the matrix ions with high oxides boiling point causes the ionisation of the matrices to occur closer to the sampler and therefore pushes the ions of the matrix towards the sampler while the analyte ions are pushed away from the central axis leading to the sampler.

Despite the varied effects of the elemental matrices on the different Ag analytes; droplets, solution and NPs, the mean size calculated of the Ag NP stays at a close range of 76.1 - 80.2 nm (Figure 42) in a high concentration of matrix.

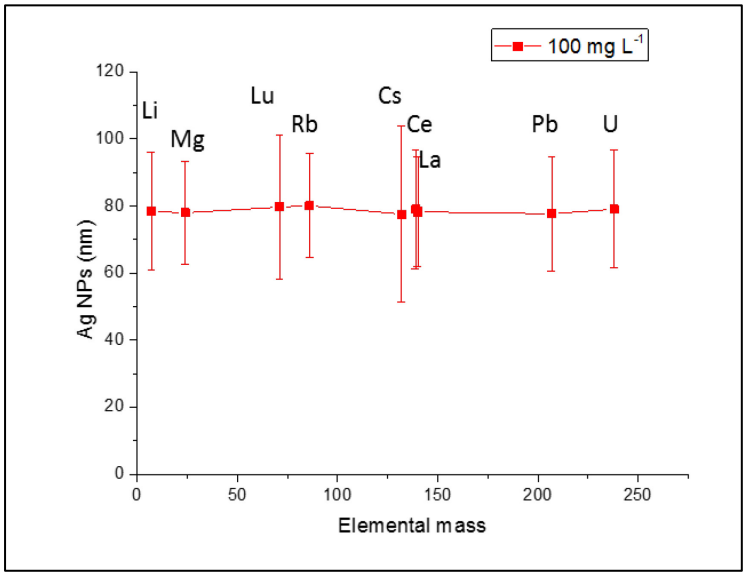

Figure 42: The calculated size of Ag NPs including relative standard deviation in the matrices at a concentration of 100 mg L^{-1}(U: 10 mg L^{-1}) In the presence of the different matrices, the calculated size of the Ag NPs falls well within the given range. The presence of high matrix concentration has no effect on the size determination of Ag NPs.

The fundamental aim of this work was to investigate if the matrix content of the sample introduced along with the Ag NPs impacts the size characterisation of the NPs. This shows

that the dual sample introduction system is a reliable technique in the characterisation of NPs, in various matrix environments. Eventually, in this matrix study, none of the particular physical property analysed showed of the matrix elements influenced the analysis of NPs.

4.7 Application of the microdroplet generator with an inductively coupled plasma time of flight mass spectrometer in the characterisation of particles in environmental water samples

The recently commercially available ICP-TOF-MS has opened the door to new possibilities in simultaneous elemental analysis. The high time resolution achievable by ICP-TOF-MS allows for the detection of NPs in the sp mode.[64, 66] This, therefore, enables the detection of the various NPs present in the sample as single particles, while also providing information on these particles multi-element/isotope compositions, which could, in some cases help decipher the source of individual particles. There are some fundamental differences between natural and engineered NPs. In their natural state, NPs can exist as complexes with other elements, whereas engineered NPs can be traced back due to their single elemental composition or multi-element composition but of consistent isotope distribution. Engineered Ceria NPs, for e.g. consist of Ce in its oxide form whereas in its natural state it occurs together with other rare earth elements (lanthanides).[49] Together with a machine-learning analysis, the capabilities of spICP-TOF-MS have been shown in a multi-element fingerprinting method, where the discrimination between naturally occurring Ceria and engineered Ce was made in an environmental sample.[153] Nevertheless, with a limited number of standard reference NPs available, characterisation of diverse natural and engineered NPs is a challenge.

In this chapter, the capability of the dual sample inlet system,[144] MDG-spICP-TOF-MS, in the characterisation of macro and nanoparticles in four water samples is demonstrated. In the absence of appropriate reference NP materials, the calibration is done by microdroplets composed of multi-elemental solutions. Since the analysis is performed on environmental samples without known composition and quantity of macro- and nanoparticles, the following characteristics of a mass analyser are required: simultaneous multi-element detection, short and fast analysis time and a high throughput analysis; all of which are satisfied by a TOF analyser. Furthermore, the multi-elemental content of particles are reported.

4.7.1 A multi-elemental droplet for size calibration of SiO_2-Au NPs

So far, the size characterisation has worked when a range of matrices were introduced through the PN along with the sample of NPs and when the calibrant consisted of a single element; that of the standard NPs. However, when an unknown sample is to be analysed for NPs, the calibrant from the MDG should be made up of > 1 element. In order to make the most of ICP-TOF-MS, the calibrant should consist of a range of elements, so the size characteristics of the NPs, as single- element or complexes, can be achieved efficiently. Therefore, in this proof-of-concept study, the first step in the analysis of environmental samples is to ensure that the dual-sample introduction system is still effective when the calibrant is made up of a solution of multiple elements. Figure 43 shows that the signals of a multielemental droplet are regular, a prerequisite to use them for calibration.

Solutions for calibration purposes were made of a series of multi-elemental concentrations (0 - 500 µg L^{-1}), each including a fixed concentration of Au of 250 µg L^{-1} (Figure 44). A sample consisting of SiO_2-Au NPs and Rh was introduced to the ICP through a PN. The purpose of the Rh is to take into account any drift in the signal of the Au droplet.

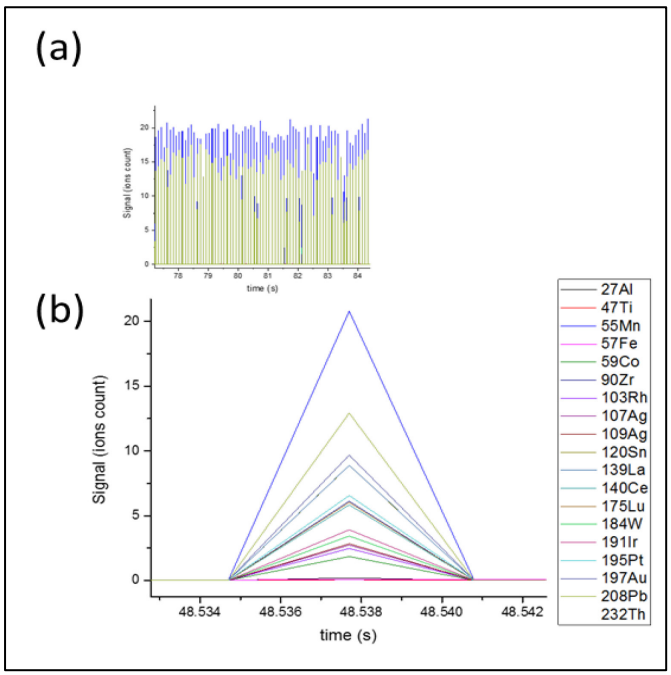

Figure 43: Signals of a single droplet consisting of multi-elements used for the calibration of particles in the samples of water (b). The inset shows part of the measurement over a period of 7 seconds (a). The droplet generation and detection are shown to be regular.

There is a linear increase in counts with increasing concentrations of an element of the multielemental solution, shown for In in Figure 44a. In the presence of a multiple elements in the calibrant, the signal of the Au droplet and the corresponding response of SiO_2-Au NPs decreases (Figure 44b) significantly as the concentration of the multi elements increases. The suppression of the signal of the Au could be most due to a combination of lateral diffusion in the central plasma zone[78] and space charge effect as the ions make their way between plasma region and expansion chamber.[146] As the concentration of the matrix ions increases, more $^{197}Au^{+}$ are repelled from the ion beam that makes it to the detector. However, the size calibration using the MDG and PN for the SiO_2-Au NPs still remains within the range, as shown in Figure 44c, provided by the manufacturer (72.4 ± 5.1 nm). Therefore, for the characterisation of a sample consisting of NPs of unknown sizes and composition, the calibration with a multi-elemental droplet is possible.

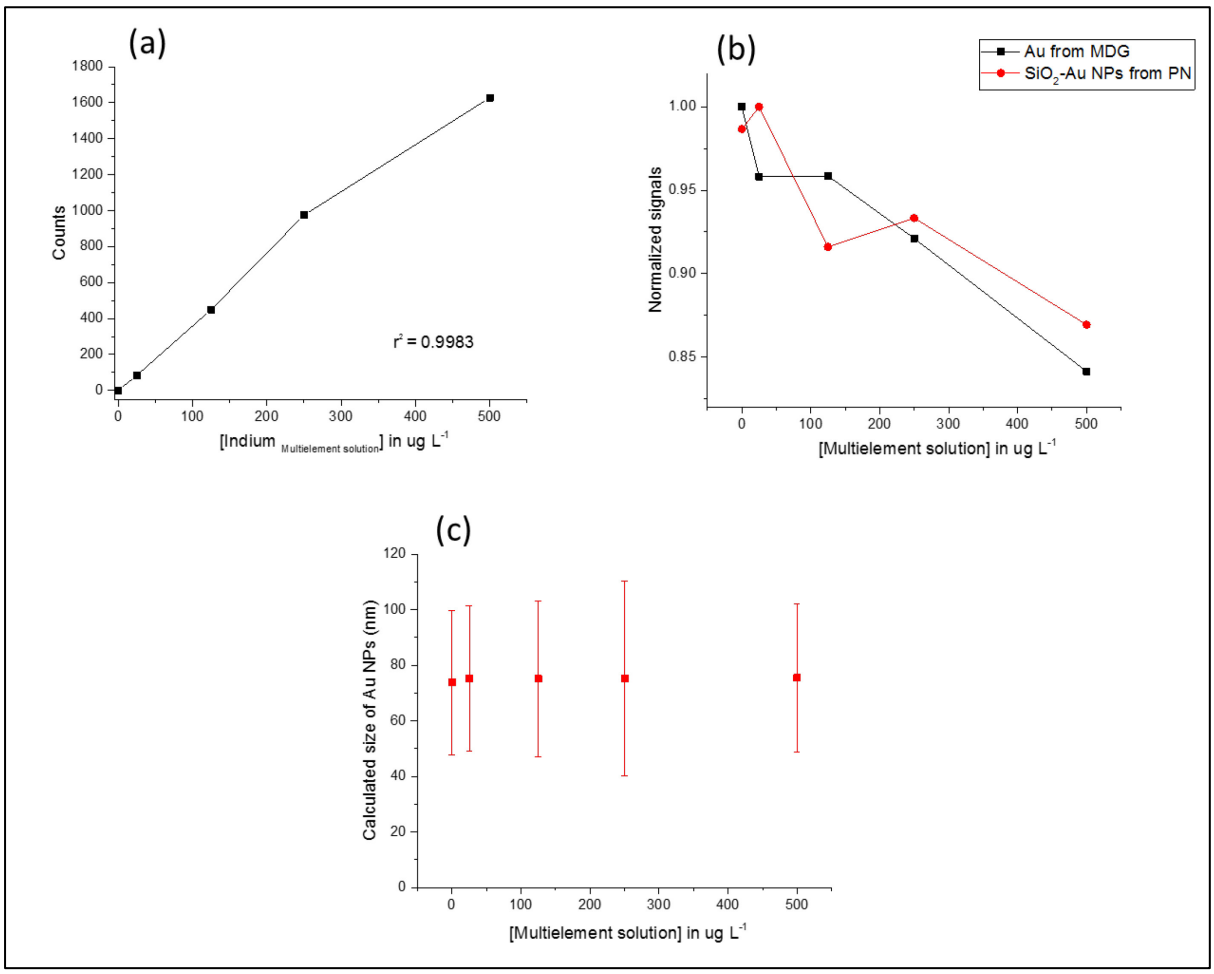

Figure 44: Effect of multi elemental droplet on size calibration. (a) Response of Indium with increasing concentration of In in a multielemental solution. The concentration of the other elements in the multielemental solution is increased to and always identical to the concentration of In. (b) The response from the 250 µg L^{-1} Au droplet and the corresponding response of SiO_2-Au NPs as the multielemental concentration is increased. (c) Calculated size of the NPs across the different concentrations of the elements in the droplet.

4.7.2 Environmental water samples

4.7.2.1 Effluent from HCI Building in ETH Zürich

After the multi-elemental droplets were analysed with ICP-TOF-MS, the water sample collected from four different sites were measured; effluent water from the HCI building at the ETH, water from Limmat river, Lake Zürich and Rhine River were analysed. The calibrant was prepared as a multi-elemental solution to be introduced as droplets from the MDG and environmental samples were introduced via the PN. The method for the calibration of NPs using a MDG-spICP-MS is outlined in Chapter 4.2. The elemental mass in each NP was

determined assuming natural abundance of the isotopes (i.e. the ratio of isotopes in the elements are present naturally) in the particles.

The pie charts below represent the contents of the water samples in terms of particles or aggregates. The particles shown are the ones with particle events of > 10 peaks during a run time of 3 mL of sample with the exception of 6 mL run time for the Effluent sample.

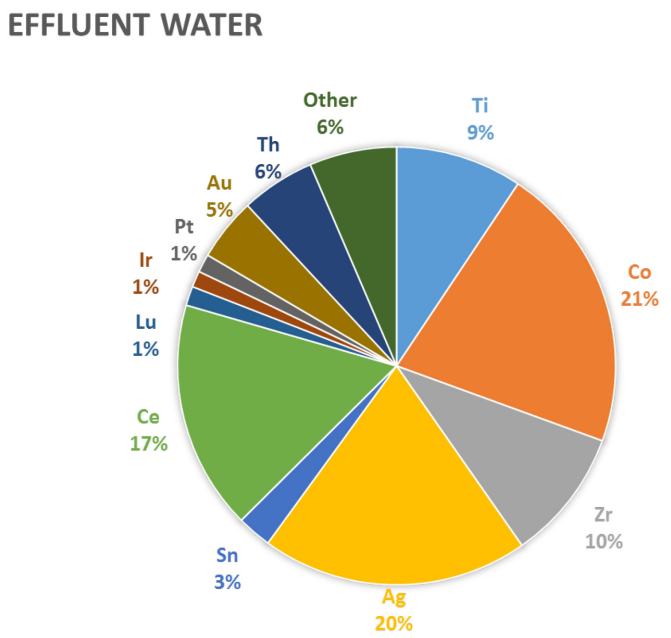

Figure 45: Particles present in a sample of effluent water from HCI building (ETH, Zürich). Other include Mn, Ni, Cu, Rh and W. The pie chart represents 2.56 x 10^3 particles L^{-1}.

A general overview of the particle content of the effluent water is shown in Figure 45. The pie chart shows the particles present in the Effluent water and the size distribution (in terms of size) is shown in the form of histograms (Figure 46). The particles shown are the waste collection from the chemistry labs in the whole building, the particles are therefore mainly engineered. Co, Ag and Ce are the most used particles in the labs. Co and Ti particles are of a broad distribution range with particles between 0 and up to 120 fg. When diluted in the effluent water, some NPs have probably dissolved or formed aggregates in contact with the various chemicals present. The particles shown in the histograms are present as single element particles in the effluent sample.

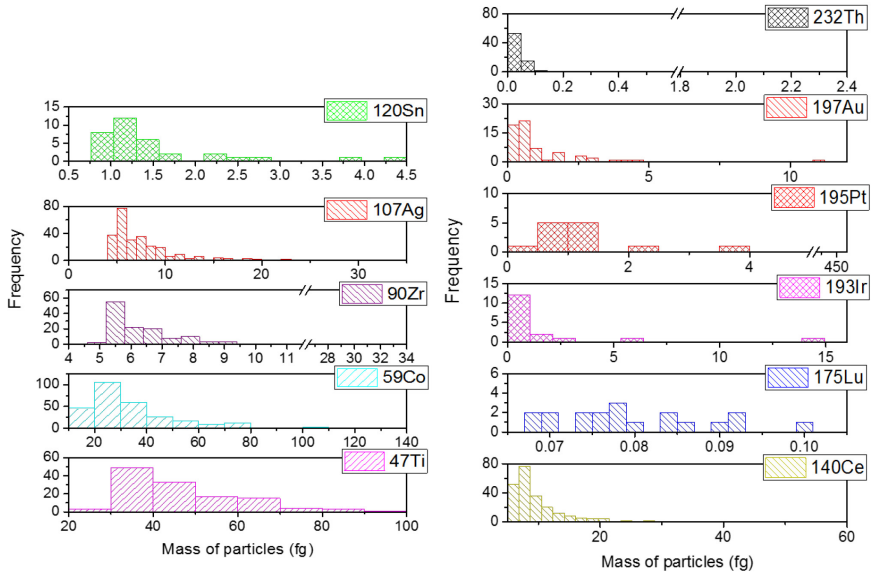

Figure 46: Size distribution (in mass) of particles of the effluent from the chemistry building HCI at the ETH Zürich containing the indicated elements.

4.7.2.2 Water sample from Lake Zürich

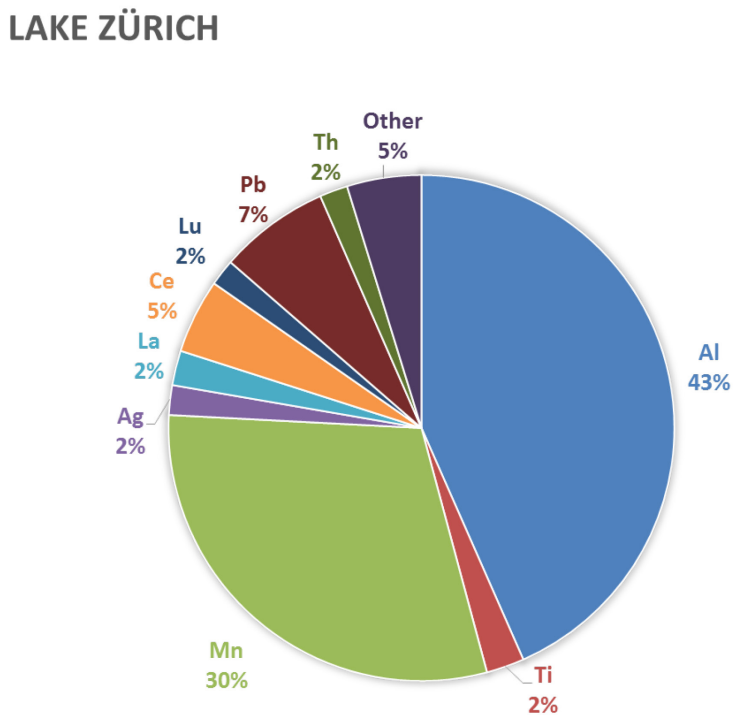

*Figure 47: Particles present in a sample of water from Lake Zürich. *Other include:* **Zn**, *Zr, Rh, W, Ir, Pt, Au ,Rh and W. The pie chart represents 9.09 x10^{2} particles L^{-1}.*

The particle content of Lake Zürich is presented in Figure 47 and their size distribution is shown in Figure 48. Naturally occurring ^{55}Mn and ^{27}Al, which are among the most abundant

elements in the earth's crust, also makes up most of the Lake's water sample analysed. The sample collected for Lake Zürich was close to the shore on a rainy day in May and at this time, it was not the bathing season yet. This can be seen in the pie chart and histograms as the percentage of Ti was low and no particles of Zn, ingredient of sunscreens, could be seen. However, as seen from Chapter 4.4, Zn NPs are very unstable and tend to dissolve. Had the Lake sample been collected on a different day/time, the elemental trace and distribution would be different. The mass distribution of Al, Ti and Mn show that they are the larger particles present.

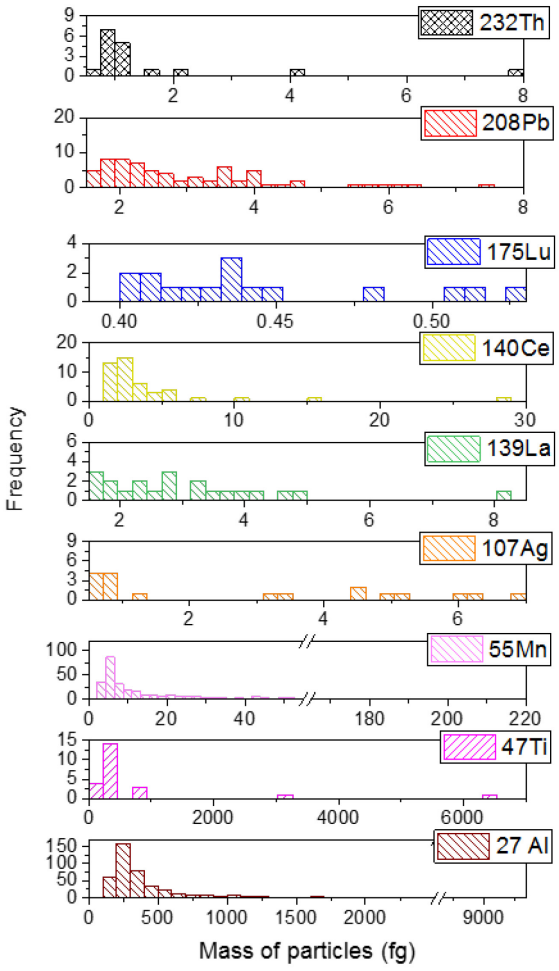

Figure 48: Size distribution (in mass) of particles of Lake Zürich containing the indicated elements.

With the growing use of NPs, ENPs can be found in the same water bodies too. The most accurate way to determine the source of a Ce-containing NPs/particle with ICP is to use a TOF device as mass analyser. In Figure 49, the presence of both natural and engineered Ce-

containing particles[49] was detected in a single run and this is only possible with the use of a mass analyser for simultaneous detection of the isotopes. Distinguishing between ENPs and naturally-occurring Ce NPs has already been shown to work with the combination of spICP-TOF-MS and machine-learning.[153] Although present in low concentration, particles of Ag-Au were also present in Lake Zürich (Figure 49).

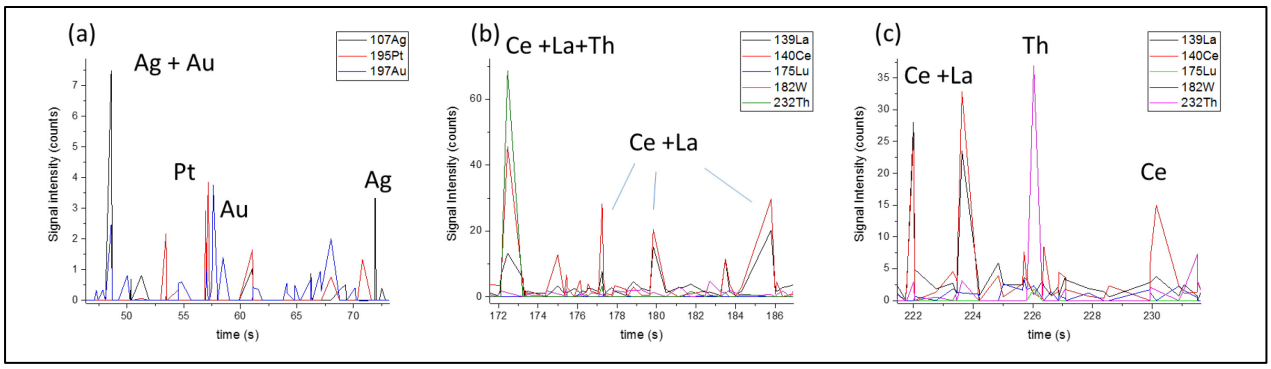

Figure 49: Particles of mono and multi-elemental nature in Lake Zürich. (a) Ag-Au and Au, Ag and Pt only particles. (b) Particles of Ce-La-Th and Ce-La. They are both naturally occurring NPs. (c) Ce-La, Th and Ce particles with Ce-La being naturally occurring and Ce particle is engineered. The ratio of the elements in the particles are varied in all the cases.

4.7.2.3 Water sample from Limmat River (Zürich)

The sample from the Limmat River was collected from a residential area, with the river flowing downstream from Lake Zürich. The particle content of Lake Zürich and Limmat River, are also very similar to each other (Figure 47 and Figure 50), since the river stems from the Lake. Lake Zürich and the Limmat River are located in a city and are surrounded by residential areas, factories and traffic. Moreover, there are highly frequented beaches around the lake, therefore there is a high probability of finding NPs present in sunscreen in the summer time. All these factors are important when it comes to the particle content of the water bodies, as the engineered particles are leeched into the water in addition to the already present natural particles. The presence of a higher concentration of some particles, namely Zr, W, Ir, and Au can be a result of the location at which the sample was collected. In contrast to the size distribution of particles in Lake Zürich, the particles in Limmat River are on average

smaller in mass (Figure 51 and Figure 48). This could be due to the change in the chemical property (such as pH, acidity and dilution) of the water as it flows through the residential areas with different influx of water on its path.

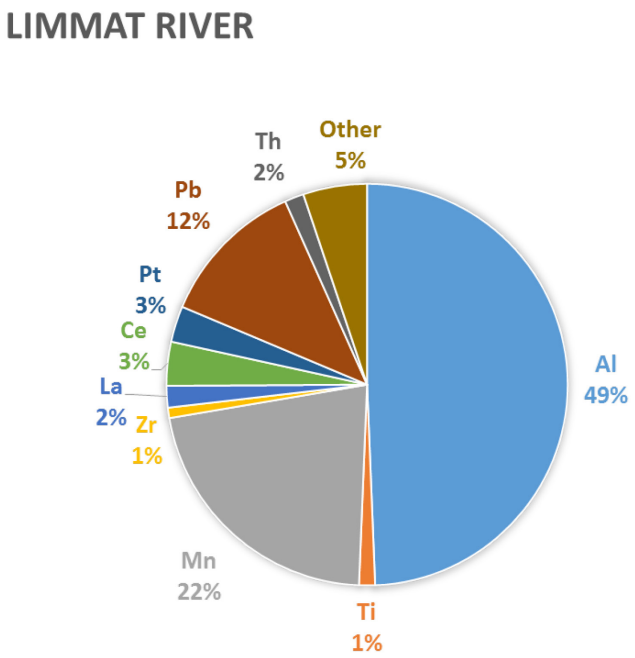

Figure 50: Particles present in a sample of water from River Limmat. *Other include: Ni, Cu, Zn, Zr, Rh, Ag ,Sn, W, Ir, and Au. The pie chart represents 1.49 x10^3 particles L^{-1}.

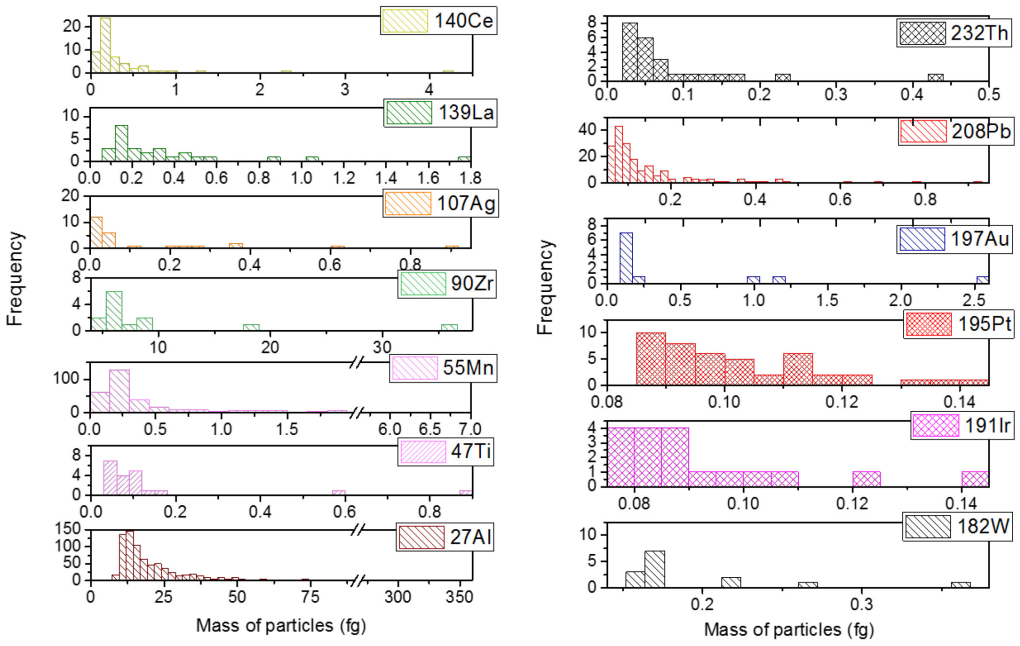

Figure 51: Size distribution (in mass) of particles from Limmat River containing the indicated elements.

Along with single-element particles, particles of multi-elemental composition can also be found in the natural water samples in the Limmat River. Particles of Ce together with other Lanthanides are present naturally in the soil and therefore can be found in natural waters[49] (Figure 52a and a1), as shown in a sample of the Limmat River.

In addition to naturally occurring Ceria particles, particles of Cu-Ag-Au were also detected in the Limmat River (Figure 52). This combination of elements could be from particles originating from an Au ore, which consist of traces of Ag and Cu. Additionally, large spikes in the signal from Ir-Pt were detected when the sample was analysed on the same day as it was collected. The Ir-Pt particles dissolved by the time a calibrated measurement was done on the following day. Alloy of Ir-Pt, used as microelectrodes for medical purposes, could have been freshly suspended particles from the surrounding of the Limmat River.

4.7.2.4 Water sample from Rhine River (Basel, Switzerland)

The Rhine River is the second longest river in Europe and sources from the Swiss Alps. In this work, the river water sample was collected in Basel (Switzerland), and therefore has not yet travelled so far, in comparison to the total distance the river covers. The pie chart (Figure 53) shows the number and concentration of particles present in the sample collected. The different elements of Ti, Ag, Ir and Pt are assumed to be from the same particle. The average size of particles of Mn, Al and Ti are also much bigger in the river Rhine than in river Limmat.

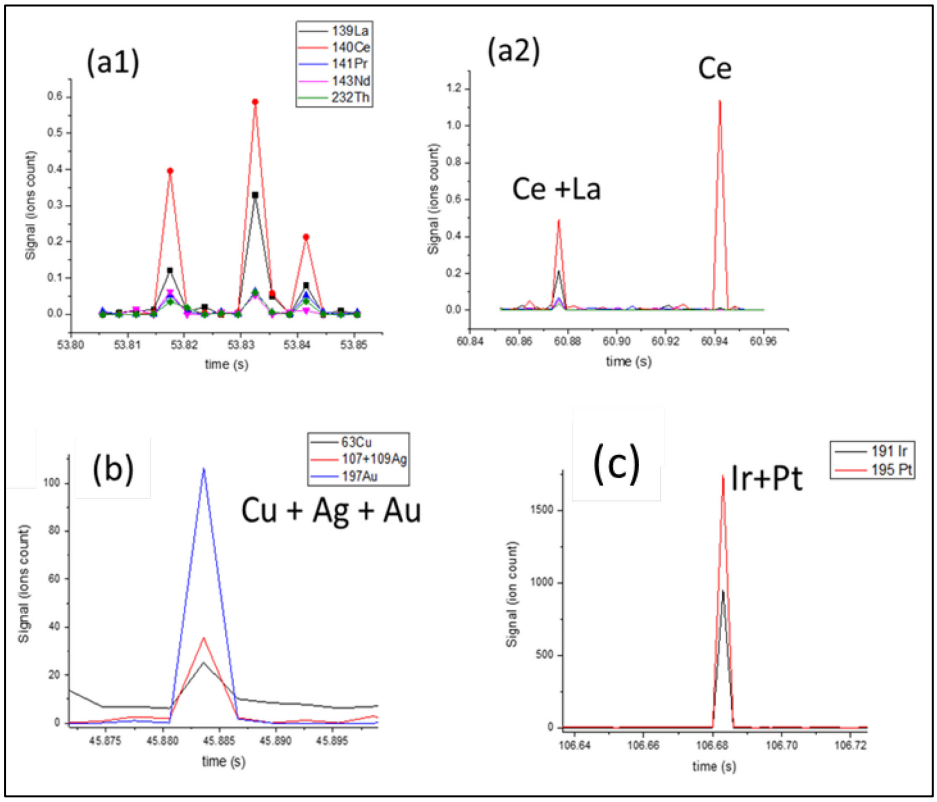

Figure 52: Presence of multi-elemental particles in Limmat River: natural particles of Ceria (a1), presence of Ce as part of a multi-element particle and on its own (a2) a Cu-Ag-Au particle which could be from a naturally present ore (b) presence of high intensity signals of Ir and Pt particles (c).

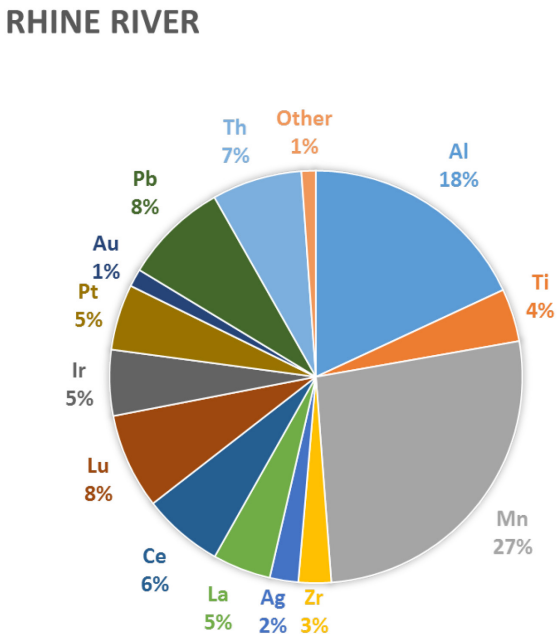

*Figure 53: Particles present in a sample of water from Rhine River. *Other include: Co, Cu, Zn, Rh, Sn, and W. The pie chart represents 2.90 x10^{3} particles L^{-1}.*

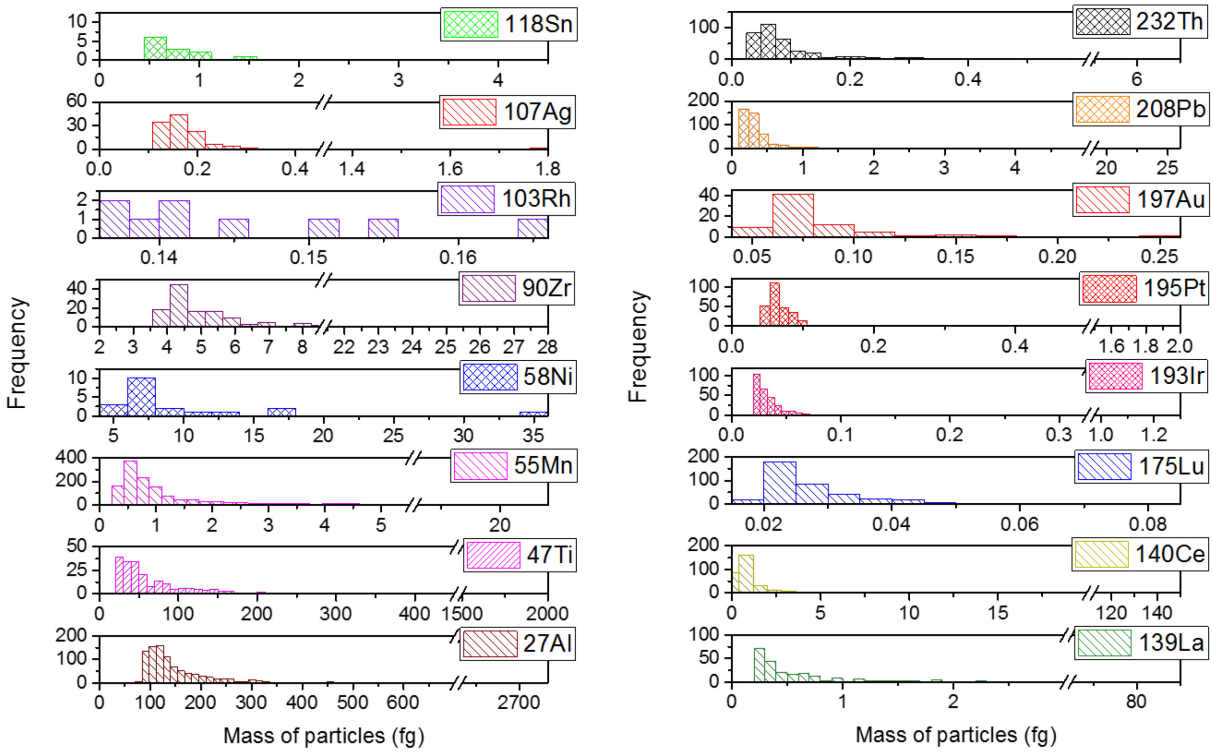

Figure 54: Size distribution (in mass) of particles from River Rhine containing the indicated elements.

The water sample collected from the river, was done at the river shore in the town centre of Basel on a rainy day. Similarly to the sample of Lake Zürich, the water content would be slightly different had the sample been taken on a different days and climate.

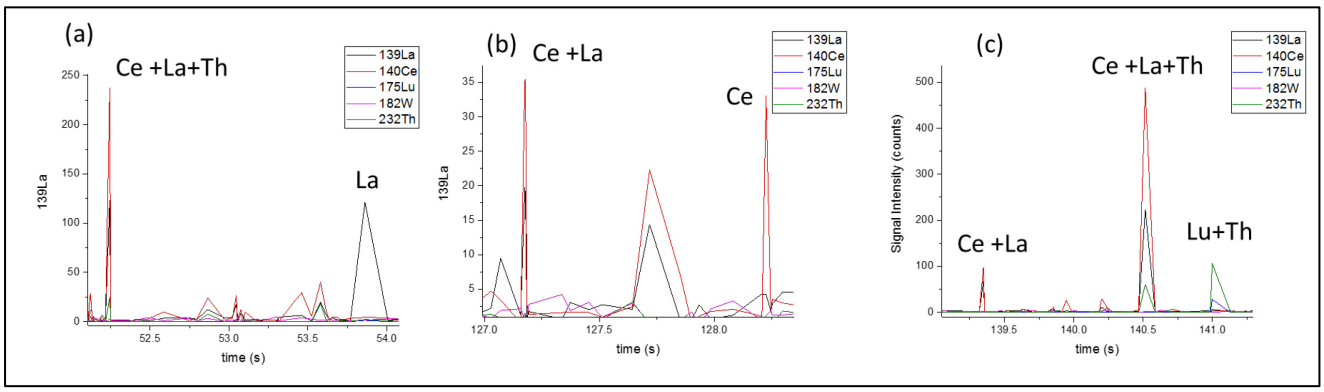

Figure 55: Particles of Ce, La and Th present as mono and multi-elemental in River Rhine. There are different combinations of Ce, La and Th paricles. Ce-La-Th and La paricles (a,) Ce-La ad Ce particles (b), Ce-La, Ce-La-Th and Lu-Th particles (c).

Comparable to the sample of Lake Zürich and the Limmat River, particles of ceria with La and Th were also present in the water of River Rhine (Figure 55). From the water samples'

content, in terms of the nature of the particle, their quantity and size distribution of the particles, a trend can be seen which can correlate to the nature of the environmental sample analysed. A stark difference between the water sample from the effluent and the environmental samples lies in the presence, concentration and size distribution (in mass) of naturally occurring particles of Al, Mn, Ce and Pb in the environmental samples. The particles at the concentration they are present can help to trace the origin of an environmental water sample.

The simultaneous detection of the particles in the environmental water samples was only possible with the use of a MDG in combination to an ICP-TOF-MS. With droplets generated from the MDG acting as a pseudo-multielement NPs for calibration purposes, the novel approach sample introduction approach offers many possibilities, one of which is demonstrated in this study. Together with the ICP-TOF-MS, this approach has given rise to a new aspect in the analysis of environmental samples.

5 Conclusion and Outlook

In order to address the lack of reference material available in the characterisation of NPs by customarily used spICP-MS, a new instrumental configuration for NP determination was investigated. Initially, a MDG which produces droplets was coupled to an ICP-MS giving a transport efficiency of 100 %. However, the low sample throughput and the difficulty in efficiently producing NP-containing droplets meant that the MDG as a sample introduction system with the ICP-MS cannot be used as a routine analysis of NPs. Therefore to provide more flexibility in terms of samples to be introduced while at the same time having the possibility to introduce droplets of well-defined size and mass into the ICP-MS, a combination of sample introducing system was developed. The MDG was coupled to an ICP-MS in a vertical manner for calibration purposes while the regular use of a pneumatic nebuliser was retained for the analysis of more complex materials. This approach combines the advantages of the efficiently transported MDG droplets (ca. 100 %) as a reference and high sample throughput via the pneumatic nebuliser.

In a first approach, the combined sample introduction system was optimised for both dissolved samples introduced as droplets and NPs aspirated via a PN into the ICP-MS. The main difference to the typical spICP-MS operating condition lies in the sample gas flows as He is an additional gas used to dry the droplet as it travels to the ICP-MS. Bulk analysis of unknown Ag and Au NP samples and the complete characterisation (size and concentration) of these NPs samples with a dissolved analyte solution as reference material was successfully carried out.

The combined sample introduction system was then applied in the analysis of ZnO and Al_2O_3. For this purpose, different separation techniques were employed to reduce the concentration of dissolved ions in the oxidic metallic NPs. In the case of the sample of ZnO, however, not only was the background noise high, but the ZnO NPs sample revealed that the

NPs were non uniform in their shape and therefore a size distribution was not feasible. Following consecutive washing steps, the use of the MDG-spICP-MS was applied in the size determination of Al_2O_3. The size distribution in nm was obtained without the use of a reference material. This work is a first step in the analysis of metal oxide NPs by spICP-MS, where a matrix matched calibration method is used. The contrasting success in analyzing ZnO and Al_2O_3 NPs points to the importance and the limit of the method.

A new possibility in the study of matrix effect was possible with the dual sample introduction system. In this study, the MDG was coupled to an ICP-TOF-MS for simultaneous detection of the calibrant, NPs and matrices. Matrix effect which may be occurring during the sample introduction and/or in the plasma is addressed: NPs are introduced together with the different matrices as aerosols via the PN while droplets of metal standards (pseudo-NPs) are generated via the MDG.

The first part of the study involved analysing SiO_2-Au NPs in the presence of the most used acid matrices: HCl and HNO_3. The varying concentration of acids showed a effect on both the droplet and on the NPs. However, the size determination of the SiO_2-Au NPs remained accurate and within the range provided by the manufacturer.

The second part of the matrix effect study involved elemental matrices (Li, Mg, Rb, Cs, La, Ce, Lu, Pb and U) of various physical property including mass, heat of vaporisation, ionisation energy and melting point. This study involved the introduction of Ag NPs, enriched ^{109}Ag solution and Ag droplets together with different concentration of the elemental matrices. Regardless of the diverse effects of the elemental matrices on the different Ag analytes, the size calculated of the Ag NP stays within the range of uncertainties of the given NPs' size. Therefore, using a combination of the MDG-ICP-MS, the correct NPs` sizes in the various the matrices tested was determined.

Eventually, the applicability of the dual sample introduction was tested on four real water samples: effluent from the chemistry building from ETH and environmental samples from: Lake Zürich, Limmat River and River Rhine. Because, the nature of macro- and NPs in environmental samples are unknown, a mass analyser with fast analysis time and simultaneous detection capabilities is best suited. For the purpose of this work, the real water sample were analysed by a TOF analyser. Using a multi-elemental droplet for calibration purposes, the characterisation of all major macro-and NPs was accomplished. Besides, particles of multi-elemental nature were also seen in the environmental waters. Therefore, the method, provides the possibility to distinguish between naturally occurring and engineered particles which are in most cases more homogeneous and of single-elemental nature. Moreover, with similar elemental composition, the group of environmental sample could be distinguished from the effluent water sample.

The combination of the MDG and spICP-MS has been shown to be not only applicable in the characterisation of metallic NPs, but also metal oxides NPs. This dual sample introduction technique has given rise to more possibilities in the study of matrix effects which arise and affect the day to day ICP-MS analyses. Its application together with a simultaneous detector was shown to be effective in the quantitative and qualitative analysis of real and environmental sample. Finally, the developed system would now allow to monitor NP effects on a daily basis and could be used for extensive environmental studies.

The developed analytical method can be applied to improve and refine the methodologies for NPs´ quantification. In this sense, further work can be focused on the cause of the size dependent transport efficiency since significant differences depending on the size and nature of the NP were observed. In addition, studies on the influence of the physical properties of the NPs on the nebulisation efficiency can also be performed.

Since toxicity of NPs is a major concern in the use of metal oxides NPs, namely TiO_2, the use of the MDG together with spICP-MS can be further expanded to analyse different samples including cosmetics for metal oxides particles. In combination with separation techniques, the MDG spICP-MS combination would be a complementary tool in the analysis of the NPs where no standard reference material is available.

Another interesting application which extends to the biological aspects of NPs, is the investigation of NPs in tissue or cells. With the MDG providing the calibration and the ICP-MS offering high throughput analysis, after homogenisation and purification steps of the biological material the NPs can be characterised in a qualitative and quantitative manner.

In the application of MDG with an ICP-TOF-MS, natural and engineered macroparticles and NPs can be distinguished. Eventually, this allows tracing back samples to its source. The use of this method is not restricted to water samples but also e.g. dissolved soil samples can be analysed. Therefore there is hardly any limitation for the use of this method as long as an appropriate sample preparation is possible.

6 Appendix

6.1 Abbreviations

AES	Atomic emission spectrometer
AF4	Asymmetric field flow fractionation
AFM	Atomic force microscopy
CCD camera	Charge-coupled device camera
Cps	Counts per second
DLS	Dynamic light scattering
EIE	Easily/efficiently ionised elements
ENP	Engineered nanoparticles
ESA	Electrostatic analyser
HDC	Hydrodynamic size chromatography
HPLC	High performance liquid chromatography
ICP	Inductively coupled plasma
ICP-MS	Inductively coupled plasma mass spectrometry
ICP-OES	Inductively coupled optical emission spectrometry
IDA	Isotope dilution analysis
IEC	Ion exchange chromatography
KE	Kinetic energy
LA	Laser ablation system
LOD	Limit of detection
MDG	Microdroplet generator
MDMI	Monodisperse dried micro-particulate injector
NAZ	Normal analytical zone
NIST	National Institute of Standards and Technology
NOM	Natural organic matter
NP	Nanoparticle

PN	Pneumatic nebuliser
RF	Radiofrequency
RSD	Relative standard deviation
RP-HPLC	Reversed phase chromatography
SdFFF	Sedimentation field flow fractionation
SEM	Scanning electron microscopy
SF	Sector field
ε_n	Transport efficiency
TE	Transport efficiency
TEM	Transmission electron microscopy
spICP-MS	Single particle mode ICP-MS
TOF	Time of flight
TOFMS	Time-of-flight mass spectrometer
NP	Nanoparticle
XRD	X-ray diffraction

7 References

1. EuropeanCommision Review of Environmental Legislation for the Regulatory Control of Nanomaterials http://ec.europa.eu/environment/chemicals/nanotech/index_en.htm (accessed 10th December 2018).
2. Gottschalk, F., T. Sonderer, R.W. Scholz, and B. Nowack, Modeled environmental concentrations of engineered nanomaterials (TiO2, ZnO, Ag, CNT, fullerenes) for different regions, *Environmental science & technology y* **2009,** *43*, 9216-9222.
3. Sharma, V.K., J. Filip, R. Zboril, and R.S. Varma, Natural inorganic nanoparticles - formation, fate, and toxicity in the environment, *Chemical Society Reviews* **2015,** *44*, 8410-8423.
4. Yin, Y., J. Liu, and G. Jiang, Sunlight-induced reduction of ionic Ag and Au to metallic nanoparticles by dissolved organic matter, *Acs Nano* **2012,** *6*, 7910-7919.
5. Levard, C., E.M. Hotze, G.V. Lowry, and G.E. Brown, Environmental Transformations of Silver Nanoparticles: Impact on Stability and Toxicity, *Environmental science & technology* **2012,** *46*, 6900-6914.
6. Sun, Y. and Y. Xia, Shape-controlled synthesis of gold and silver nanoparticles, *Science* **2002,** *298*, 2176-2179.
7. Vance, M.E., T. Kuiken, E.P. Vejerano, S.P. McGinnis, M.F. Hochella Jr, D. Rejeski, and M.S. Hull, Nanotechnology in the real world: Redeveloping the nanomaterial consumer products inventory, *Beilstein journal of nanotechnology* **2015,** *6*, 1769-1780.
8. Kim, J.S., E. Kuk, K.N. Yu, J.-H. Kim, S.J. Park, H.J. Lee, S.H. Kim, Y.K. Park, Y.H. Park, and C.-Y. Hwang, Antimicrobial effects of silver nanoparticles, *Nanomedicine: Nanotechnology, Biology and Medicine* **2007,** *3*, 95-101.
9. Lee, K.-S. and M.A. El-Sayed, Gold and silver nanoparticles in sensing and imaging: sensitivity of plasmon response to size, shape, and metal composition, *The Journal of Physical Chemistry B* **2006,** *110*, 19220-19225.
10. Peters, R.J., G. Bemmel, Z. Herrera-Rivera, H.P. Helsper, H.J. Marvin, S. Weigel, P.C. Tromp, A.G. Oomen, A.G. Rietveld, and H. Bouwmeester, Characterization of titanium dioxide nanoparticles in food products: analytical methods to define nanoparticles, *Journal of Agricultural and Food Chemistr* **2014,** *62*.
11. Tiede, K., A.B. Boxall, S.P. Tear, J. Lewis, H. David, and M. Hassellöv, Detection and characterization of engineered nanoparticles in food and the environment, *Food Additives and Contaminants* **2008,** *25*, 795-821.
12. Kvítek, L., A. Panáček, J. Soukupová, M. Kolář, R. Večeřová, R. Prucek, M. Holecová, and R. Zbořil, Effect of Surfactants and Polymers on Stability and Antibacterial Activity of Silver Nanoparticles (NPs), *The Journal of Physical Chemistry C* **2008,** *112*, 5825-5834.
13. Huang, K., H. Ma, J. Liu, S. Huo, A. Kumar, T. Wei, X. Zhang, S. Jin, Y. Gan, and P.C. Wang, Size-dependent localization and penetration of ultrasmall gold nanoparticles in cancer cells, multicellular spheroids, and tumors in vivo, *Acs Nano* **2012,** *6*.
14. Salata, O.V., Applications of nanoparticles in biology and medicine, *Journal of Nanobiotechnology* **2004,** *2*, 3.
15. Veronovski, N., M. Lesnik, A. Lubej, and D. Verhovsek, Surface treated titanium dioxide nanoparticles as inorganic UV filters in sunscreen products, *Acta Chimica Slovenica* **2014,** *61*.
16. Donovan, A.R., C.D. Adams, Y. Ma, C. Stephan, T. Eichholz, and H. Shi, Detection of zinc oxide and cerium dioxide nanoparticles during drinking water treatment by rapid single particle ICP-MS methods, *Analytical and bioanalytical chemistry* **2016,** *408*, 5137-5145.
17. Batley, G.E., J.K. Kirby, and M.J. McLaughlin, Fate and Risks of Nanomaterials in Aquatic and Terrestrial Environments, *Accounts of Chemical Research* **2013,** *46*, 854-862.
18. Li, M., S. Pokhrel, X. Jin, L. Mädler, R. Damoiseaux, and E.M. Hoek, Stability, bioavailability, and bacterial toxicity of ZnO and iron-doped ZnO nanoparticles in aquatic media, *Environmental science & technology* **2010,** *45*, 755-761.
19. Donaldson, K., L. Tran, L.A. Jimenez, R. Duffin, D.E. Newby, N. Mills, W. MacNee, and V. Stone, Combustion-derived nanoparticles: a review of their toxicology following inhalation exposure, *Particle and fibre toxicology* **2005,** *2*, 1.

20. Brunner, T.J., P. Wick, P. Manser, P. Spohn, R.N. Grass, L.K. Limbach, A. Bruinink, and W.J. Stark, In vitro cytotoxicity of oxide nanoparticles: comparison to asbestos, silica, and the effect of particle solubility, *Environmental science & technology* **2006,** *40*, 4374-4381.
21. Ma, R., C.m. Levard, J.D. Judy, J.M. Unrine, M. Durenkamp, B. Martin, B. Jefferson, and G.V. Lowry, Fate of zinc oxide and silver nanoparticles in a pilot wastewater treatment plant and in processed biosolids, *Environmental science & technology* **2013,** *48*, 104-112.
22. Zhang, L., Y. Jiang, Y. Ding, M. Povey, and D. York, Investigation into the antibacterial behaviour of suspensions of ZnO nanoparticles (ZnO nanofluids), *Journal of Nanoparticle Research* **2007,** *9*, 479-489.
23. Applerot, G., A. Lipovsky, R. Dror, N. Perkas, Y. Nitzan, R. Lubart, and A. Gedanken, Enhanced antibacterial activity of nanocrystalline ZnO due to increased ROS-mediated cell injury, *Advanced Functional Materials* **2009,** *19*, 842-852.
24. Liu, W., Y. Wu, C. Wang, H.C. Li, T. Wang, C.Y. Liao, L. Cui, Q.F. Zhou, B. Yan, and G.B. Jiang, Impact of silver nanoparticles on human cells: effect of particle size, *Nanotoxicology* **2010,** *4*.
25. Mortimer, M., K. Kasemets, and A. Kahru, Toxicity of ZnO and CuO nanoparticles to ciliated protozoa Tetrahymena thermophila, *Toxicology* **2010,** *269*, 182-189.
26. Miller, R.J., H.S. Lenihan, E.B. Muller, N. Tseng, S.K. Hanna, and A.A. Keller, Impacts of metal oxide nanoparticles on marine phytoplankton, *Environmental science & technology* **2010,** *44*, 7329-7334.
27. Li, M., L. Zhu, and D. Lin, Toxicity of ZnO nanoparticles to Escherichia coli: mechanism and the influence of medium components, *Environmental science & technology* **2011,** *45*, 1977-1983.
28. Mudunkotuwa, I.A., T. Rupasinghe, C.-M. Wu, and V.H. Grassian, Dissolution of ZnO nanoparticles at circumneutral pH: a study of size effects in the presence and absence of citric acid, *Langmuir* **2011,** *28*, 396-403.
29. Manzo, S., A. Rocco, R. Carotenuto, F.D.L. Picione, M.L. Miglietta, G. Rametta, and G. Di Francia, Investigation of ZnO nanoparticles' ecotoxicological effects towards different soil organisms, *Environmental Science and Pollution Research* **2011,** *18*, 756-763.
30. Tuoriniemi, J., G. Cornelis, and M. Hassellov, Size discrimination and detection capabilities of single-particle ICPMS for environmental analysis of silver nanoparticles, *Analytical Chemistry* **2012,** *84*, 3965-72.
31. Sondi, I. and B. Salopek-Sondi, Silver nanoparticles as antimicrobial agent: a case study on E. coli as a model for Gram-negative bacteria, *Journal of colloid and interface science* **2004,** *275*, 177-182.
32. José-Yacamán, M., M. Marın-Almazo, and J. Ascencio, High resolution TEM studies on palladium nanoparticles, *Journal of Molecular Catalysis A: Chemical* **2001,** *173*, 61-74.
33. Zak, A.K., W.A. Majid, M.E. Abrishami, and R. Yousefi, X-ray analysis of ZnO nanoparticles by Williamson–Hall and size–strain plot methods, *Solid State Sciences* **2011,** *13*, 251-256.
34. Junno, T., K. Deppert, L. Montelius, and L. Samuelson, Controlled manipulation of nanoparticles with an atomic force microscope, *Applied Physics Letters* **1995,** *66*, 3627-3629.
35. Hoo, C.M., N. Starostin, P. West, and M.L. Mecartney, A comparison of atomic force microscopy (AFM) and dynamic light scattering (DLS) methods to characterize nanoparticle size distributions, *Journal of Nanoparticle Research* **2008,** *10*, 89-96.
36. Akthakul, A., A.I. Hochbaum, F. Stellacci, and A.M. Mayes, Size fractionation of metal nanoparticles by membrane filtration, *Advanced materials* **2005,** *17*, 532-535.
37. Mächtle, W. and L. Börger, *Analytical ultracentrifugation of polymers and nanoparticles*. Springer Science & Business Media: 2006.
38. Pergantis, S.A., T.L. Jones-Lepp, and E.M. Heithmar, Hydrodynamic chromatography online with single particle-inductively coupled plasma mass spectrometry for ultratrace detection of metal-containing nanoparticles, *Analytical Chemistry* **2012,** *84*, 6454-6462.
39. Sötebier, C.A., S.M. Weidner, N. Jakubowski, U. Panne, and J. Bettmer, Separation and quantification of silver nanoparticles and silver ions using reversed phase high performance liquid chromatography coupled to inductively coupled plasma mass spectrometry in combination with isotope dilution analysis, *Journal of Chromatography A* **2016,** *1468*, 102-108.

40. Soto-Alvaredo, J., M. Montes-Bayón, and J.r. Bettmer, Speciation of silver nanoparticles and silver (I) by reversed-phase liquid chromatography coupled to ICPMS, *Analytical Chemistry* **2013,** *85*, 1316-1321.
41. Hagendorfer, H., R. Kaegi, M. Parlinska, B. Sinnet, C. Ludwig, and A. Ulrich, Characterization of Silver Nanoparticle Products Using Asymmetric Flow Field Flow Fractionation with a Multidetector Approach–a Comparison to Transmission Electron Microscopy and Batch Dynamic Light Scattering, *Analytical Chemistry* **2012,** *84*, 2678-2685.
42. Meermann, B., K. Wichmann, F. Lauer, F. Vanhaecke, and T.A. Ternes, Application of stable isotopes and AF4/ICP-SFMS for simultaneous tracing and quantification of iron oxide nanoparticles in a sediment-slurry matrix, *Journal of Analytical Atomic Spectrometry* **2016,** *31*, 890-901.
43. Sötebier, C.A., F.S. Bierkandt, S. Rades, N. Jakubowski, U. Panne, and S.M. Weidner, Sample loss in asymmetric flow field-flow fractionation coupled to inductively coupled plasma-mass spectrometry of silver nanoparticles, *Journal of Analytical Atomic Spectrometry* **2015,** *30*, 2214-2222.
44. Soto-Alvaredo, J., F. Dutschke, J. Bettmer, M. Montes-Bayon, D. Profrock, and A. Prange, Initial results on the coupling of sedimentation field-flow fractionation (SdFFF) to inductively coupled plasma-tandem mass spectrometry (ICP-MS/MS) for the detection and characterization of TiO2 nanoparticles, *Journal of Analytical Atomic Spectrometry* **2016,** *31*, 1549-1555.
45. Mitrano, D.M., A. Barber, A. Bednar, P. Westerhoff, C.P. Higgins, and J.F. Ranville, Silver nanoparticle characterization using single particle ICP-MS (SP-ICP-MS) and asymmetrical flow field flow fractionation ICP-MS (AF4-ICP-MS), *Journal of Analytical Atomic Spectrometry* **2012,** *27*, 1131-1142.
46. Bednar, A.J., A.R. Poda, D. Mitrano, A. Kennedy, E. Gray, J. Ranville, C. Hayes, F. Crocker, and J. Steevens, Comparison of on-line detectors for field flow fractionation analysis of nanomaterials, *Talanta* **2013,** *104*, 140-148.
47. Houk, R.S., V.A. Fassel, G.D. Flesch, H.J. Svec, A.L. Gray, and C.E. Taylor, Inductively coupled argon plasma as an ion source for mass spectrometric determination of trace elements, *Analytical Chemistry* **1980,** *52*, 2283-2289.
48. Rao, R.N. and M.K. Talluri, An overview of recent applications of inductively coupled plasma-mass spectrometry (ICP-MS) in determination of inorganic impurities in drugs and pharmaceuticals, *Journal of pharmaceutical and biomedical analysis* **2007,** *43*, 1-13.
49. von der Kammer, F., P.L. Ferguson, P.A. Holden, A. Masion, K.R. Rogers, S.J. Klaine, A.A. Koelmans, N. Horne, and J.M. Unrine, Analysis of engineered nanomaterials in complex matrices (environment and biota): general considerations and conceptual case studies, *Environmental Toxicology and Chemistry* **2012,** *31*, 32-49.
50. Gondikas, A.P., F.v.d. Kammer, R.B. Reed, S. Wagner, J.F. Ranville, and T. Hofmann, Release of TiO2 nanoparticles from sunscreens into surface waters: a one-year survey at the old Danube recreational Lake, *Environmental science & technology* **2014,** *48*, 5415-5422.
51. Montaser, A., *Inductively coupled plasma mass spectrometry*. John Wiley & Sons: 1998.
52. Olesik, J.W., J.A. Kinzer, and B. Harkleroad, Inductively coupled plasma optical emission spectrometry using nebulizers with widely different sample consumption rates, *Analytical Chemistry* **1994,** *66*, 2022-2030.
53. Thomas, R., *Practical guide to ICP-MS: a tutorial for beginners*. CRC press: 2013.
54. Dawson, P.H., *Quadrupole mass spectrometry and its applications*. Elsevier: 2013.
55. Olesik, J.W., Inductively coupled plasma mass spectrometry, *PRACTICAL SPECTROSCOPY SERIES* **2000,** *23*, 67-158.
56. Miller, P.E. and M.B. Denton, The quadrupole mass filter: basic operating concepts, *Journal of Chemical Education* **1986,** *63*, 617.
57. Mattauch, J. and R. Herzog, Über einen neuen Massenspektrographen, *Zeitschrift für Physik* **1934,** *89*, 786-795.
58. Gießmann, U. and U. Greb, High resolution ICP-MS—a new concept for elemental mass spectrometry, *Fresenius' journal of analytical chemistry* **1994,** *350*, 186-193.
59. Jakubowski, N., L. Moens, and F. Vanhaecke, Sector field mass spectrometers in ICP-MS, *Spectrochimica Acta Part B: Atomic Spectroscopy* **1998,** *53*, 1739-1763.

60. Prohaska, T., J. Irrgeher, A. Zitek, and N. Jakubowski, *Sector Field Mass Spectometry for Elemental and Isotopic Analysis*. Royal Society of Chemistry: 2014.
61. Myers, D.P., G. Li, P. Yang, and G.M. Hieftje, An inductively coupled plasma-time-of-flight mass spectrometer for elemental analysis. Part I: Optimization and characteristics, *Journal of the American Society for Mass Spectrometry* **1994,** *5*, 1008-1016.
62. Guilhaus, M., D. Selby, and V. Mlynski, Orthogonal acceleration time-of-flight mass spectrometry, *Mass spectrometry reviews* **2000,** *19*, 65-107.
63. Mamyrin, B., V. Karataev, D. Shmikk, and V. Zagulin, The mass-reflectron, a new nonmagnetic time-of-flight mass spectrometer with high resolution, *Soviet Journal of Experimental and Theoretical Physics* **1973,** *37*, 45.
64. Hendriks, L., A. Gundlach-Graham, B. Hattendorf, and D. Günther, Characterization of a new ICP-TOFMS instrument with continuous and discrete introduction of solutions, *Journal of Analytical Atomic Spectrometry* **2017,** *32*, 548-561.
65. Gundlach-Graham, A., M. Burger, S. Allner, G. Schwarz, H.A. Wang, L. Gyr, D. Grolimund, B. Hattendorf, and D. Günther, High-speed, high-resolution, multielemental laser ablation-inductively coupled plasma-time-of-flight mass spectrometry imaging: part I. Instrumentation and two-dimensional imaging of geological samples, *Analytical Chemistry* **2015,** *87*, 8250-8258.
66. Borovinskaya, O., S. Gschwind, B. Hattendorf, M. Tanner, and D. Gunther, Simultaneous mass quantification of nanoparticles of different composition in a mixture by microdroplet generator-ICPTOFMS, *Analytical Chemistry* **2014,** *86*, 8142-8.
67. Olesik, J.W. and L.C. Bates, Characterization of aerosols produced by pneumatic nebulizers for inductively coupled plasma sample introduction: effect of liquid and gas flow rates on volume based drop size distributions, *Spectrochimica Acta Part B: Atomic Spectroscopy* **1995,** *50*, 285-303.
68. Wiederin, D.R., F.G. Smith, and R. Houk, Direct injection nebulization for inductively coupled plasma mass spectrometry, *Analytical Chemistry* **1991,** *63*, 219-225.
69. Homepage of J E Meinhard Associates, I.https://www.meinhard.com/index.cfm/category/8/spray-chambers.cfm (accessed 10th December 2018).
70. Beres, S., P. Brueckner, and E. Denoyer, Performance evaluation of a cyclonic spray chamber for ICP-MS, *Atomic spectroscopy* **1994,** *15*, 96-99.
71. Stewart, I.I. and J.W. Olesik, The effect of nitric acid concentration and nebulizer gas flow rates on aerosol properties and transport rates in inductively coupled plasma sample introduction, *Journal of Analytical Atomic Spectrometry* **1998,** *13*, 1249-1256.
72. Canals, A., V. Hernandis, J. Todoli, and R. Browner, Fundamental studies on pneumatic generation and aerosol transport in atomic spectrometry: effect of mineral acids on emission intensity in inductively coupled plasma atomic emission spectrometry, *Spectrochimica Acta Part B: Atomic Spectroscopy* **1995,** *50*, 305-321.
73. Todolí, J.-l. and J.-m. Mermet, Minimization of acid effects at low consumption rates in an axially viewed inductively coupled plasma atomic emission spectrometer by using micronebulizer-based sample introduction systems, *Journal of Analytical Atomic Spectrometry* **1998,** *13*, 727-734.
74. Vaughan, M.A. and G. Horlick, Oxide, Hydroxide, and Doubly Charged Analyte Species in Inductively Coupled Plasma/Mass Spectrometry, *Applied spectroscopy* **1986,** *40*, 434-445.
75. Ramsey, M.H. and M. Thompson, A predictive model of plasma matrix effects in inductively coupled plasma atomic emission spectrometry, *Journal of Analytical Atomic Spectrometry* **1986,** *1*, 185-193.
76. Vanhaecke, F., R. Dams, and C. Vandecasteele, 'Zone model'as an explanation for signal behaviour and non-spectral interferences in inductively coupled plasma mass spectrometry, *Journal of Analytical Atomic Spectrometry* **1993,** *8*, 433-438.
77. Horner, J.A. and G.M. Hieftje, Computerized simulation of mixed-solute-particle vaporization in an inductively coupled plasma1, *Spectrochimica Acta Part B: Atomic Spectroscopy* **1998,** *53*, 1235-1259.
78. N.N. Sesi, G.M.H., Studies into the interelement matrix effect in inductively coupled plasma spectrometry, *Spectrochimica Acta Part B* **1996**, 1601.

79. P.J. Galley, M.G., G.M. Hieftje, Easily ionizable element interferences in ICP-AES. Part I. Effect on radial analyte emission patterns, *Spectrochimica Acta Part B* **1993,** *48*.
80. Tan, S.H. and G. Horlick, Matrix-effect observations in inductively coupled plasma mass spectrometry, *Journal of Analytical Atomic Spectrometry* **1987,** *2*, 745-763.
81. Hobbs, S.E. and J.W. Olesik, The influence of incompletely desolvated droplets and vaporizing particles on chemical matrix effects in inductively coupled plasma spectrometry: time-gated optical emission and laser-induced fluorescence measurements, *Spectrochimica Acta Part B: Atomic Spectroscopy* **1997,** *52*, 353-367.
82. Hobbs, S.E. and J.W. Olesik, Inductively coupled plasma mass spectrometry signal fluctuations due to individual aerosol droplets and vaporizing particles, *Anal Chem* **1992,** *64*, 274-283.
83. Mermet, J., Use of magnesium as a test element for inductively coupled plasma atomic emission spectrometry diagnostics, *Analytica chimica acta* **1991,** *250*, 85-94.
84. Olesik, J.W. and M.P. Dziewatkoski, Time-resolved measurements of individual ion cloud signals to investigate space-charge effects in plasma mass spectrometry, *Journal of the American Society for Mass Spectrometry* **1996,** *7*, 362-367.
85. Kawaguchi, H., N. Fukasawa, and A. Mizuike, Investigation of airborne particles by inductively coupled plasma emission spectrometry calibrated with monodisperse aerosols, *Spectrochimica Acta Part B: Atomic Spectroscopy* **1986,** *41*, 1277-1286.
86. Bochert, U. and W. Dannecker, On-line aerosol analysis by atomic emission spectroscopy, *Journal of Aerosol Science* **1989,** *20*, 1525-1528.
87. Nomizu, T., H. Nakashima, Y. Hotta, T. Tanaka, and H. Kawaguchi, Simultaneous Measurement of the Elemental Content and Size of Airborne Particles by Inductively Coupled Plasma Emission Spectrometry Combined with the Laser Light-Scattering Method, *Analytical sciences* **1992,** *8*, 527-531.
88. Degueldre, C. and P.-Y. Favarger, Colloid analysis by single particle inductively coupled plasma-mass spectroscopy: a feasibility study, *Colloids and Surfaces A: Physicochemical and Engineering Aspects* **2003,** *217*, 137-142.
89. Degueldre, C., P.-Y. Favarger, and C. Bitea, Zirconia colloid analysis by single particle inductively coupled plasma–mass spectrometry, *Analytica chimica acta* **2004,** *518*, 137-142.
90. Degueldre, C. and P.-Y. Favarger, Thorium colloid analysis by single particle inductively coupled plasma-mass spectrometry, *Talanta* **2004,** *62*, 1051-1054.
91. Degueldre, C., P.-Y. Favarger, and S. Wold, Gold colloid analysis by inductively coupled plasma-mass spectrometry in a single particle mode, *Analytica chimica acta* **2006,** *555*, 263-268.
92. Degueldre, C., P.-Y. Favarger, R. Rosse, and S. Wold, Uranium colloid analysis by single particle inductively coupled plasma-mass spectrometry, *Talanta* **2006,** *68*, 623-628.
93. Laborda, F., J. Jiménez-Lamana, E. Bolea, and J.R. Castillo, Selective identification, characterization and determination of dissolved silver (I) and silver nanoparticles based on single particle detection by inductively coupled plasma mass spectrometry, *Journal of Analytical Atomic Spectrometry* **2011,** *26*, 1362-1371.
94. Mitrano, D.M., E.K. Lesher, A. Bednar, J. Monserud, C.P. Higgins, and J.F. Ranville, Detecting nanoparticulate silver using single-particle inductively coupled plasma-mass spectrometry, *Environmental Toxicology and Chemistry* **2012,** *31*, 115-21.
95. Pace, H.E., N.J. Rogers, C. Jarolimek, V.A. Coleman, C.P. Higgins, and J.F. Ranville, Determining transport efficiency for the purpose of counting and sizing nanoparticles via single particle inductively coupled plasma mass spectrometry, *Analytical Chemistry* **2011,** *83*, 9361-9.
96. Laborda, F., E. Bolea, and J. Jimenez-Lamana, Single particle inductively coupled plasma mass spectrometry: a powerful tool for nanoanalysis, *Analytical Chemistry* **2014,** *86*, 2270-8.
97. Heithmar, E.M. and S.A. Pergantis, *Characterizing Concentrations and Size Distributions of Metal-containing Nanoparticles in Waste Water*. US Environmental Protection Agency, Office of Research and Development, National Exposure Research Laboratory: 2010.
98. Laborda, F., J. Jiménez-Lamana, E. Bolea, and J.R. Castillo, Critical considerations for the determination of nanoparticle number concentrations, size and number size distributions by single particle ICP-MS, *Journal of Analytical Atomic Spectrometry* **2013,** *28*, 1220-1232.

99. Olesik, J.W. and P.J. Gray, Considerations for measurement of individual nanoparticles or microparticles by ICP-MS: determination of the number of particles and the analyte mass in each particle, *Journal of Analytical Atomic Spectrometry* **2012,** *27*, 1143.
100. Gustavsson, A., The determination of some nebulizer characteristics, *Spectrochimica Acta Part B: Atomic Spectroscopy* **1984,** *39*, 743-746.
101. Montaño, M.D., J.W. Olesik, A.G. Barber, K. Challis, and J.F. Ranville, Single Particle ICP-MS: Advances toward routine analysis of nanomaterials, *Analytical and bioanalytical chemistry* **2016,** *408*, 5053-5074.
102. Pace, H.E., N.J. Rogers, C. Jarolimek, V.A. Coleman, E.P. Gray, C.P. Higgins, and J.F. Ranville, Single particle inductively coupled plasma-mass spectrometry: a performance evaluation and method comparison in the determination of nanoparticle size, *Environmental science & technology* **2012,** *46*, 12272-80.
103. Reed, R.B., C.P. Higgins, P. Westerhoff, S. Tadjiki, and J.F. Ranville, Overcoming challenges in analysis of polydisperse metal-containing nanoparticles by single particle inductively coupled plasma mass spectrometry, *Journal of Analytical Atomic Spectrometry* **2012,** *27*, 1093-1100.
104. Liu, J., K.E. Murphy, R.I. MacCuspie, and M.R. Winchester, Capabilities of single particle inductively coupled plasma mass spectrometry for the size measurement of nanoparticles: a case study on gold nanoparticles, *Analytical Chemistry* **2014,** *86*, 3405-3414.
105. Borovinskaya, O., S. Gschwind, B. Hattendorf, M. Tanner, and D. Günther, Simultaneous mass quantification of nanoparticles of different composition in a mixture by microdroplet generator-ICPTOFMS, *Analytical Chemistry* **2014,** *86*, 8142-8148.
106. Strenge, I. and C. Engelhard, Capabilities of fast data acquisition with microsecond time resolution in inductively coupled plasma mass spectrometry and identification of signal artifacts from millisecond dwell times during detection of single gold nanoparticles, *Journal of Analytical Atomic Spectrometry* **2015**.
107. Montano, M., H. Badiei, S. Bazargan, and J. Ranville, Improvements in the detection and characterization of engineered nanoparticles using spICP-MS with microsecond dwell times, *Environmental Science: Nano* **2014,** *1*, 338-346.
108. Loeschner, K., J. Navratilova, C. Købler, K. Mølhave, S. Wagner, F. von der Kammer, and E.H. Larsen, Detection and characterization of silver nanoparticles in chicken meat by asymmetric flow field flow fractionation with detection by conventional or single particle ICP-MS, *Analytical and bioanalytical chemistry* **2013,** *405*, 8185-8195.
109. Kim, S.T., H.K. Kim, S.H. Han, E.C. Jung, and S. Lee, Determination of size distribution of colloidal TiO 2 nanoparticles using sedimentation field-flow fractionation combined with single particle mode of inductively coupled plasma-mass spectrometry, *Microchemical Journal* **2013,** *110*, 636-642.
110. Hadioui, M., C. Peyrot, and K.J. Wilkinson, Improvements to single particle ICPMS by the online coupling of ion exchange resins, *Analytical Chemistry* **2014,** *86*, 4668-4674.
111. Hadioui, M., V. Merdzan, and K.J. Wilkinson, Detection and characterization of ZnO nanoparticles in surface and waste waters using single particle ICPMS, *Environmental science & technology* **2015,** *49*, 6141-6148.
112. Tadjiki, S., M.D. Montaño, S. Assemi, A. Barber, J. Ranville, and R. Beckett, Measurement of the Density of Engineered Silver Nanoparticles Using Centrifugal FFF-TEM and Single Particle ICP-MS, *Analytical Chemistry* **2017,** *89*, 6056-6064.
113. Scheffer, A., C. Engelhard, M. Sperling, and W. Buscher, ICP-MS as a new tool for the determination of gold nanoparticles in bioanalytical applications, *Analytical and bioanalytical chemistry* **2008,** *390*, 249-252.
114. Shigeta, K., H. Traub, U. Panne, A. Okino, L. Rottmann, and N. Jakubowski, Application of a micro-droplet generator for an ICP-sector field mass spectrometer–optimization and analytical characterization, *Journal of Analytical Atomic Spectrometry* **2013,** *28*, 646-656.
115. Sötebier, C.A., D.J. Kutscher, L. Rottmann, N. Jakubowski, U. Panne, and J. Bettmer, Combination of single particle ICP-QMS and isotope dilution analysis for the determination of size, particle number and number size distribution of silver nanoparticles, *Journal of Analytical Atomic Spectrometry* **2016,** *31*, 2045-2052.
116. Borovinskaya, O., B. Hattendorf, M. Tanner, S. Gschwind, and D. Günther, A prototype of a new inductively coupled plasma time-of-flight mass spectrometer providing temporally

resolved, multi-element detection of short signals generated by single particles and droplets, *Journal of Analytical Atomic Spectrometry* **2013,** *28*, 226-233.
117. Hieftje, G. and H. Malmstadt, Unique system for studying flame spectrometric processes, *Analytical Chemistry* **1968,** *40*, 1860-1867.
118. Bastiaans, G. and G. Hieftje, Vaporization of individual solute particles in flame spectrometry, *Analytical Chemistry* **1974,** *46*, 901-910.
119. Bleasdell, B., E. Wittig, and G. Hieftje, An approximate model for the liberation and ionization of atoms from individual solute particles in flame spectrometry, *Spectrochimica Acta Part B: Atomic Spectroscopy* **1981,** *36*, 205-213.
120. Boss, C.B. and G.M. Hieftje, Experimental studies on spatial distributions of atoms surrounding an individual solute particle vaporizing in an analytical flame, *Anal Chem* **1979,** *51*, 1897-1905.
121. French, J.B., B. Etkin, and R. Jong, Monodisperse dried microparticulate injector for analytical instrumentation, *Analytical Chemistry* **1994,** *66*, 685-691.
122. Olesik, J.W. and S.E. Hobbs, Monodisperse dried microparticulate injector: a new tool for studying fundamental processes in inductively coupled plasmas, *Analytical Chemistry* **1994,** *66*, 3371-3378.
123. Allen, L.A., J.J. Leach, and R. Houk, Spatial location of the space charge effect in individual ion clouds using monodisperse dried microparticulate injection with a twin quadrupole inductively coupled plasma mass spectrometer, *Analytical Chemistry* **1997,** *69*, 2384-2391.
124. Stewart, I.I. and J.W. Olesik, Time-resolved measurements with single droplet introduction to investigate space-charge effects in plasma mass spectrometry, *Journal of the American Society for Mass Spectrometry* **1999,** *10*, 159-174.
125. Groh, S., C.C. Garcia, A. Murtazin, V. Horvatic, and K. Niemax, Local effects of atomizing analyte droplets on the plasma parameters of the inductively coupled plasma, *Spectrochimica Acta Part B: Atomic Spectroscopy* **2009,** *64*, 247-254.
126. Murtazin, A., S. Groh, and K. Niemax, Investigation of sample introduction-and plasma-related matrix effects in inductively coupled plasma spectrometry applying single analyte droplet and particle injection, *Spectrochimica Acta Part B: Atomic Spectroscopy* **2012,** *67*, 3-16.
127. Niemax, K., Considerations about the detection efficiency in inductively coupled plasma mass spectrometry, *Spectrochimica Acta Part B: Atomic Spectroscopy* **2012,** *76*, 65-69.
128. Homepage of microdrop Technologies GmbH. http://www.microdrop.de/electronics.html (accessed 10th December 2018).
129. Gschwind, S., L. Flamigni, J. Koch, O. Borovinskaya, S. Groh, K. Niemax, and D. Günther, Capabilities of inductively coupled plasma mass spectrometry for the detection of nanoparticles carried by monodisperse microdroplets, *Journal of Analytical Atomic Spectrometry* **2011,** *26*, 1166-1174.
130. Koch, J., L. Flamigni, S. Gschwind, S. Allner, H. Longerich, and D. Günther, Accelerated evaporation of microdroplets at ambient conditions for the on-line analysis of nanoparticles by inductively-coupled plasma mass spectrometry, *Journal of Analytical Atomic Spectrometry* **2013,** *28*, 1707.
131. Gschwind, S., H. Hagendorfer, D.A. Frick, and D. Gunther, Mass quantification of nanoparticles by single droplet calibration using inductively coupled plasma mass spectrometry, *Analytical Chemistry* **2013,** *85*, 5875-83.
132. Fabricius, A.-L., L. Duester, B. Meermann, and T.A. Ternes, ICP-MS-based characterization of inorganic nanoparticles—sample preparation and off-line fractionation strategies, *Analytical and bioanalytical chemistry* **2014,** *406*, 467-479.
133. Montano, M.D., J.W. Olesik, A.G. Barber, K. Challis, and J.F. Ranville, Single Particle ICP-MS: Advances toward routine analysis of nanomaterials, *Analytical and bioanalytical chemistry* **2016,** *408*, 5053-74.
134. Ramkorun-Schmidt, B., S.A. Pergantis, D. Esteban-Fernández, N. Jakubowski, and D. Günther, Investigation of a Combined Microdroplet Generator and Pneumatic Nebulization System for Quantitative Determination of Metal-Containing Nanoparticles Using ICPMS, *Analytical Chemistry* **2015,** *87*, 8687-8694.

135. Günther, D. and C.A. Heinrich, Enhanced sensitivity in laser ablation-ICP mass spectrometry using helium-argon mixtures as aerosol carrier, *Journal of Analytical Atomic Spectrometry* **1999,** *14*, 1363-1368.
136. O'Connor, C., B.L. Sharp, and P. Evans, On-line additions of aqueous standards for calibration of laser ablation inductively coupled plasma mass spectrometry: theory and comparison of wet and dry plasma conditions, *Journal of Analytical Atomic Spectrometry* **2006,** *21*, 556-565.
137. Flamigni, L., J. Koch, and D. Günther, The effect of carrier gas humidity on the vaporization of laser-produced aerosols in inductively coupled plasmas, *Journal of Analytical Atomic Spectrometry* **2014,** *29*, 280-286.
138. Dange, C., T. Phan, V. André, J. Rieger, J. Persello, and A. Foissy, Adsorption mechanism and dispersion efficiency of three anionic additives [poly (acrylic acid), poly (styrene sulfonate) and HEDP] on zinc oxide, *Journal of colloid and interface science* **2007,** *315*, 107-115.
139. Miao, A.J., X.Y. Zhang, Z. Luo, C.S. Chen, W.C. Chin, P.H. Santschi, and A. Quigg, Zinc oxide–engineered nanoparticles: Dissolution and toxicity to marine phytoplankton, *Environmental Toxicology and Chemistry* **2010,** *29*, 2814-2822.
140. Tso, C.P., C.M. Zhung, Y.H. Shih, Y.M. Tseng, S.C. Wu, and R.A. Doong, Stability of metal oxide nanoparticles in aqueous solutions, *Water Science Technology* **2010,** *61*, 127-33.
141. Zhou, D. and A.A. Keller, Role of morphology in the aggregation kinetics of ZnO nanoparticles, *Water Research* **2010,** *44*, 2948-56.
142. Bohme, S., H.J. Stark, T. Meissner, A. Springer, T. Reemtsma, D. Kuhnel, and W. Busch, Quantification of Al2O3 nanoparticles in human cell lines applying inductively coupled plasma mass spectrometry (neb-ICP-MS, LA-ICP-MS) and flow cytometry-based methods, *Journal of Nanopartical Research* **2014,** *16*, 2592.
143. Murtazin, A., S. Groh, and K. Niemax, Investigation of sample introduction- and plasma-related matrix effects in inductively coupled plasma spectrometry applying single analyte droplet and particle injection, *Spectrochimica Acta Part B: Atomic Spectroscopy* **2012,** *67*, 3-16.
144. Ramkorun-Schmidt, B., S.A. Pergantis, D. Esteban-Fernandez, N. Jakubowski, and D. Gunther, Investigation of a combined microdroplet generator and pneumatic nebulization system for quantitative determination of metal-containing nanoparticles using ICPMS, *Analytical Chemistry* **2015,** *87*, 8687-94.
145. Stewart, I.I. and J.W. Olesik, Steady state acid effects in ICP-MS, *Journal of Analytical Atomic Spectrometry* **1998,** *13*, 1313-1320.
146. Tanner, S.D., Space charge in ICP-MS: calculation and implications, *Spectrochimica Acta Part B: Atomic Spectroscopy* **1992,** *47*, 809-823.
147. Chan, G.C.-Y., W. Chan, X. Mao, and R.E. Russo, Investigation of matrix effect on dry inductively coupled plasma conditions using laser ablation sampling, *Spectrochimica Acta Part B: Atomic Spectroscopy* **2000,** *55*, 221-235.
148. Chan, G.C.-Y., W.-T. Chan, X. Mao, and R.E. Russo, Investigation of matrix effects in inductively coupled plasma-atomic emission spectroscopy using laser ablation and solution nebulization—effect of second ionization potential, *Spectrochimica Acta Part B: Atomic Spectroscopy* **2001,** *56*, 77-92.
149. Praphairaksit, N. and R. Houk, Reduction of mass bias and matrix effects in inductively coupled plasma mass spectrometry with a supplemental electron source in a negative extraction lens, *Analytical Chemistry* **2000,** *72*, 4435-4440.
150. Haynes, W.M., *CRC handbook of chemistry and physics*. CRC press: 2014.
151. Chen, X. Matrix effects in inductively coupled plasma mass spectrometry. Retrospective Theses and Dissertations, Iowa State University, 1995.
152. A.C. West, V.A.F., R.N. Kniseley, Lateral diffusion interferences in flame atomic absorption and emission spectrometry, *Analytical Chemistry.* **1973,** *45*.
153. Praetorius, A., A. Gundlach-Graham, E. Goldberg, W. Fabienke, J. Navratilova, A. Gondikas, R. Kaegi, D. Gunther, T. Hofmann, and F. von der Kammer, Single-particle multi-element fingerprinting (spMEF) using inductively-coupled plasma time-of-flight mass spectrometry (ICP-TOFMS) to identify engineered nanoparticles against the elevated natural background in soils, *Environmental Science: Nano* **2017,** *4*, 307-314.